Indoor radio propagation modeling for system performance prediction

Meiling Luo Xie

Numéro d'ordre: 2013-ISAL- Year 2013

Thesis

INDOOR RADIO PROPAGATION MODELING FOR SYSTEM PERFORMANCE PREDICTION

defended at

L'Institut National des Sciences Appliquées de Lyon

École Doctorale: Électronique, Électrotechnique et Automatique

for the degree of

DOCTOR OF PHILOSOPHY

Specialty: STIC Santé

by

Meiling LUO

Defended on July 17th, 2013

in front of the following jury

Directeurs	Jean-Marie Gorce	Professeur	INSA de Lyon
	Guillaume Villemaud	Maître de conférences	INSA de Lyon
Rapporteurs	Martine Lienard	Professeur	Université de Lille
	Narcis Cardona	Professeur	Universitat Politècnica de València
Examinateurs	Rodolphe Vauzelle	Professeur	Université de Poitiers
	Patrice Pajusco	Directeur d'etude	Télécom Bretagne

This thesis was prepared at Centre d'Innovation en Télécommunications et Intégration de Services (CITI), INSA de Lyon - INRIA Rhône-Alpes

Acknowledgements

Finally, I come to the final stage of my thesis. I want to say it is so hard to get here. For the acknowledgements, I think I should first thank my husband, Fuchun XIE because without him, I would not have had the courage to apply for this PhD position and believed that I could be someday a PhD in France. His constant support and love lead me where I stand today. The EU-FP7 iPLAN project which funds this thesis also deserves my appreciation. It provides me an opportunity to challenge myself and makes me know how much potential I have. I would like to thank Professor Martine LIENARD and Professor Narcis CARDONA for being kind to have accepted to review my thesis. I would like also to thank Professor Rodolphe VAUZELLE and Dr. Patrice PAJUSCO for being kind to have accepted to be the examiners of my PhD defense.

I would like to express my sincere gratitude to my supervisors, Professor Jean-Marie GORCE and Dr. Guillaume VILLEMAUD for their valuable advice/ideas and guiding me throughout my PhD study. Without their supervisions, I would hardly have come to the final stage of this thesis. I even feel lucky to have them as my supervisors because they are so nice people. Besides, I am also grateful to Professor Jie ZHANG who accepted me to work in the Ranplan company and in his fantastic CWiND team in UK for two years where I gained valuable experience for my life.

I would like to take this opportunity to give my special thanks to Dmitry UMANSKY and Guillaume DE LA ROCHE from whom I learned how to write a good scientific paper. Besides, Dmitry UMANSKY is the person who really guided me step by step in the first year

and Guillaume DE LA ROCHE is the person who is always there when I have questions about the simulator. I would like to thank also Katia JAFFRES-RUNSER for her help on the calibration engine and Nikolai LEBEDEV for the useful discussions in Ranplan.

I am happy to thank my friends and colleagues Yufang, Fei, Paul, Virgile, Anya, Gaëlle, Sandesh, Anis, Leonardo, Yuangyuang, Lusheng, Fuda, Zhaowu, Tao, Jin, Yuxin, Diala, Trista etc with whom I have spent a very happy time in the family-like CITI laboratory. Especially, I express my special thanks to Yufang, Paul and Fuda for helping me manage the PhD registration and rent the house etc when I was in UK, and Gaëlle for her constantly selfless help. I would like also to thank my friends and colleagues in UK, such as Zhihua, Xiaoming, Jialai, Jonathan, Hui, Peng, Wei, Hanye etc. Friendship is important for me, it makes me feel I am not alone.

Last but not least, I would like to thank all the members in my big family for their constant love and devotion.

Abstract

This thesis aims at proposing all the possible enhancements for the Multi-Resolution Frequency-Domain ParFlow (MR-FDPF) model. As a deterministic radio propagation model, the MR-FDPF model possesses the property of a high level of accuracy, but it also suffers from some common limitations of deterministic models. For instance, realistic radio channels are not deterministic but a kind of random processes due to, e.g. moving people or moving objects, thus they can not be completely described by a purely deterministic model. In this thesis, a semi-deterministic model is proposed based on the deterministic MR-FDPF model which introduces a stochastic part to take into account the randomness of realistic radio channels. The deterministic part of the semi-deterministic model is the mean path loss, and the stochastic part comes from the shadow fading and the small scale fading.

Besides, many radio propagation simulators provide only the mean power predictions. However, only mean power is not enough to fully describe the behavior of radio channels. It has been shown that fading has also an important impact on the radio system performance. Thus, a fine radio propagation simulator should also be able to provide the fading information, and then an accurate Bit Error Rate (BER) prediction can be achieved. In this thesis, the fading information is extracted based on the MR-FDPF model and then a realistic BER is predicted. Finally, the realistic prediction of the BER allows the implementation of the adaptive modulation scheme. This has been done in the thesis for three systems, the Single-Input Single-Output (SISO) systems, the Maximum Ratio Combining (MRC) diversity systems and the wideband Orthogonal Frequency-Division Multiplexing (OFDM) systems.

Résumé

Cette thèse a pour but de proposer toutes les avancées possibles dans l'utilisation du modèle de propagation Multi-Resolution Frequency-Domain ParFlow (MR-FDPF). Etant un modèle de propagation radio déterministe, le modèle MR-FDPF possède un haut niveau de précision, mais souffre des limitations communes à tous les modèle déterministes. Par exemple, un canal radio réel n'est pas déterministe, mais un processus aléatoire à cause par exemple des personnes ou objets mobiles, et ne peut donc être décrit fidèlement par un modèle purement déterministe. Dans cette thèse, un modèle semi-déterministe est proposé, basé sur le modèle MR-FDPF, qui introduit une part stochastique pour tenir compte des aspects aléatoires du canal radio réaliste. La partie déterministe du modèle est composée du path loss (atténuation d'espace), et la partie stochastique venant du shadow fading (masquage) et du small scale fading (évanouissement).

De même, de nombreux simulateurs de propagation radio ne proposent que la prédiction de la puissance moyenne. Mais pour une simulation précise de la propagation radio il convient de prédire également des informations de fading permettant dès lors une prédiction précise du taux d'erreur binaire (BER) potentiel. Dans cette thèse, l'information de fading est déduite des simulations MR-FDPF et par la suite des valeurs réalistes de BER sont données. Enfin, ces données réalistes de BER permettent d'évaluer l'impact de schémas de modulation adaptatifs. Des résultats sont présentés dans trois configurations : systèmes SISO (mono-antenne à l'émission et à la réception), systèmes à diversité de type MRC, et systèmes large bande de type OFDM.

Contents

List of Tables

List of Figures

List of Acronyms

3GPP	the 3rd generation partnership project
AMC	adaptive modulation and coding
AWGN	additive white gaussian noise
BEP	bit error probability
BER	bit error rate
COST	cooperation in science and technology
CDF	cumulative distribution function
CFL	Courant-Friedrichs-Lewy
EDF	empirical distribution function
EIRP	equivalent isotropically radiated power
FAPs	femto access points
FCF	frequency correlation function
FD	fading depth
FDPF	frequency domain ParFlow
FDTD	finite-difference time-domain
GO	geometrical optics
GSCMs	geometry-based stochastic channel models
GTD	geometrical theory of diffraction
LOS	line-of-sight
MGF	moment generating function
MIMO	multiple-input multiple-output
MISO	multiple-input single-output
MR	multi-resolution
MRC	maximum ratio combining
MR-FDPF	multi-resolution frequency domain ParFlow
NLOS	non-line-of-sight
OFDM	orthogonal frequency-division multiplexing
PBSs	pico base stations
PDF	probability density function
PDP	power delay profile

QoS	quality of service
RBW	resolution bandwidth
RMSE	root mean square error
SAGE	space-alternating generalized expectation maximization
SER	symbol error rate
SIMO	single-input multiple-output
SINR	Signal to Interference plus Noise Ratio
SISO	single-input single-output
SLAC	stochastic local area channel
SNR	signal-to-noise ratio
SWT	sweep time
TCF	time correlation function
UTD	uniform geometrical theory of diffraction
WINNER	wireless world initiative new radio
WSSUS	wide-sense stationary uncorrelated scattering

Chapter 1

Introduction

1.1 Context and motivation

In the past two decades, wireless telecommunications have experienced an explosive growth. On the one hand, a wide variety of advanced wireless telecommunication technologies have greatly facilitated our daily lives and thus stimulated an increasing demand for smart mobile devices, such as laptops, smart phones, tablets etc. On the other hand, the popularity of these smart mobile devices has, in turn, inspired the rapid development of wireless telecommunications.

However, the increasing demand for various smart mobile devices has led to an exponential growth of mobile traffic which has set a formidable challenge to the wireless system capacity. Due to the fact that there is a capacity limit of conventional macro-cellular systems, the concept of heterogeneous networks has been proposed so that a part of traffic can be offloaded to smaller cells. Heterogeneous networks aim at increasing the system capacity by e.g. dense frequency reuse over space. The main idea of heterogeneous networks is to overlay the conventional single-tier macro-cellular networks with one or more tiers of low power and low cost devices, e.g. base stations or access points in Microcells, Picocells, and Femtocells to increase local capacity at capacity-demanding areas [1].

In cellular networks, the term Macrocells is used to describe the cellular networks with the largest range of cell sizes. Normally, the cell sizes of Macrocells range from 1 km to 20 km [2]. Macrocells are usually used to provide radio

coverage for rural or suburban areas. For urban areas which are more capacity-demanding than rural and suburban areas, the radio coverage is usually provided by Microcells. Microcells typically have the cell sizes ranging from 500 m to 2 km. Unlike Macrocells and Microcells which provide radio coverage for wide areas, Picocells and Femtocells, by contrast, provide radio coverage for small areas. Picocells are usually used to increase local capacity of networks for small areas with very dense mobile users, for instance, shopping malls and train stations. Picocells extend radio coverage to indoor areas where outdoor signals from Macrocells or Microcells are not strong enough to provide the required quality of radio links after wall penetration. At last, Femtocells are designed for providing radio coverage in home or small offices.

By shrinking the service range and dense spatial reuse of the frequency spectrum, smaller cells (e.g. Femtocells, Picocells, Microcells compared to Macrocells) can achieve significant improvement in radio link quality and system capacity. It is believed that heterogeneous network architecture is one of the most promising low-cost approaches to increase the system capacity and improve the Quality of Service (QoS).

It is reported that about 2/3 of calls and 90% of data services occur indoors [3]. A good radio coverage is the basis to guarantee the required quality of services, thus it is extremely significant to investigate the radio propagation in indoor environments.

In the initial stages of cellular networks, the indoor radio coverage was usually provided by the outdoor signals penetrating from Macrocells or Microcells. With the development of wireless cellular networks, nowadays, the indoor radio coverage is normally provided by the indoor base stations or access points, e.g. pico base stations (PBSs) and femto access points (FAPs). Thus, the indoor radio coverage should be reinvestigated from a new perspective.

In wireless telecommunications, the term "path loss", in decibel (dB), is defined as the transmitted power minus the received power. Thus, path loss represents the signal attenuation introduced by the propagation channels [4]. It is always a positive quantity. Due to the complexity of radio propagation environments and various propagation mechanisms, in reality, the instantaneous path

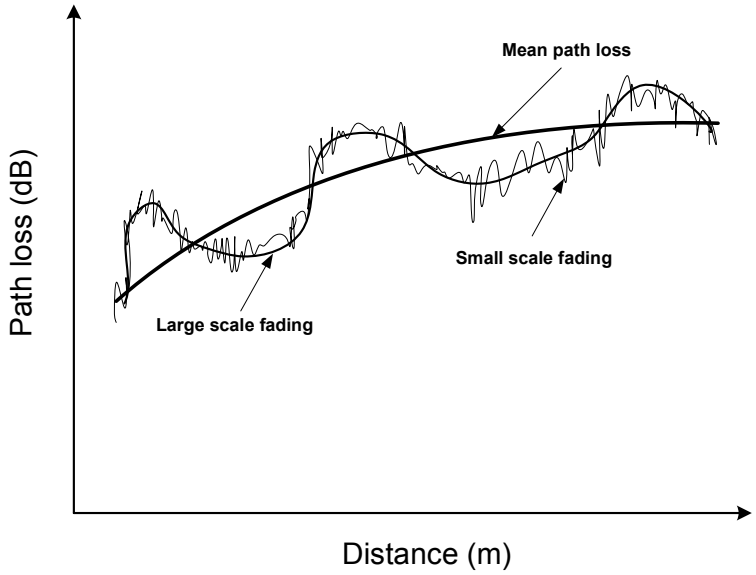

Figure 1.1: The instantaneous path loss.

loss is a combination of the mean path loss, the large scale fading and the small scale fading as shown in Fig. 1.1. Among these, the mean path loss is considered to be deterministic while the large scale fading, i.e. the shadow fading, and the small scale fading are usually described statistically. The channel models which tackle the relationship between the mean path loss and the Tx-Rx (Transmitter and Receiver) separation distances are called the path loss models. Those which tackle the large scale fading and the small scale fading are called the large scale fading models and the small scale fading models, respectively.

Although the basic propagation principle in indoor environments is similar to that of outdoor environments, the indoor radio propagation has its specificity as follows:

1. ***More reflections, diffractions and refractions are possible to occur in indoor radio propagation due to the rich presence of obstacles, such as walls and furniture etc.*** Hence, radio propagation tools whose computational efforts are independent of the number of reflections and diffractions are advantageous over those whose computational efforts are strongly dependent on the complexity of scenarios, like ray-optical tools.

2. The sizes of indoor scenarios are normally smaller than those of outdoor

scenarios. Thus ***a relatively higher computational effort per spatial unit can be afforded by radio propagation tools in order to obtain a higher level of accuracy.***

3. Unlike outdoor environments which are full of high speed moving objects and mobile users, indoor environments are usually full of low speed moving people. Hence, ***the Doppler shift in indoor environments is negligible*** [5].

The commonly used radio propagation modeling methods for indoor environments can be mainly categorized into the following four types (more details will be provided in Chapter 2):

1. ***Empirical models***: Empirical models are usually extracted from channel measurements conducted at some typical places. They are extracted by fitting the measurement data with some simplified mathematical formulas or distribution functions. Thus, empirical models are normally very easy to implement and with very low computational load. However, since empirical models are extracted from measurements conducted only at some typical places, they retain some general channel characteristics without taking into account the specific propagation environments. For a specific propagation scenario, empirical models usually suffer from a low level of accuracy. The widely used empirical models for indoor environments include, for instance, the one-slope model, wall and floor factor models, COST231 multi-wall model and linear attenuation model etc.

2. ***Stochastic models***: Stochastic models are usually used to model the random aspects of radio channels with random variables, e.g. fading characteristics of radio channels. Stochastic models require very little information of the propagation environments. For radio propagation channels, there exist two typical types of fadings: the large scale fading and the small scale fading. The large scale fading characterizes the signal strength variation over large distances [4]. On the contrary, the small scale fading characterizes the rapid fluctuations of the received signal strength over very short travel distances (usually a few wavelengths). The large scale fading and the small scale fading are usually modeled with stochastic models. For instance, the large scale fading, i.e. the shadow fading, is usually modeled to be the Log-normal fading, and the small scale fading is widely modeled to be either the Rayleigh, Rice or Nakagami-m fading etc.

3. ***Deterministic models***: Deterministic models simulate the real physical propagation phenomenon of radio waves. Deterministic models are based on the Maxwell's equations describing the behavior of electromagnetic field and take into account the specific propagation environments. Thus they usually possess a high level of accuracy. Since deterministic models take into account the specific propagation environments, they are also called site-specific models. The predicted results provided by the deterministic models are deterministic, i.e. the predicted results are always the same no matter how many times you rerun it if there is nothing changed in the simulated scenarios. Although deterministic models have the advantage of high accuracy, they have also the disadvantage of heavy computational load. Moreover, the high accuracy of deterministic models depends strongly on the accuracy of databases of the simulated scenarios. Ray-optical models and Finite-Difference Time-Domain (FDTD) models are the two widely used deterministic propagation models.

4. ***Semi-deterministic models***: Semi-deterministic models are the combinations of deterministic models and stochastic models or empirical models. Thus, semi-deterministic models benefit from both deterministic models and stochastic models or empirical models. For instance, semi-deterministic models usually require less computational time and lower computational load than deterministic models, but possess a higher level of accuracy than stochastic models or empirical models. The existing semi-deterministic models include for example, the Dominant path model, the Motif model and the Geometry-based Stochastic Channel Models (GSCMs) etc.

1.2 Objective of the thesis

This thesis was supported by the EU-FP7 iPLAN project whose main objective was to develop an automatic indoor radio network planning and optimization tool. The iPLAN project was a collaboration between INSA-Lyon, France, University of Bedfordshire, UK, and Ranplan Wireless Network Design Ltd., UK. I spent the first year of my PhD period at INSA-Lyon, France, and then the second and the third year in Ranplan Wireless Network Design Ltd. in UK.

A FDTD-like model, Multi-Resolution Frequency Domain ParFlow (MR-FDPF) model, was proposed by Gorce et al. in [6][7][8]. The MR-FDPF model falls into the deterministic models which is based on the lattice wave automata theory [9]. Since it is a deterministic model including all the radio propagation phenomena in a natural way, the MR-FDPF model possesses a high level of accuracy. Although an effort of computational efficiency has been made to the MR-FDPF model by introducing the Multi-resolution structure, which makes it more computationally efficient compared to the conventional ParFlow model [10], the MR-FDPF model is still more suitable for radio coverage prediction in indoor environments due to its high computational load. It is more suitable for indoor radio coverage prediction also because in indoor environments, the MR-FDPF mode is advantageous over the widely used ray-optical models [11] since its computational load is independent of the complexity of scenarios.

The MR-FDPF model has been proven to be fast and efficient in predicting the mean power [6][7]. However, it is known that only mean power is not enough to describe the behavior of radio channels, even not enough for determining the radio link quality. Therefore, the objective of this thesis is to propose all the possible enhancements of the MR-FDPF model so that it can provide as much as possible the knowledge of the radio channels. These can be detailed as follows:

1. The MR-FDPF model can provide a coverage map for the simulated scenarios, but this coverage map mixes the large scale fading and the small scale fading. In order to get a better insight and understanding of the radio propagation environments, we prefer to know separately the path loss model, i.e. path loss relationship with the transmitter (Tx) and receiver (Rx) distance, the standard deviation of the lognormal distributed shadow fading, and the distribution of the small scale fading. Moreover, for system level simulators, what they really need are the separated path loss models, shadow fading models and small scale fading models. Hence, ***the first objective of this thesis is to separate the large scale path loss, shadow fading and the small scale fading***.

2. As already mentioned, the MR-FDPF model is a deterministic model, which means the predicted results by the MR-FDPF model are deterministic. However, in reality, radio channels are a sort of random processes and present fading due to e.g. movements of surrounding objects. Thus, realistic radio channels

can not be completely represented by a purely deterministic result. Therefore, ***the second objective of this thesis is to improve the MR-FDPF model so that it can take into account the nature of randomness of realistic radio channels***.

3. Since only the mean power of the received signal is not enough to determine the radio link quality and describe the behavior of radio links, ***the third objective of this thesis is thus to provide a complete radio link quality prediction, e.g. the fading severity parameters, the Bit Error Rate (BER), and the achievable data rate***.

1.3 Organization and contribution of the thesis

The rest of this thesis is organized as follows:

Chapter 2 starts with an introduction of the basic propagation principles and radio propagation phenomena, and then a state-of-the-art review of the indoor radio propagation models is presented. This includes a detailed description of the widely used empirical models, stochastic models, deterministic models and semi-deterministic models.

Chapter 3 introduces first the characterization of deterministic channels. However, realistic radio channels are a kind of random processes which can not be completely described by deterministic channels. Thus, randomly time-variant linear channels are introduced in the second part of this chapter. After that, a number of parameters for radio link quality are listed and described which will be used in the latter chapters.

Chapter 4 introduces detailedly in the first section the principle of the MR-FDPF model and its level of accuracy. Then in the second section, the large scale propagation characteristics are described followed by how to extract the large scale propagation characteristics and how to separate the deterministic path loss and shadow fading based on the MR-FDPF model. In the third section, the small scale fading statistics are extracted by introducing the Stochastic Local Area Channel (SLAC) model. The parameters of the SLAC model corresponding to a specific position are estimated by the well-known Space-Alternating Generalized Expectation maximization algorithm (SAGE). The estimated parameters

of the SLAC model allow determining a number of small scale fading statistics, namely, the Power Delay Profile (PDP), the envelope Probability Density Function (PDF), the Frequency Correlation Function (FCF), the Rice K factor, the mean delay, and the root mean square delay etc. Finally, based on the extraction of the large scale propagation characteristics and the small scale fading statistics above, a semi-deterministic channel model is proposed which is based on the deterministic MR-FDPF model, but introduces a stochastic part to take into account the random aspect of the realistic radio channels. The results of the large scale propagation characteristics have been included in [12] and those of the small scale fading statistics in [13].

Chapter 5 is about the realistic prediction of the BER based on the MR-FDPF model. Two systems are tackled in this chapter: the SISO systems and the MRC diversity systems. The predicted BER is realistic because it takes into account the impact of the fading severity. Especially, for the MRC diversity systems, the correlations among diversity branches are also taken into account. This work for the prediction of the BER for the SISO systems and the MRC diversity systems has been separately published in [14][15].

Chapter 6 is about the wideband simulations based on the MR-FDPF model. Two approaches of the wideband simulations are given in the first part of this chapter. One is the straightforward repetition of the MR-FDPF simulations at multiple frequencies and the other one is an approximation approach based on the Neumann series expansion. The second part of this chapter is about the wideband multipath fast fading characteristics. By comparisons, the simulated wideband multipath fast fading characteristics from the MR-FDPF model and those from the measurements fit each other statistically. In the last part, the block adaptive modulation scheme based on the simulated multipath fast fading characteristics is implemented and the obtained average aggregate data rate and the data rate gain are verified by comparisons to the measurements. These results in Chapter 6 have been presented in [16] and [17].

Finally, conclusion and future work are given in Chapter 7.

1.4 List of publications

Journal papers

1. M. Luo, G. Villemaud, J.-M. Gorce, and J. Zhang, "Realistic Prediction of BER and AMC for Indoor Wireless Transmissions", *IEEE Antennas and Wireless Propagation Letters*, vol. 11, pp. 1084 - 1087, 2012.

2. D. Umansky, J.-M. Gorce, M. Luo, G. De la Roche, and G. Villemaud, "Computationally Efficient MR-FDPF and MR-FDTLM Methods for Multifrequency Simulations", *IEEE Transactions on Antennas and Propagation*, 61(3):1309 - 1320, 2012.

Book chapter

1. Z. Lai, G. Villemaud, M. Luo and J. Zhang, "Chapter 2 - Radio Propagation Modelling," in Book: X.Chu, D. López-Pérez, Y. Yang and F. Gunnarsson, "Heterogeneous Cellular Networks - Theory, Simulation, and Deployment", *Cambridge University Press*, 2012.

Conference papers

1. M. Luo, G. Villemaud, J.-M. Gorce, and J. Zhang, "Realistic Prediction of BER for Adaptive OFDM Systems", in *7th European Conference on Antennas and Propagation (Eucap 2013)*, Gothenburg, Sweden, April, 2013.

2. M. Luo, G. Villemaud, J. Weng, J.-M. Gorce, and J. Zhang, "Realistic Prediction of BER and AMC with MRC Diversity for Indoor Wireless Transmissions", in *IEEE Wireless Communications and Networking Conference (WCNC 2013)*, Shanghai, China, April, 2013.

3. M. Luo, N. Lebedev, G. Villemaud, G. De La Roche, J. Zhang, and J.M. Gorce, "On predicting large scale fading characteristics with the MR-FDPF method", in *6th European Conference on Antennas and Propagation (Eucap 2012)*, Prague, Czech Republic, March, 2012.

4. M. Luo, G. De la Roche, G. Villemaud, J.-M. Gorce and J. Zhang, "Simulation of Wide Band Multipath Fast Fading Based on Finite Difference Method", in *IEEE 74th Vehicular Technology Conference (VTC 2011-Fall)*, San Francisco, United States, September, 2011.

5. M. Luo, D. Umansky, G. Villemaud, M. Lafort, and J.-M. Gorce, "Estimating channel fading statistics based on radio wave propagation predicted with deterministic MR-FDPF method", in *5th European Conference on Antennas and Propagation (Eucap 2011)*, Rome, Italy, April, 2011.

Others

Presentations

1. "On Predicting Large Scale Fading Characteristics with a Finite Difference Method", in *5th International Workshop on Femtocells*, London, UK, 13-14 February, 2012.

2. "On Predicting Large Scale Fading Characteristics with a Finite Difference Method", in *3rd IC1004 MC and Scientific Meeting (TD(12)03023)*, Barcelona, Spain, 8-10 February, 2012.

3. "Simulation of Wide Band Multipath Fast Fading Based on Finite Difference Method", in *1st International Workshop on Planning and Optimization of Wireless Networks*, Sheffield, UK, 14-15 September, 2011.

4. "Estimating Channel Fading Statistics based on Radio Wave Propagation Predicted with Deterministic MR-FDPF Method", in *International Workshop on Propagation and Channel Modeling for Next-Generation Wireless Networks*, Lyon, France, 2-4 March, 2011.

Report

1. M. Luo, D. Umansky, G. Villemaud, and J.-M. Gorce, "D1.2: Progress Report: The Prediction of Small Scale Fadings in Radio Propagation Based on the MR-FDPF Method", 2011.

Chapter 2

Background and state of the art

In this chapter, we first give a brief introduction of the basic radio propagation mechanisms, and then make a state-of-the-art survey of the indoor radio propagation models, mainly on the path loss models and fading models. The existing indoor radio propagation models can be mainly categorized into four groups: empirical models, stochastic models, deterministic models and semi-deterministic models. After a detailed description of these radio propagation models, a clear understanding of their advantages and disadvantages will be had. This chapter provides the background knowledge for the following chapters.

2.1 Radio propagation mechanisms

The basic radio propagation mechanisms include reflection, refraction and diffraction.

From the radio propagation perspective, the effect of a medium can be determined by three parameters: conductivity σ, permittivity ε and permeability μ. These three parameters are known as the constitutive parameters of the medium [18].

In lossless media, when a plain wave propagates from a medium with permittivity ε_1 and permeability μ_1 to another medium with different permittivity ε_2 and permeability μ_2, reflection and refraction will happen at the boundary of these two media (see Fig. 2.1). The two produced reflection and refraction waves have exactly the same frequency as the incident wave. The directions of the two

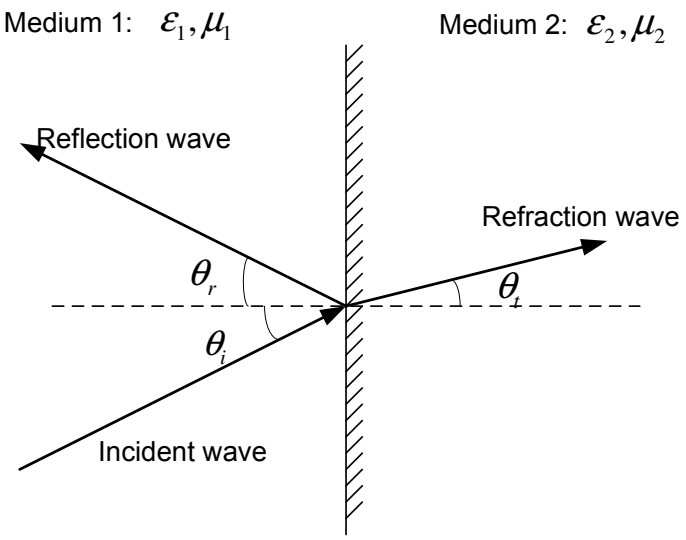

Figure 2.1: Reflection and refraction.

waves follow the Snell's law of reflection (Eq. 2.1) and the Snell's law of refraction (Eq. 2.2), respectively, as follows

$$\theta_r = \theta_i \tag{2.1}$$

$$\frac{\sin\theta_t}{\sin\theta_i} = \frac{n_1}{n_2} \tag{2.2}$$

where θ_i, θ_r and θ_t are the incident angle, reflection angle and refraction angle, respectively. The parameter n is the refractive index which depends on the relative permittivity ε_r and relative permeability μ_r of media according to

$$n = \sqrt{\varepsilon_r \mu_r} \tag{2.3}$$

The ε_r and μ_r are the medium's permittivity and permeability expressed relative to those of vacuum.

Above, we have assumed the boundary or surface between the two media is a perfectly smooth surface. The reflection in this case is usually termed specular reflection. When the surface is getting rougher, there will be also an amount of scattered waves around the main reflection wave. Scattering is a special case of reflection, which describes the phenomenon that radio waves are reflected in many directions by irregular objects or rough surfaces.

Diffraction is typically described as the phenomenon that radio waves bend around small obstacles or spread out past small openings. Diffraction explains the field leakage in the shadow region behind obstacles. Diffraction can be explained by Huygens' principle [19] which states that every element in the wavefront can be a source of a spherical wavelet and the envelope of all these wavelets forms another secondary wavefront in the subsequent time. Radio waves do propagate into the shadow region of an obstacle. But how much is the field strength of the diffraction waves behind the obstacle? It is very complicated depending on the specific situations in reality. How to accurately model diffractions is one of the most difficult task in radio propagation modeling. The easiest model is the single knife-edge model which considers only one perfect absorbing plane existing between the transmitter and receiver [18]. Although the single knife-edge model provides an acceptable prediction of diffractions for some cases and gives us an insight to how the position of the knife-edge impacts the diffraction waves, in reality, there are other cases where it is necessary to take into account more details of the obstacles, e.g. the shape and the property of the materials. Thus Geometrical Theory of Diffraction (GTD) was proposed in the 1950s by Joseph Keller [20] and it can be implemented by the well known ray-optical methods [11]. In the 1970s, GTD was improved and extended to the Uniform GTD (UTD) [21] in order to overcome the false prediction of GTD in the transition region (region close to the shadow boundary).

2.2 State of the art of indoor radio propagation models

There exist many kinds of radio propagation models [4][18][22][23][24][25]. For instance, from the bandwidth's prospective, we have narrowband models and wideband models. Narrowband models can be further divided into the path loss models, large scale fading models and small scale fading models etc. Similarly, wideband models can also be further divided into the Tapped delay line models, models for the Power Delay profile, and models for the Arrival Times of Rays and Clusters etc [23]. From the modeling methods' prospective, we have empirical

models, stochastic models, deterministic models and semi-deterministic models. From the application scenarios' perspective, we have indoor radio propagation models and outdoor radio propagation models. Here in this chapter, we mainly focus on the indoor narrowband radio propagation models. In the following section, we will start with the free space propagation model, and then introduce the empirical models, stochastic models, deterministic models and semi-deterministic models for indoor environments successively.

2.2.1 Free space propagation model

The simplest radio propagation scenario is the free space propagation, which means there is absolutely no any obstacle between the transmitter and the receiver. According to the Friis' law (Friis free space equation), the received power by a receiver antenna which is separated from the transmitter by a distance d is [23]

$$P_r(d) = P_t \cdot G_t \cdot G_r \cdot \left(\frac{\lambda}{4\pi d}\right)^2 \tag{2.4}$$

where $P_r(d)$ is the received power at the Tx-Rx separation distance d, P_t is the transmitter power, G_t and G_r are the transmitter and receiver antenna gains, respectively. λ is the wavelength.

If we write it in the logarithmic scale, it is then

$$P_r|_{dBm}(d) = P_t|_{dBm} + G_t|_{dBi} + G_r|_{dBi} + 20\log\left(\frac{\lambda}{4\pi d}\right) \tag{2.5}$$

where $|_{dBm}$ and $|_{dBi}$ mean in dBm and dBi, respectively, and $\log(\cdot)$ represents the base 10 logarithm.

When antenna gains are excluded, the free space path loss model is thus

$$PL(d) = 20\log\left(\frac{4\pi d}{\lambda}\right) = 20\log\left(\frac{4\pi}{\lambda}\right) + 20\log(d) \tag{2.6}$$

The term $20\log(d)$ indicates that the free space path loss increases at a rate of 20 dB per decade (one decade means ten times' increase in the distance between the transmitter and the receiver).

Inspired by the free space path loss formula above, a number of empirical path loss models are constructed in the similar form of

$$PL(d) = a + 10 \cdot n \cdot \log(d) \tag{2.7}$$

where a is a constant path loss at a reference distance, and n is called the path loss exponent which depends strongly on the propagation environments. For the free space propagation, the path loss exponent is 2. It is reported that the path loss exponent can usually range from 1.6 to 6.5 [26]. For instance, urban Macrocells normally have a big path loss exponent, whereas indoor office buildings usually have a low value where wave guide effect can possibly happen.

2.2.2 Empirical models

Empirical models [18][24][27][28][29][30][31] are constructed either based on simplifying assumptions concerning the physical geometry of the propagation environments or based on a best fit to extensive measurement data conducted in a typical environment. Empirical models usually consider the path loss as function of some meaningful parameters like distance, frequency, antenna heights. Empirical models characterize radio channels by their average behavior. Since some simplifications have been made more or less during the establishing of empirical models, they usually require very low computation effort and are very easy to implement. However, they have the disadvantage of low accuracy for a specific scenario because they do not take the specific propagation environment into account. Empirical model are widely used in network design due to the low computational time and computation load.

2.2.2.1 One-slope model

The one-slope model [24][30] assumes that the path loss in dB is linearly dependent on the logarithmic Tx-Rx distance

$$PL(d) = L_0 + 10 \cdot n \cdot \log(d) \tag{2.8}$$

where L_0 is the path loss at the Tx-Rx distance of 1 meter and n is the path loss exponent. Obviously, this model is based on the form of the free space model and

aims at including all the losses due to various propagation mechanisms by the path loss exponent. This model is very easy to implement, but it can sometimes lead to large errors because, in indoor environments, a large variability in propagation mechanisms is possible among different offices and buildings.

2.2.2.2 Wall and floor factor models

The wall and floor factor models [31] are based on the free space path loss. They assume that the indoor path loss is the free space path loss plus an additional loss related to the number of floors n_f and the number of walls n_w intersected with the straight line between the transmitter and the receiver.

$$PL(d) = L_1 + 20\log(d) + n_f L_f + n_w L_w \tag{2.9}$$

where L_1 is the path loss at the Tx-Rx distance d of 1 meter, L_f and L_w are the penetration losses caused per floor and per wall, respectively. The term $20\log(d)$ is the free space path loss factor.

The wall and floor factor models perform better than the one-slope model since they provides more degrees of freedom than the latter.

2.2.2.3 COST231 multi-wall model

The COST231 multi-wall model [18][24] is a further improved version of the wall and floor factor models. It takes into account the fact that overall penetration loss has a nonlinear dependence with the number of penetrated floors [18][30][32]. The COST231 multi-wall model can be expressed as follows

$$PL(d) = L_{FS} + L_C + \sum_{i=1}^{W} L_{wi} n_{wi} + L_f n_f^{\left(\frac{n_f+2}{n_f+1} - b\right)} \tag{2.10}$$

where L_{FS} is the free space path loss for the straight-line path between the transmitter and receiver, L_{wi} is the penetration loss for a wall of type i, n_{wi} is the number of walls of type i, W is the number of wall types, n_f is the number of floors, L_f is the penetration loss per floor, b and L_C are constants which are determined empirically.

For practical reasons, the number of different wall types should not be too large in order to avoid to be too complicated.

2.2.2.4 Linear attenuation model

Unlike the one-slope model, the linear attenuation model assumes that the path loss in dB is linearly dependent on the Tx-Rx distance (in meter)

$$PL(d) = L_{FS} + \alpha_n \cdot d \tag{2.11}$$

where α_n (dB/m) is the attenuation coefficient. In some studies, additional wall loss terms are added to this model in order to improve the performance [24][33].

The four empirical models above just give the forms of the models, the parameters there should be optimized based on the measurement data. An example of these parameter values could be found in [24].

2.2.3 Stochastic models

Stochastic models are those whose results are random each time, but their statistical characteristics, e.g. Probability Density Function (PDF) follow a certain law. In general, stochastic models use one or more random variables to model the random aspects of radio channels. Stochastic models are usually used to model all kinds of fadings, e.g. the large scale fading and the small scale fading, since fadings are with the nature of randomness. For instance, the small scale fading was reported to follow Rayleigh distributions for Non-Line-Of-Sight (NLOS) scenarios and Rice distributions for Line-Of-Sight (LOS) scenarios [4][25]. The large scale fading was observed to follow log-normal distributions [24].

The small scale fading, also named the multipath fading, is due to the constructive and destructive combinations of multipath signals with random amplitudes and phases. Thus, the small scale fading is the rapid fluctuations of the received signal amplitude over usually a few wavelengths. Moreover, the mean of the small scale fading is also a random process due to the shadowing from obstacles existing between the transmitters and receivers. The variation of the mean of the small scale fading is called the large scale fading, or the shadow fading. Therefore, the large scale fading models tackle the variation of the mean of the received signal averaged over a few wavelength (remove the small scale fading).

The widely used small scale fading models include the Rayleigh fading model, the Rice fading model and the Nakagami-m fading model etc. The large scale fading models include the Log-normal fading model etc.

2.2.3.1 Rayleigh fading model

The Rayleigh fading model is widely used to model multipath fading when there is no LOS path. In NLOS scenarios, the received signal amplitude α is distributed according to the Rayleigh distribution

$$P_\alpha(\alpha) = \frac{2\alpha}{\Omega}\exp(-\frac{\alpha^2}{\Omega}), \qquad \alpha \geq 0 \tag{2.12}$$

where $\Omega = \overline{\alpha^2}$ is the average power of the fading.

2.2.3.2 Rice fading model

The Rice distribution is also known as the Nakagami-n distribution. Unlike the Rayleigh fading model, the Rice fading model is usually used to model the multipath fading when there is a direct LOS path. In LOS scenarios, the received signal amplitude α is distributed according to the Rice distribution

$$P_\alpha(\alpha) = \frac{2(1+n^2)e^{-n^2}\alpha}{\Omega}\exp(-\frac{(1+n^2)\alpha^2}{\Omega})I_0(2n\alpha\sqrt{\frac{1+n^2}{\Omega}}), \qquad \alpha \geq 0 \tag{2.13}$$

where n is the Nakagami-n fading parameter ranging from 0 to ∞. This parameter n is related to the well-known Rice K factor by $K = n^2$ which is defined as the ratio of the power of the LOS component to all the NLOS compenents (usually called diffuse components). It is of importance to note that in the extreme case when the LOS component tends to 0, e.g. K and $n \to 0$, the Rice distribution reduces to the Rayleigh distribution. And when K and $n \to \infty$, the Rice distribution approaches to the Gaussian distribution.

2.2.3.3 Nakagami-m fading model

The Nakagami-m fading distribution is given as follows [34]

$$P_\alpha(\alpha) = \frac{2m^m\alpha^{2m-1}}{\Omega^m\Gamma(m)}\exp(-\frac{m\alpha^2}{\Omega}), \qquad \alpha \geq 0 \tag{2.14}$$

where m is called the m parameter of the Nakagami-m fading and $\Gamma(\cdot)$ is the gamma function. The Nakagami-m fading model has been received extensive attention since it gives the best fit to many measurement data, such as, land-mobile and indoor-mobile multipath propagation [25][35]. The parameter m varies from $\frac{1}{2}$ to ∞ indicating the severity of the fading. The smaller the m value is, the severer the fading becomes. The Nakagami-m distribution includes the Rayleigh distribution when $m = 1$ and the one-sided Gaussian distribution when $m = \frac{1}{2}$ as special cases. When $m \to \infty$, the Nakagami-m fading channel approaches to a nonfading Additive White Gaussian Noise (AWGN) channel. When $m > 1$, we have a one-to-one mapping between the Nakagami-m distribution and the Rice distribution by their parameters

$$\mathrm{m} = \frac{(1+K)^2}{1+2K}, \qquad K \geq 0 \tag{2.15}$$

where K is the Rice K factor. Hence, the Nakagami-m fading model can describe a very wide range of multipath fading.

2.2.3.4 Log-normal fading model

Measurements reveal that the shadow fading can be modeled by the Log-normal fading model both for outdoor and indoor environments [36][37]. That is the distribution of the mean received signal power in dBW $\psi_{dBW} = 10\log E[\alpha^2]$ follows

$$P_{\psi_{dBW}}(\psi_{dBW}) = \frac{1}{\sqrt{2\pi}\sigma_{\psi_{dBW}}} \exp\left(-\frac{(\psi_{dBW} - \mu_{\psi_{dBW}})^2}{2\sigma^2_{\psi_{dBW}}}\right) \tag{2.16}$$

or the distribution of the mean received signal power in linear scale $\psi = E[\alpha^2]$ follows

$$P_{\psi}(\psi) = \frac{\xi}{\sqrt{2\pi}\psi\sigma_{\psi_{dBW}}} \exp\left(-\frac{(10\log\psi - \mu_{\psi_{dBW}})^2}{2\sigma^2_{\psi_{dBW}}}\right), \ \ \psi > 0 \tag{2.17}$$

where $\xi = 10/\ln 10$, $\mu_{\psi_{dBW}}$ and $\sigma_{\psi_{dBW}}$ are the mean and the standard deviation of ψ_{dBW}, respectively. Normally, the $\mu_{\psi_{dBW}}$ can be determined from the mean path loss, i.e. the path loss models.

2.2.4 Deterministic models

Deterministic models simulate radio wave propagation based on the Maxwell's equations and take the radio propagation environments into account. They simulate the physical phenomenons of radio waves, e.g. reflections, refractions and diffractions. Deterministic models usually possess a high level of accuracy even if their high accuracy is only achieved when the databases of the simulated scenarios are firstly accurate. Deterministic models can usually yield both the narrowband and wideband information of radio channels.

There are two main types of deterministic models: Ray-optical models and Finite-difference time-domain (FDTD) like models. Moreover, Ray-optical modes can be further divided into two subtypes: the ray launching model and the ray tracing model. FDTD-like models also have some subtypes such as, the conventional FDTD model, the time domain ParFlow model and the frequency domain ParFlow model.

2.2.4.1 Ray launching model

The ray launching model [38] is based on the Geometrical Optics (GO) which simulates the radio wave propagation according to the physical phenomenons, such as reflections, refractions and diffractions. The ray launching model actively launches a number of rays from the transmitter end. These rays are separated by a small angle, so each of them is with a different transmit direction. After launched, the rays interact with the objects in the propagation environments according to the reflection, refraction and diffraction theory (see Fig. 2.2). The propagation of a ray is terminated either when its power falls below a predefined threshold or when its number of interactions with objects reaches a predefined number or the receiver is reached. The ray launching model has an inherent disadvantage that distant objects may be missed by rays even if the separation angle between rays is very small at the transmitter (see Fig. 2.3). Ray launching is usually called the 'brute force' method since it has to launch many rays at very similar angles [37].

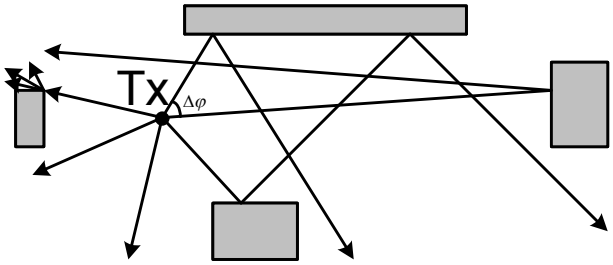

Figure 2.2: Ray launching.

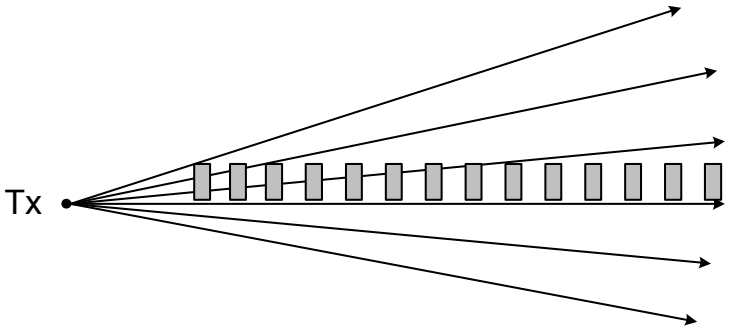

Figure 2.3: Distant objects may be missed by rays.

2.2.4.2 Ray tracing model

Unlike the ray launching model which traces rays forwards, the ray tracing model traces rays backwards. The ray tracing [37] model is an image-based model which assumes all objects in the propagation environments are potential reflectors. In implementations, the ray tracing model uses the images of the transmitter relative to all the reflectors, i.e. all the objects in the propagation environments to determine the directions of the reflected rays. Compared to the ray launching model, the ray tracing model has some advantages. For the ray launching, it has to launch a large amount of rays from the transmitter, but for a specific receiver, only few of them may finally reach the receiver and most of these rays would be a waste. Hence, for the point-to-point prediction, ray launching is not efficient. However, in the opposite, ray tracing considers only the paths which really exist between the transmitter and the receiver. Therefore, ray tracing often requires much less computation time than ray launching. But ray tracing has the disadvantage that its computational time grows exponentially with the order of

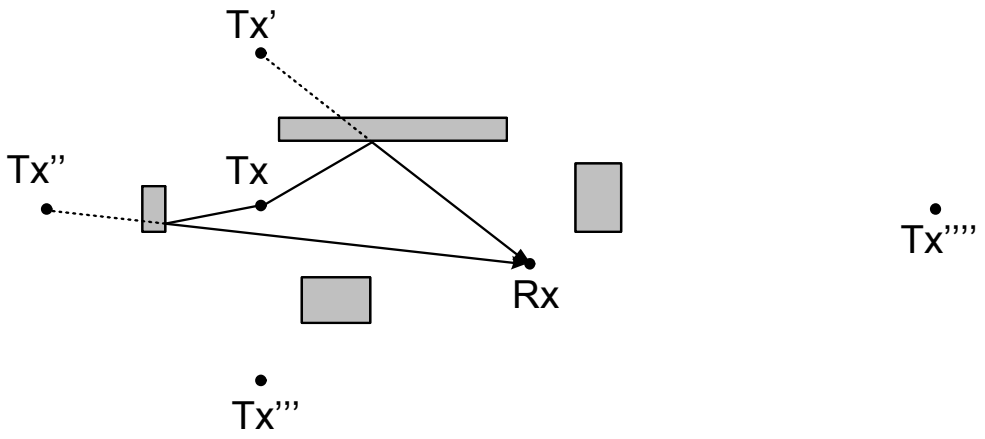

Figure 2.4: Ray tracing.

calculated reflections.

Both in the ray launching and ray tracing models, the strengths of reflected rays and refracted rays are computed according to the geometrical optics. The diffracted rays are computed according to e.g. UTD theory. For ray launching and ray tracing, the complexity of the propagation environments has a strong impact on their computational load since more obstacles lead to more reflections and diffractions etc.

2.2.4.3 FDTD model

Here, the FDTD model means the conventional FDTD model. The FDTD model [39][40][41][42] is a numerical solution of Maxwell's equations.

Since Maxwell's equations were first published in 1861 [43], they have been considered as the most accurate and elegant description about how electric field and magnetic field interact with each other and how electromagnetic waves propagate. However, Maxwell's equations are a set of partial differential equations which are very difficult to solve. In 1966, Yee proposed to approximately solve them based on a space-time grid [39] (see Fig. 2.5). The idea is that we replace the set of partial differential equations of Maxwell's equations by a set of finite-difference equations and then this set of finite-difference equations can be solved iteratively based on the space-time grid. This space-time grid is thus named the

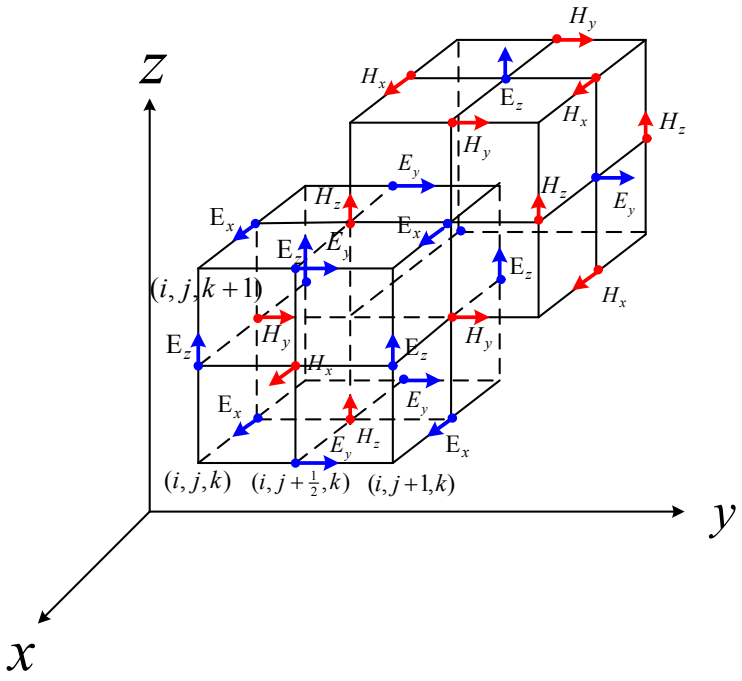

Figure 2.5: Yee grid.

Yee grid. In the 1980s, this method was further developed by Taflove and he coined the term of FDTD [40].

Since the FDTD model approximately solves the Maxwell's equations, the nature of high accuracy is its main advantage. Moreover, since in the iterative process, the finite-difference equations have already taken into account the constitutive parameters (i.e. conductivity σ, permittivity ε and permeability μ) of objects, all the effects of objects or obstacles in the propagation environments have been included by the FDTD model in a natural way. Hence, the complexity of the propagation environments (e.g. the number of obstacles existing in the propagation environments) will not impact the computational load of the FDTD model, which is a very useful property for complicated propagation environments, e.g. indoor environments. The main disadvantage of FDTD model is its high computational load. As we know, in the FDTD model, Maxwell's equations are solved on a space-time grid. In order to avoid the problem of numerical unstability [44], the size of this grid step should not be too large relative to the wavelength (i.e. should satisfy the Courant-Friedrichs-Lewy (CFL) stability condition [45]), which

makes the required computational load high.

2.2.4.4 ParFlow model

Here, the ParFlow model means the conventional time domain parFlow model. An intuitive interpretation of ParFlow models is the discrete form of Huygens principle which states that every point of a wavefront may be considered as the source of secondary wavelets. The ParFlow model can be viewed as a discrete solution of Maxwell's equations which determines its nature of high accuracy.

The ParFlow model is based on the cellular automata formalism [46][47]. In this model, simulated scenarios should be first discretized into a 2D grid-based structure and the scalar electrical field strength at a grid point r is supposed to be the sum of the fictitious flows traveling along the connection lines between the grid point r and its neighbor four grid points. From the discrete time instance $n\Delta t$ to $(n+1)\Delta t$ (where Δt is the time step), the fictitious flows can travel to their neighbor grid points, such as the flows $\{f_E, f_W, f_S, f_N\}$ or remain at rest as the stationary flow (also called the inner flow) $\breve{f}_0$ in Fig. 2.6. The flows coming into the grid point are called the inward flows, whereas the flows leaving it are called the outward flows. Noted that the inward flows of a grid point r are the outward flows of its neighbor grid points and vice versa. That is

$$\overleftarrow{f}_d(r+\Delta r, t) = \vec{f}_d(r, t-\Delta t), \quad d \in E, W, S, N \tag{2.18}$$

where Δr is the space step between any two neighbor grid points. The space step Δr satisfies the following conditions

$$\Delta r = c_0\sqrt{2}\Delta t, \quad \Delta r \ll \lambda \tag{2.19}$$

where c_0 is the speed of electromagnetic wave in the propagation medium and λ is the wavelength.

The discrete time evolution of the flows should obey the following local scattering equation so that it satisfies the Maxwell's equations

$$\vec{F}(r,t) = \Sigma(r)\overleftarrow{F}(r, t-\Delta t) + \vec{S}(r,t) \tag{2.20}$$

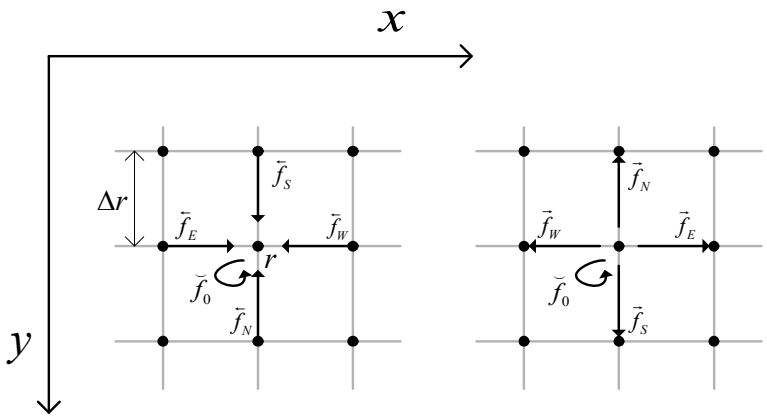

Figure 2.6: Inward and outward flows

where the inward flows vector $\overleftarrow{F}(r,t)$, the outward flows vector $\vec{F}(r,t)$, and the source flows vector $\vec{S}(r,t)$ are defined, respectively, as follows

$$\begin{aligned}
\overleftarrow{F}(r,t) &= [\overleftarrow{f}_E(r,t)\ \ \overleftarrow{f}_W(r,t)\ \ \overleftarrow{f}_S(r,t)\ \ \overleftarrow{f}_N(r,t)\ \ \breve{f}_0(r,t)]^T \\
\vec{F}(r,t) &= [\vec{f}_E(r,t)\ \ \vec{f}_W(r,t)\ \ \vec{f}_S(r,t)\ \ \vec{f}_N(r,t)\ \ \breve{f}_0(r,t)]^T \\
\vec{S}(r,t) &= [\vec{s}_E(r,t)\ \ \vec{s}_W(r,t)\ \ \vec{s}_S(r,t)\ \ \vec{s}_N(r,t)\ \ \ 0]^T
\end{aligned} \tag{2.21}$$

The operator $[\cdot]^T$ signifies the matrix transposition. The stationary flow $\breve{f}_0(r,t)$ models the dielectric media with the relative permittivities $\varepsilon_r \neq 1$. The local scattering matrix $\Sigma(r)$ in Eq. 2.20 is

$$\Sigma(r) = \frac{1}{2n_r^2}\begin{pmatrix} 1 & \alpha_r & 1 & 1 & Y_r \\ \alpha_r & 1 & 1 & 1 & Y_r \\ 1 & 1 & 1 & \alpha_r & Y_r \\ 1 & 1 & \alpha_r & 1 & Y_r \\ 1 & 1 & 1 & 1 & \beta_r \end{pmatrix} \tag{2.22}$$

where n_r is the refraction index and $\alpha_r = 1 - 2n_r^2$; $\beta_r = 2n_r^2 - 4$; $Y_r = 4n_r^2 - 4$.

In addition, according to the Luthi's proposal [9], the local scattering matrix should be adapted to introduce the effect of absorption, thus the final local scattering matrix should be

$$\Sigma_a(r) = a_r \cdot \Sigma(r) \tag{2.23}$$

where a_r is the normalized absorption coefficient.

The local scattering equation can be efficiently solved by a cellular automaton and then the electric field is given by

$$\Psi(r,t) = \frac{1}{n_r^2}\left(\sum_{d=E,W,S,N} \overleftarrow{f}_d(r,t) + Y_r \breve{f}_0\right) \tag{2.24}$$

2.2.4.5 Multi-Resolution Frequency Domain ParFlow model

The MR-FDPF model was proposed by Gorce et al. in [6][7] and represents the frequency-domain version of the ParFlow model. The ParFlow model is transferred into the frequency domain by the Fourier transform because it has several advantages in the frequency domain (more details will be stated in Chapter 4):

1. In the frequency domain, the inner flow can be removed from the formulation, thus only operating with the border flows (i.e. the inward flows and outward flows) is enough.

2. In the frequency domain, the local scattering equation becomes a linear equation after taking advantage of the relationship between the inward flows and outward flows and properly combining the local scattering matrix.

3. The further optimization can be performed to reduce the high computational load, e.g. by introducing the Multi-Resolution (MR) structure.

In the frequency domain, after appropriate processes of the border flows and the local scattering matrix, the final linear local scattering equation can be expressed as

$$\underline{\overleftarrow{F}}(v) = \underline{\tilde{\Sigma}} \cdot e^{-j2\pi v \Delta t} \underline{\overleftarrow{F}}(v) + \underline{\overleftarrow{S}}(v) \tag{2.25}$$

where v denotes the frequency and $\underline{\overleftarrow{F}}(v)$, $\underline{\overleftarrow{S}}(v)$, $\underline{\tilde{\Sigma}}$ are the global inward flow vector, the global source inward flow vector, and the global scattering matrix, respectively.

Thus in the frequency domain, the field strength prediction becomes a linear matrix inversion problem

$$\underline{\overleftarrow{F}}(v) = \left(I - \underline{\tilde{\Sigma}} \cdot e^{-j2\pi v \Delta t}\right)^{-1} \underline{\overleftarrow{S}}(v) \tag{2.26}$$

where I is the identity matrix.

Due to the huge size of the matrix corresponding to the discretization of simulated scenarios, the direct matrix inversion is usually unbearable. Therefore,

a MR structure is proposed to provide a computationally efficient way to solve this problem in the MR-FDPF model. The MR structure is based on the binary tree of the simulated scenarios obtained from the preprocessing stage. The MR structure allows the MR-FDPF model to exploit recursively the relationship between the stationary flows, the inward flows and the outward flows associated with each MR node and thus the matrix inversion problem can be indirectly solved. Besides, the preprocessing also greatly accelerates the MR-FDPF model. The preprocessing gathers the main computational load of the MR-FDPF model, but it just needs to be run once even if there are multiple signal sources.

Both the ParFlow model and the MR-FDPF model take into account all the radio propagation effects, e.g. reflections, diffractions and refractions, and the computational load does not depend on the number of reflections. However, it is shown that the space discretization step Δr should be at least six times smaller than the wavelength in order to get a good propagation prediction [9]. The smaller the space discretization step is, the higher the computational load becomes. Therefore, the main drawback of the ParFlow models is the high computational time and load, which can be partly addressed by using a lower fake frequency [9][46].

2.2.5 Semi-deterministic models

Semi-deterministic models are the combinations of deterministic models and stochastic models or empirical models. They are aiming at improving the efficiency of purely deterministic models. For instance, one example of semi-deterministic models can be to calculate the main signal paths by a deterministic model, but to take into account other diffuse paths by an empirical model or stochastic model. This way, the computational load and time from the deterministic model is reduced.

2.2.5.1 Dominant path model

The dominant path model was proposed by Wölfle et al. in [32][48][49][50]. It was proposed based on the fact that in most cases, 90% of the signal energy is contributed by one propagation path. The dominant path model overcomes

the disadvantage of ray-optical models that ray-optical models need to trace and compute a large number of rays (most of the rays contribute very little) and their accuracy has a strong dependence on the accuracy of building databases. For dominant path model, the dominant path is not a really existing physical path, but an equivalent path representing a group of similar paths optimized either by neural networks or by empirical regression [48]. So the inaccuracy of building databases has very little influence on the accuracy of the prediction. The dominant path model can usually achieve or even exceed the accuracy of ray-optical models with a much less computational time.

2.2.5.2 Motif model

The Motif model [51][52][53] was first proposed by Pechač et al. as a combination of deterministic models and empirical models. It is a modified version of the ray launching model. The Motif model introduces a probability radiation pattern to control the subsequent directions of the rays impinging on obstacles. This probability radiation pattern is determined by three probabilistic parameters: the probability of absorption, the probability of reflection and the probability of diffuse scattering, which take into account the three basic propagation phenomenons: absorption, reflection and diffuse scattering. These probabilistic parameters are optimized by measurements. Since the Motif model does not require to know the electrical properties of materials and avoid the Fresnel equations and any other complex computations, the required computational time and load are reduced compared to a conventional ray launching model.

2.2.5.3 Geometry-based stochastic channel models

Geometry-based channel models calculate the received signal based on the locations of scatterers in the propagation environments. Unlike deterministic geometry-based models, e.g. ray tracing, whose locations of scatters are prescribed according to the specific propagation environment, the Geometry-based Stochastic Channel Models (GSCMs) choose their locations of scatters and clusters (a collection of scatterers) in a stochastic way [22][54][55][56]. For instance, the GSCMs choose the locations of the scatters and clusters, or even the number

of the scatterers and clusters according to a certain distribution function. Each realization provides a different propagation channel. Therefore, the advantage of the GSCMs is that they can simulate a wide variety of radio channels, and for a specific radio propagation scenario, the GSCMs take into account of the nature of randomness. But on the other hand, for a specific propagation scenario, how to find the correct parameters associated to the specific scenario, e.g. the distribution function of the locations of the scatters, is the most difficult task.

The GSCMs are widely used by the European Cooperation in Science and Technology (COST) community, the Wireless World Initiative New Radio (WINNER) partners and the 3rd Generation Partnership Project (3GPP).

2.3 Chapter summary

In this chapter, we first introduced the three basic propagation mechanisms: reflection, refraction and diffraction. And then the free space propagation was described which is the ideal and simplest propagation case, but it provides us an insight of how signal is attenuated with the Tx-Rx distances. The form of the free space path loss model is thus popularly adopted by empirical models.

For the indoor radio propagation models, we categorized them mainly into four groups: empirical models, stochastic models, deterministic models and semi-deterministic models. Empirical models usually consider the path loss as function of some meaningful parameters such as distance, frequency, antenna heights etc. The parameters in empirical models are optimized according to a best fit to measurement data. Since empirical models are just functions of distance and frequency etc, they are usually very easy to implement and require very low computational load. However, they have the disadvantage of low accuracy for a specific scenario because they do not take the specific propagation environment into account. Stochastic models are those which use random variables to model the random aspects of radio channels. The PDFs of the random variables follow a certain law according to the observations from intensive measurements. Like empirical models, the stochastic models are also easy to implement and have a low level of accuracy for a specific scenario. Deterministic models simulate radio wave propagation based on the Maxwell's equations and they take the specific

radio propagation environments into account. Thus, deterministic models usually possess a high level of accuracy for a specific scenario and most of them, e.g. ray launching and FDTD, can provide a coverage map for the whole simulated area, i.e. not just a point-to-point prediction. But their main disadvantages are firstly the high computational load and secondly the strong dependence of the prediction accuracy on the accuracy of the building databases. The semi-deterministic models are the combinations of deterministic models and stochastic models or empirical models which aim at either improving the computational efficiency of purely deterministic models or introducing a stochastic part to model the randomness of realistic radio channels since realistic radio channels are a kind of random processes due to moving objects.

This chapter provides a clear understanding of the existing indoor radio propagation models. The understanding of the characteristics associated to each radio propagation model allows an easy understanding of the following chapters, especially Chapter 4.

Chapter 3

Radio link quality evaluation

After a state-of-the-art survey of the existing indoor radio propagation models in Chapter 2, this chapter mainly talks about the characterization of deterministic channels and randomly time-variant linear channels and then a number of parameters used to evaluate the radio link quality will be introduced. These parameters include such as the mean received signal power, the SNR, the SINR, the Probability Density Function (PDF), the outage probability, the level-crossing rate, the average fade duration, the BER and the throughput. Most of these parameters will be extracted based on the deterministic MR-FDPF model in the latter chapters.

3.1 Characterization of deterministic channels

The radio propagation channel can be considered as a time-variant linear filter which transforms input signals into output signals. Since the input signal and output signal can be described in both the time and frequency domain, there exist totally four system functions to describe the behavior of the channel, i.e., the time-variant impulse response, the time-variant transfer function, the Doppler-variant impulse response and the Doppler-variant transfer function [23].

Time-variant impulse response

Mathematically, the radio propagation channel can be represented by a time-variant impulse response $h(t, \tau)$ as shown in Fig. 3.1 and the received signal

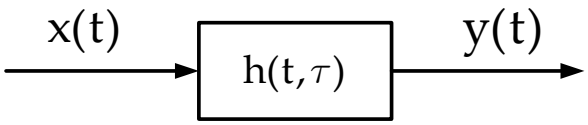

Figure 3.1: Radio propagation channels.

$y(t)$ can be obtained by convolving the transmit signal $x(t)$ with the time-variant impulse response $h(t,\tau)$

$$y(t) = \int_{-\infty}^{\infty} x(t-\tau)h(t,\tau)d\tau \tag{3.1}$$

Time-variant transfer function

Applying the Fourier transform to the time-variant impulse response $h(t,\tau)$ with respect to the variable τ leads to the time-variant transfer function $H(t,f)$

$$H(t,f) = \int_{-\infty}^{\infty} h(t,\tau)\exp(-j2\pi f\tau)d\tau \tag{3.2}$$

The relationship between the transmit signal $x(t)$ and the received signal $y(t)$ is given by

$$y(t) = \int_{-\infty}^{\infty} X(f)H(t,f)\exp(j2\pi ft)df \tag{3.3}$$

Doppler-variant impulse response

Similarly, applying the Fourier transform to the time-variant impulse response $h(t,\tau)$ with respect to the variable t leads to the Doppler-variant impulse response $s(v,\tau)$

$$s(v,\tau) = \int_{-\infty}^{\infty} h(t,\tau)\exp(-j2\pi vt)dt \tag{3.4}$$

The Doppler-variant impulse response $s(v,\tau)$ describes the spreading effect of the radio channel to the transmit signal in both the delay and Doppler domains.

Doppler-variant transfer function

Finally, applying the Fourier transform to the Doppler-variant impulse response $s(v,\tau)$ with respect to τ leads to the Doppler-variant transfer function

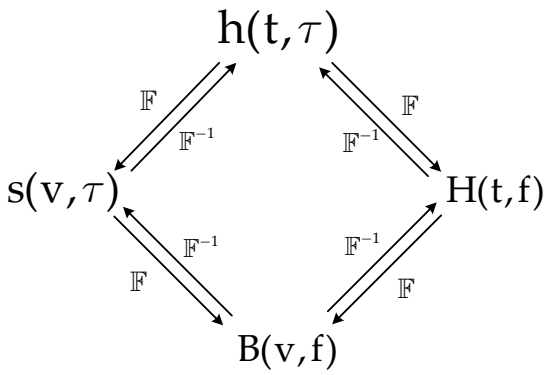

Figure 3.2: Interrelations among the four system functions for deterministic channels.

$B(v, f)$

$$B(v,f) = \int_{-\infty}^{\infty} s(v,\tau)\exp(-j2\pi f\tau)d\tau \tag{3.5}$$

The interrelations among the above four system functions are shown in Fig. 3.2, where the symbols $\mathbb{F}$ and $\mathbb{F}^{-1}$ denote the Fourier transform and the inverse Fourier transform, respectively.

3.2 Characterization of randomly time-variant linear channels

As mentioned previously, radio channels have the nature of randomness in reality. We thus interpret them as randomly time-variant linear systems [41]. A complete description of such radio channels requires a joint multidimensional PDF of all the system functions which is in practice too complicated to obtain. Hence, a less accurate but more realistic approach which is frequently used is based on a second-order description, i.e. the autocorrelation function of various system functions [23][37].

Here, we still use the $h(t,\tau)$, $H(t,f)$, $s(v,\tau)$ and $B(v,f)$ to represent the randomly time-variant impulse response, the randomly time-variant transfer function, the randomly Doppler-variant impulse response and the randomly Doppler-

variant transfer function, respectively, for notational simplicity. The autocorrelation functions of the four system functions for the randomly time-variant linear systems are defined as follows:

$$R_h(t,t',\tau,\tau') = E\left\{h^*(t,\tau)h(t',\tau')\right\} \tag{3.6}$$

$$R_H(t,t',f,f') = E\left\{H^*(t,f)H(t',f')\right\} \tag{3.7}$$

$$R_s(v,v',\tau,\tau') = E\left\{s^*(v,\tau)s(v',\tau')\right\} \tag{3.8}$$

$$R_B(v,v',f,f') = E\left\{B^*(v,f)B(v',f')\right\} \tag{3.9}$$

The autocorrelation functions depend on four variables, which are still rather complicated. Hence, the Wide-Sense Stationary Uncorrelated Scattering (WSSUS) assumption is usually made to further simplify the autocorrelation functions. Under the assumption of the WSSUS, the autocorrelation functions of the four system functions satisfy the following relationships:

$$R_h(t,t+\Delta t,\tau,\tau') = P_h(\Delta t,\tau)\delta(\tau-\tau') \tag{3.10}$$

$$R_H(t,t+\Delta t,f,f+\Delta f) = R_H(\Delta t,\Delta f) \tag{3.11}$$

$$R_s(v,v',\tau,\tau') = P_s(v,\tau)\delta(v-v')\delta(\tau-\tau') \tag{3.12}$$

$$R_B(v,v',f,f+\Delta f) = P_B(v,\Delta f)\delta(v-v') \tag{3.13}$$

Now the P-functions depend only on two variables, which greatly simplifies the analysis. The $P_h(\Delta t,\tau)$ is called the ***delay cross power spectral density***; The $R_H(\Delta t,\Delta f)$ is called the ***time frequency correlation function***; The $P_s(v,\tau)$ is called the ***scattering function*** and the $P_B(v,\Delta f)$ is called the ***Doppler cross power spectral density***. They are connected to each other by the Fourier transform. Their interrelations are shown in Fig. 3.3

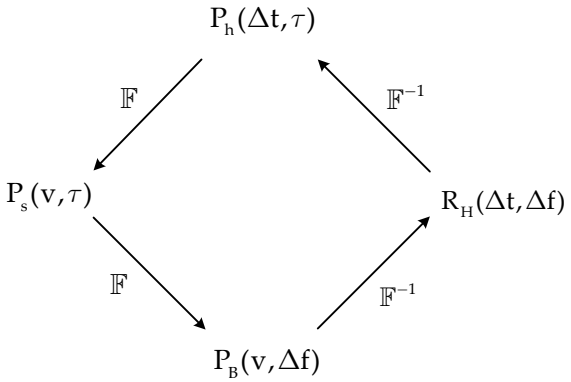

Figure 3.3: Interrelations among P-functions for WSSUS channels.

With the autocorrelation functions of the system functions in randomly time-variant linear channels, it is possible to obtain the autocorrelation function of the received signal $y(t)$ given the autocorrelation function of the transmit signal $x(t)$. In the following part, we will show how the autocorrelation function of the received signal are related to those of the system functions. Here, we just take the randomly time-variant impulse response $h(t,\tau)$ system function as an example. For other system functions, they can be derived in a similar way.

From Eq. 3.1, we know that the autocorrelation function of the received signal $y(t)$ can be expressed as $R_y(t,t')$

$$\begin{aligned} R_y(t,t') &= E\left\{y^*(t)y(t)\right\} \\ &= E\left\{\int_{-\infty}^{+\infty}\int_{-\infty}^{+\infty} x^*(t-\tau)x(t'-\tau')h^*(t-\tau)h(t'-\tau')d\tau d\tau'\right\} \\ &= \int_{-\infty}^{+\infty}\int_{-\infty}^{+\infty} x^*(t-\tau)x(t'-\tau')E\left\{h^*(t-\tau)h(t'-\tau')\right\}d\tau d\tau' \\ &= \int_{-\infty}^{+\infty}\int_{-\infty}^{+\infty} x^*(t-\tau)x(t'-\tau')R_h(t,t',\tau,\tau')d\tau d\tau' \end{aligned} \tag{3.14}$$

This shows that the autocorrelation function of the received signal can be determined by the autocorrelated functions of the system functions of radio channels. For WSSUS channels, we have $R_h(t,t',\tau,\tau') = P_h(\Delta t,\tau)\delta(\tau-\tau')$, where

$\Delta t = t' - t$. So Eq. 3.14 becomes

$$\begin{aligned} R_y(t, t+\Delta t) &= \int_{-\infty}^{+\infty} \int_{-\infty}^{+\infty} x^*(t-\tau)x(t+\Delta t-\tau')P_h(\Delta t, \tau)\delta(\tau-\tau')d\tau d\tau' \\ &= \int_{-\infty}^{+\infty} x^*(t-\tau)x(t+\Delta t-\tau)P_h(\Delta t, \tau)d\tau \end{aligned} \tag{3.15}$$

For the case $\Delta t = 0$, it becomes

$$R_y(t, t) = \int_{-\infty}^{+\infty} |x(t-\tau)|^2 P_h(\tau)d\tau \tag{3.16}$$

where $P_h(\tau) = P_h(0, \tau)$ is known as the ***Power Delay Profile*** (PDP). The Eq. 3.16 means that for WSSUS channels, the autocorrelation function of the received signal is determined by the Power Delay Profile $P_h(\tau)$ of the radio channels.

If ergodicity holds, the PDP can be obtained from the time-variant impulse response according to

$$P_h(\tau) = \lim_{T\to\infty} \frac{1}{2T} \int_{-T}^{T} |h(t, \tau)|^2 dt \tag{3.17}$$

3.3 Radio link quality parameters

This thesis focuses mainly on the indoor radio propagation, where the Doppler shift is negligible, so we are more interested in two of the autocorrelation functions of the system functions for randomly time-variant linear channels: the delay cross power spectral density $P_h(\Delta t, \tau)$ and the time frequency correlation function $R_H(\Delta t, \Delta f)$.

For the time frequency correlation function $R_H(\Delta t, \Delta f)$, when $\Delta t = 0$,

$$R_H(0, \Delta f) = R_H(\Delta f) \tag{3.18}$$

The $R_H(\Delta f)$ is called the ***Frequency Correlation Function*** (FCF). When $\Delta f = 0$,

$$R_H(\Delta t, 0) = R_H(\Delta t) \tag{3.19}$$

The $R_H(\Delta t)$ is called the ***Time Correlation Function*** (TCF). From Fig. 3.3, it is easy to know that the PDP $P_h(\tau)$ and the FCF $R_H(\Delta f)$ are a Fourier transform pair.

Two useful statistical parameters associated to $P_h(\tau)$ are the ***mean delay*** τ_m and the ***root mean square delay*** τ_{rms}:

$$\tau_m = \frac{\int_0^\infty \tau P_h(\tau) d\tau}{\int_0^\infty P_h(\tau) d\tau} \tag{3.20}$$

$$\tau_{rms} = \sqrt{\frac{\int_0^\infty (\tau - \tau_m)^2 P_h(\tau) d\tau}{\int_0^\infty P_h(\tau) d\tau}} \tag{3.21}$$

The root mean square delay τ_{rms} is of special importance because it has been shown that the error probability induced by the delay dispersion is proportional to the root mean square delay, but has no obvious relationships with the shape of the PDP [23]. This means it is not necessary to know about the actual shape of the PDP, but only the root mean square delay.

For the time frequency correlation function $R_H(\Delta t, \Delta f)$, there are also two statistical parameters associated to it: the ***coherence bandwidth*** B_c and the ***coherence time*** T_c. The coherence bandwidth B_c is the minimum value of Δf for which $R_H(\Delta f)$ equals some predefined values, e.g. 0.5 or 0.9. It is a parameter used to indicate how large the bandwidth is over which the signals are still strongly correlated. Similarly, the coherence time T_c is the minimum value of Δt for which $R_H(\Delta t)$ equals some predefined values. It is a measure of how long the time is over which the signals are still strongly correlated.

3.3.1 First-order fading statistics

In radio propagation channels, the received signal power fluctuates as a function of the time, space and frequency. To quantify the impacts of fading channels on the system performance, a wireless network designer must quantify first the distribution of the received signal power or voltage envelope.

Mean received signal power, SNR and SINR

Among all the first-order fading statistics, the ***mean received signal power*** is maybe the most common parameter since it is the most intuitive measure of the

radio link quality. According to the Shannon's Theorem, the achievable channel capacity C is a function of the available bandwidth B and the ***Signal-to-Noise Ratio*** (SNR) as follows

$$C = B \cdot \log_2(1 + S/N) \tag{3.22}$$

where S and N are the mean received signal power and the the mean noise power, respectively. The Ratio S/N is the SNR.

In AWGN channels, the SNR has an explicit relationship with the BER of radio channels. The bigger the SNR, the smaller the BER (i.e. the better the radio channels). In fading channels, since the instantaneous SNR is random, we use the ***mean SNR*** instead of the instantaneous SNR as a measure of the radio link quality. The mean SNR is computed as follows for fading channels

$$\bar{\gamma} = \int_0^\infty \gamma P_\gamma(\gamma) d\gamma \tag{3.23}$$

where γ and $\bar{\gamma}$ denotes the instantaneous SNR and the mean SNR, respectively, and $P_\gamma(\gamma)$ denotes the PDF of the instantaneous SNR.

For the radio communication scenario where multiple base stations or users exist, the received signal powers from any other irrelevant transmitters act like a kind of noise for a dedicated base station or user (called interference). Therefore, the concept of the ***Signal to Interference plus Noise Ratio*** (SINR) is introduced and it is defined as follows

$$SINR = \frac{S}{I + N} \tag{3.24}$$

where I denotes the power of the interference. From the definition above, it is known that the meaning of the SINR is the same as the SNR except that the SINR takes the interference into account as a kind of noise.

It is of importance to note that for those radio propagation models which provide a separate coverage map for each transmitter, the SINR is very easy to compute since the interference is just the sum of the received powers from other irrelevant transmitters.

Probability Density Function

Mean received power is just one aspect of the first-order behavior of radio channels [57]. In order to have a better understanding of the first-order behavior of radio channels, the received signal power or envelope ***Probability Density Function*** (PDF) is necessary.

Since power P is just the square of envelope α, the power PDF and the envelope PDF can be interconverted according to:

$$f_P(P) = \frac{1}{2\sqrt{P}} f_\alpha(\sqrt{P}) \tag{3.25}$$

$$f_\alpha(\alpha) = 2\alpha f_P(\alpha^2) \tag{3.26}$$

According to [57], the envelope PDF $f_\alpha(\alpha)$ and the characteristic function $\Phi_{XY}(v)$ are a Fourier-Bessel transform pair as follows:

$$f_\alpha(\alpha) = \alpha \int_0^\infty \Phi_{XY}(v) J_0(v\alpha) v dv \tag{3.27}$$

$$\Phi_{XY}(v) = \int_0^\infty f_\alpha(\alpha) J_0(v\alpha) d\alpha \tag{3.28}$$

Besides, the envelope PDF $f_\alpha(\alpha)$ has also a relationship with the well-known Moment Generating Function (MGF) $M_\gamma(s)$ which is defined by [25]

$$M_\gamma(s) = \int_0^\infty P_\gamma(\gamma) \cdot e^{s\gamma} d\gamma \tag{3.29}$$

Here let's take the Rayleigh fading as an example whose PDF is in Eq. 2.12. Typically, after attenuated by the fading channel, the signal will be also perturbed by Additive White Gaussian Noise (AWGN) which is normally independent of the fading amplitude [25]. If we assume that the energy per symbol of the transmitted signal is E_s and the one-sided power spectral density of AWGN is N_0, then the instantaneous SNR per symbol will be $\gamma = \alpha^2 E_s / N_0$.

The PDF of the instantaneous SNR per symbol can be obtained by introducing a change of variables in the fading envelope PDF α

$$\begin{aligned} P_\gamma(\gamma) &= P_\alpha(\sqrt{\frac{\Omega\gamma}{\bar{\gamma}}}) \Big/ 2\sqrt{\frac{\gamma\bar{\gamma}}{\Omega}} \\ &= \frac{1}{\bar{\gamma}} \exp(-\frac{\gamma}{\bar{\gamma}}), \quad \gamma \geq 0 \end{aligned} \tag{3.30}$$

where $\bar{\gamma} = \Omega E_s/N_0$ denotes the average SNR per symbol.

Combining the definition of the MGF in Eq. 3.29, we can then easily obtain the MGF of the Rayleigh fading

$$M_\gamma(s) = (1 - s\bar{\gamma})^{-1} \tag{3.31}$$

Similarly, we can obtain the MGF of the Rice fading and the Nakagami-m fading. The MGF of the Rice fading is

$$M_\gamma(s) = \frac{(1+n^2)}{(1+n^2) - s\bar{\gamma}} \exp(\frac{n^2 s\bar{\gamma}}{(1+n^2) - s\bar{\gamma}}) \tag{3.32}$$

If substituting the Rice K factor for the n^2 in Eq. 3.32, we can then obtain the MGF of the Rice fading as a function of the Rice K factor

$$M_\gamma(s) = \frac{(1+K)}{(1+K) - s\bar{\gamma}} \exp(\frac{Ks\bar{\gamma}}{(1+K) - s\bar{\gamma}}) \tag{3.33}$$

The MGF of the Nakagami-m fading is

$$M_\gamma(s) = \left(1 - \frac{s\bar{\gamma}}{m}\right)^{-m} \tag{3.34}$$

3.3.2 Second-order fading statistics

Although the first-order fading statistics are useful, they do not tell us how often the signal falls below a threshold and how long the signal stays below this threshold. Such kind of fading statistics are important for the performance of error-correction coding and spatial diversity etc.

Outage probability

The outage probability is defined as the probability that the instantaneous BER exceeds a threshold or equivalently the instantaneous SNR falls below a corresponding threshold [25]

$$P_{outage} = \int_0^{\gamma_{th}} P_\gamma(\gamma) d\gamma \tag{3.35}$$

where $P_\gamma(\gamma)$ is the PDF of the SNR and γ_{th} is the corresponding threshold of the SNR.

An interesting property of the P_{outage} is that the P_{outage} is related to the MGF of the SNR as follows [25]

$$P_{outage} = \frac{1}{2\pi j} \int_{\sigma-j\infty}^{\sigma+j\infty} \frac{M_{\gamma}(-s)}{s} e^{s\gamma_{th}} ds \tag{3.36}$$

This relationship to the MGF can be easily derived according the definition of the MGF in Eq. 3.29. This relationship is very useful to compute the P_{outage} in practice since the MGF of many fading models are already available.

Level-crossing rate

The level-crossing rate $N(\gamma_{th})$ is defined as the average number of crossings per second that the signal falls below a threshold

$$N(\gamma_{th}) = \int_{0}^{\infty} \gamma' f_{\gamma,\gamma'}(\gamma_{th}, \gamma') d\gamma' \tag{3.37}$$

where $f_{\gamma,\gamma'}(\gamma_{th}, \gamma')$ is the joint PDF of γ and its time derivative γ'.

Average fade duration

The average fade duration is the amount of time that the signal stays below a threshold once it has crossed that threshold. The average fade duration $T(\gamma_{th})$ can be calculated as the ratio of the outage probability to the level-crossing rate:

$$T(\gamma_{th}) = \frac{P_{outage}}{N(\gamma_{th})} \tag{3.38}$$

3.3.3 Bit error rate and bit error probability

The Bit Error Rate (BER) is a key parameter for measuring the quality of radio links. It is defined as the ratio of the number of error bits to the total number of transferred bits

$$BER = \frac{N_{error}}{N_{total}} \tag{3.39}$$

where N_{error} and N_{total} are the number of error bits and the number of transferred bits, respectively. The BER provides an end-to-end measure of radio links. Unlike other parameters stated above which reflects radio link quality indirectly, the BER measures the link quality directly, i.e. the SNR, the average fade duration etc

reflect the radio link quality through their impacts on the BER. Hence, the BER is the fundamental parameter for radio link quality and it has been widely used.

Another relevant parameter is the Bit Error Probability (BEP). The BER can be considered as the estimate of the BEP. The larger the total number of the transferred bits is, the more accurate the estimate becomes.

3.3.4 Throughput

The throughput is a higher layer concept to measure the link quality. The throughput is defined as the sum of data rates delivered to all terminals in a network

$$Throughput = \sum_{i=1}^{N} R_i \tag{3.40}$$

where R_i is the data rate for the i-th terminal and N is the total number of terminals in the network. The throughput is usually measured in bits per second, i.e. bps. High throughput is the basis for a system to provide all kinds of high quality services.

3.4 Chapter summary

This chapter was dedicated to the radio link quality evaluation. We started with the characterization of deterministic channels whose behavior can be determined by any one of their four system functions. However, a realistic radio channel is a kind of random process whose characteristics can not be completely determined in a deterministic manner. The better way is to describe them statistically. Thus, the autocorrelation functions of the four system functions are introduced and they are widely used in describing the behavior of randomly time-variant linear channels. The last part of this chapter listed a number of fading parameters which will be used in the latter chapters to evaluate the radio link quality.

Chapter 4

Extraction of fading statistics based on the MR-FDPF model

As stated in Chapter 2, the MR-FDPF model falls into the category of deterministic models. Deterministic models can usually provide an accurate radio coverage prediction. In reality, radio channels have the nature of randomness due to e.g. moving people or objects. Thus, they can not be rigorously simulated by a purely deterministic model. However, it is believed that some fading statistics can be extracted from deterministic models and these statistics can be used to describe radio channels in reality.

In this chapter, the large scale and small scale fading statistics are extracted based on the MR-FDPF model after a detailed introduction of the MR-FDPF model in Section 4.1. The extraction performance is verified by comparisons with measurements. These extracted large scale and small scale fading statistics can be very useful for system level simulators. At the end of this chapter, a semi-deterministic model is proposed based on the the extracted large scale propagation characteristic and the small scale fading statistics. The proposed semi-deterministic model is based on the deterministic MR-FDPF model but introduces a stochastic part to take into account the random aspect of the realistic channels.

4.1 The MR-FDPF model

This section gives a more detailed description of the MR-FDPF model which has been briefly introduced in Chapter 2.

4.1.1 The FDPF model

We start with the Frequency-Domain ParFlow model (FDPF) model. When applying the Fourier transform on both sides of the local scattering equation (Eq. 2.20) in the ParFlow model, we obtain the local scattering equation for the FDPF model as follows

$$\vec{F}(r,v) = \Sigma_f(r,v) \cdot \overleftarrow{F}(r,v) + \vec{S}(r,v) \tag{4.1}$$

where $\Sigma_f(r,v) = \Sigma_a(r) \cdot e^{-j2\pi v dt}$. Now we show how the inner flow can be removed from the FDPF model and only the border flows, i.e. the inward flows and outward flows are enough for the electric field prediction. Let's define the border outward flow vector, the border inward flow vector and the inner flow vector in the frequency domain as follows:

$$\vec{F}_b(r) = \begin{pmatrix} \vec{f}_E(r) \\ \vec{f}_W(r) \\ \vec{f}_S(r) \\ \vec{f}_N(r) \end{pmatrix} \quad ; \quad \overleftarrow{F}_b(r) = \begin{pmatrix} \overleftarrow{f}_E(r) \\ \overleftarrow{f}_W(r) \\ \overleftarrow{f}_S(r) \\ \overleftarrow{f}_N(r) \end{pmatrix} \tag{4.2}$$

$$\breve{F}(r) = \left(\breve{f}_0(r)\right) \tag{4.3}$$

If the $\Sigma_f(r,v)$ in Eq. 4.1 is written in the form of

$$\Sigma_f(r,v) = \begin{pmatrix} \Sigma_{ee}(r) & \Sigma_{ei}(r) \\ \Sigma_{ie}(r) & \Sigma_{ii}(r) \end{pmatrix} \tag{4.4}$$

then according to Eq. 2.22, it is easy to obtain that

$$\Sigma_{ee}(r) = \sigma_0 \cdot \begin{pmatrix} 1 & \alpha_r & 1 & 1 \\ \alpha_r & 1 & 1 & 1 \\ 1 & 1 & 1 & \alpha_r \\ 1 & 1 & \alpha_r & 1 \end{pmatrix} \qquad \Sigma_{ei}(r) = \sigma_0 \cdot \begin{pmatrix} Y_r \\ Y_r \\ Y_r \\ Y_r \end{pmatrix}$$
$$\Sigma_{ie}(r) = \sigma_0 \cdot \begin{pmatrix} 1 & 1 & 1 & 1 \end{pmatrix} \qquad \Sigma_{ii}(r) = \sigma_0 \cdot \beta_r \tag{4.5}$$

where $\sigma_0 = \frac{a_r}{2{n_r}^2} e^{-j2\pi vdt}$. The border flow vector of a source is

$$\vec{S}_b(r) = \begin{pmatrix} \vec{s}_E(r) \\ \vec{s}_W(r) \\ \vec{s}_S(r) \\ \vec{s}_N(r) \end{pmatrix} \tag{4.6}$$

For a real source node, i.e. not an equivalent source node discussed later, the $\breve{s}_0(r) = 0$ since it has no inner flow. Now the local scattering equation (Eq. 4.1) can be expressed as

$$\begin{pmatrix} \vec{F}_b(r) \\ \breve{f}_o(r) \end{pmatrix} = \begin{pmatrix} \Sigma_{ee}(r) & \Sigma_{ei}(r) \\ \Sigma_{ie}(r) & \Sigma_{ii}(r) \end{pmatrix} \cdot \begin{pmatrix} \overleftarrow{F}_b(r) \\ \breve{f}_o(r) \end{pmatrix} + \begin{pmatrix} \vec{S}_b(r) \\ 0 \end{pmatrix} \tag{4.7}$$

Solving this equation with respect to $\breve{f}_o(r)$, we obtain

$$\breve{f}_o(r) = (I - \Sigma_{ii}(r))^{-1} \cdot \left(\Sigma_{ie}(r) \cdot \overleftarrow{F}_b(r)\right) \tag{4.8}$$

$$\vec{F}_b(r) = \Sigma_b(r) \cdot \overleftarrow{F}_b(r) + \vec{S}_b(r) \tag{4.9}$$

where

$$\Sigma_b(r) = \Sigma_{ee}(r) + \Sigma_{ei}(r) \cdot (I - \Sigma_{ii}(r))^{-1} \cdot \Sigma_{ie}(r) \tag{4.10}$$

After substituting the $\Sigma_{ee}(r)$, $\Sigma_{ei}(r)$, $\Sigma_{ie}(r)$ and $\Sigma_{ii}(r)$ with their corresponding matrix in Eq. 4.5, the $\Sigma_b(r)$ can be expressed as follows

$$\Sigma_b(r) = \sigma_0 \cdot \begin{pmatrix} \sigma_1 & \sigma_2 & \sigma_1 & \sigma_1 \\ \sigma_2 & \sigma_1 & \sigma_1 & \sigma_1 \\ \sigma_1 & \sigma_1 & \sigma_1 & \sigma_2 \\ \sigma_1 & \sigma_1 & \sigma_2 & \sigma_1 \end{pmatrix} \tag{4.11}$$

where $\sigma_1 = 1 + Y_r \cdot k_r$, $\sigma_2 = \alpha_r + Y_r \cdot k_r$ and $k_r = \frac{\sigma_0}{1 - \sigma_0 \cdot \beta_r}$.

Finally, the electric field can be computed only with the inward flows as follows

$$\Psi(r, v) = \frac{1 + Y_r \cdot k_r}{{n_r}^2} \cdot \sum_{d=E,W,S,N} \overleftarrow{f}_d(r, v) \tag{4.12}$$

4.1.2 The MR approach

The Eq. 4.9 is the local scattering equation for the FDPF model which contains only the border flows. When written in the global form, the local scattering matrix will be huge even if the inner flow has already been removed. Thus the direct matrix inversion is still unbearable for most of scenarios.

In [6][58], Gorce et al. proposed a Multi-Resolution (MR) decomposition of this problem which avoids the direct matrix inversion. It is based on the binary tree decomposition of the simulated scenarios and the concept of the MR nodes. This approach is thus called the MR approach.

The binary tree decomposition of the simulated scenarios is conducted as follows: First, the simulated scenario, i.e. the head node, is divided into two child nodes along its main discontinuity line. Second, each of the two child nodes is further divided into another two child nodes, and so on as shown in Fig. 4.1. Finally, the division is terminated when the smallest predefined nodes are reached, e.g. the usual ParFlow pixels or the homogeneous nodes.

All the nodes in the binary tree of the simulated scenarios are called the MR nodes. One MR node is a rectangular aggregate of usual ParFlow pixels whose sides are associated with inward or outward flows as shown in Fig. 4.2. The property of the MR nodes is exactly the same as usual ParFlow pixels except that the MR nodes usually contain a set of ParFlow pixels. For instance, the outward flows and inward flows associated to the MR nodes are also bound by the local scattering equation. The MR node which is immediately on the top of another two smaller nodes is called the father node of the two smaller nodes. Meanwhile, the two smaller nodes are called the child nodes of their top father node. From the binary tree, it is obvious that except the head node and the pixel nodes, all the father nodes can be the child nodes of their top father nodes and all the child nodes can be also the father nodes of their underneath child nodes. For the head node, it only has the child nodes. For the pixel nodes, they only have the father nodes.

In the following, we explain that the local scattering matrix of a father node can be derived from those of its two child nodes. The derivation depends on the direction of gathering of the child nodes, i.e., the horizontal gathering or the

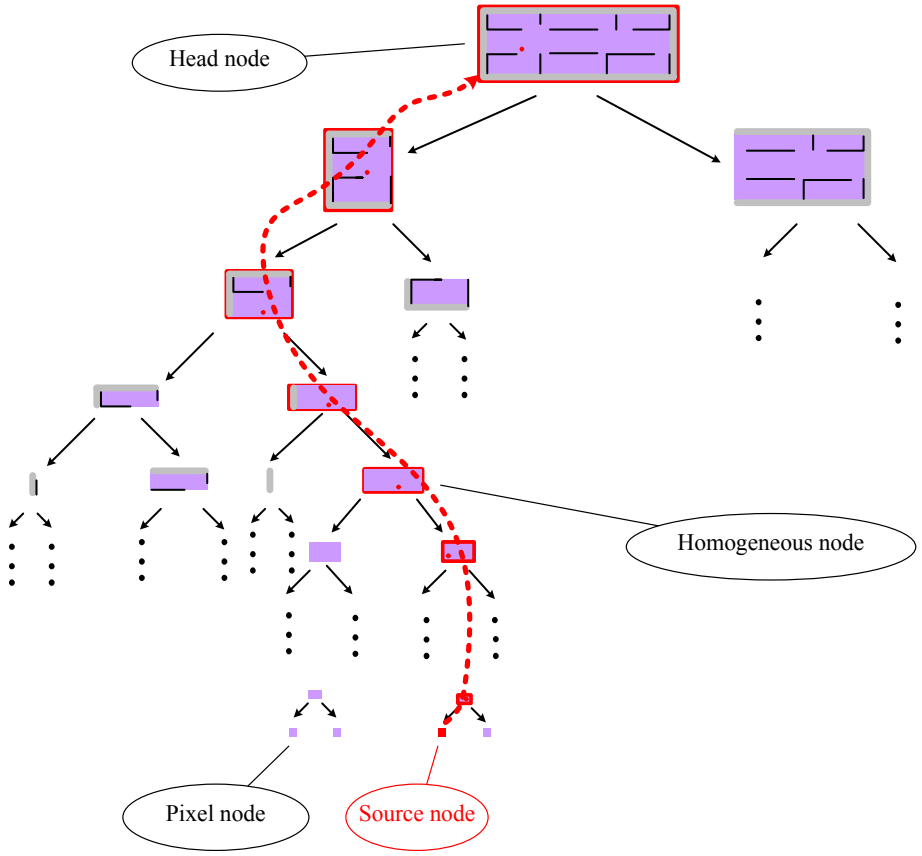

Figure 4.1: The binary tree of the simulated scenario and the MR nodes

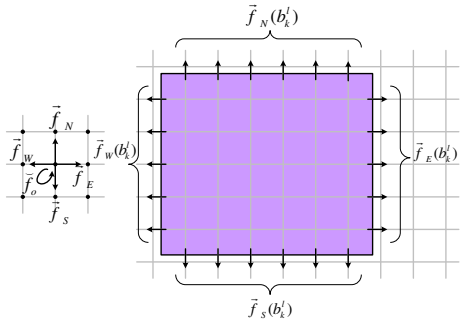

Figure 4.2: The usual ParFlow pixel and the MR node

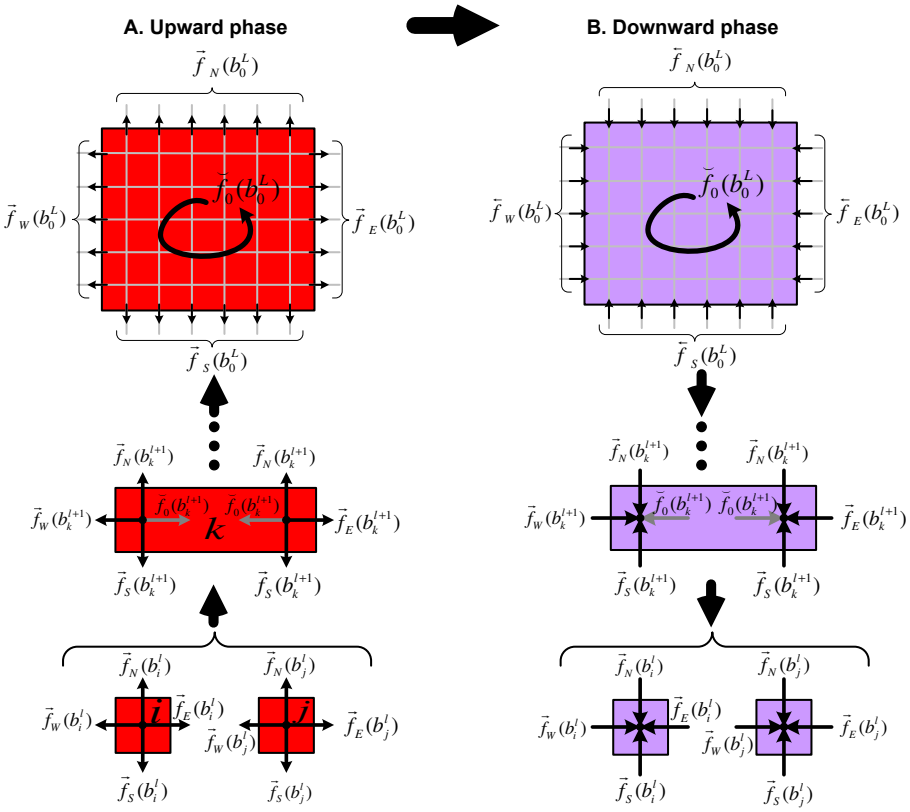

Figure 4.3: The upward and downward phase

vertical gathering. Here, we take the horizontal gathering as an illustration, but the vertical gathering can be derived in the similar way.

Assume that the child nodes i and j are at level l in the binary tree (see Fig. 4.3) with the border outward flow vector $\vec{F}_b(b_i^l)$ and $\vec{F}_b(b_j^l)$ respectively as follows

$$\vec{F}_b(b_i^l) = \begin{pmatrix} \vec{f}_E(b_i^l) \\ \vec{f}_W(b_i^l) \\ \vec{f}_S(b_i^l) \\ \vec{f}_N(b_i^l) \end{pmatrix} \quad ; \quad \vec{F}_b(b_j^l) = \begin{pmatrix} \vec{f}_E(b_j^l) \\ \vec{f}_W(b_j^l) \\ \vec{f}_S(b_j^l) \\ \vec{f}_N(b_j^l) \end{pmatrix} \tag{4.13}$$

From the previous knowledge (e.g. Eq. 4.9), we know that the border outward flow vector can be obtained from the border inward flow vector through the local scattering equation involving only the border flows. Thus, for the child node i,

we have

$$\vec{F}_b(b_i^l) = \Sigma_b(b_i^l) \cdot \overleftarrow{F}_b(b_i^l) + \vec{S}_b(b_i^l) \tag{4.14}$$

where

$$\Sigma_b(b_i^l) = \Sigma_{ee}(b_i^l) + \Sigma_{ei}(b_i^l) \cdot (I - \Sigma_{ii}(b_i^l))^{-1} \cdot \Sigma_{ie}(b_i^l) \tag{4.15}$$

Whatever, we can write the $\Sigma_b(b_i^l)$ into the following form

$$\Sigma_b(b_i^l) = \begin{pmatrix} \sigma^b_{EE}(b_i^l) & \sigma^b_{EW}(b_i^l) & \sigma^b_{ES}(b_i^l) & \sigma^b_{EN}(b_i^l) \\ \sigma^b_{WE}(b_i^l) & \sigma^b_{WW}(b_i^l) & \sigma^b_{WS}(b_i^l) & \sigma^b_{WN}(b_i^l) \\ \sigma^b_{SE}(b_i^l) & \sigma^b_{SW}(b_i^l) & \sigma^b_{SS}(b_i^l) & \sigma^b_{SN}(b_i^l) \\ \sigma^b_{NE}(b_i^l) & \sigma^b_{NW}(b_i^l) & \sigma^b_{NS}(b_i^l) & \sigma^b_{NN}(b_i^l) \end{pmatrix} \tag{4.16}$$

where $\sigma^b_{WE}(b_i^l)$ for example means the coefficient for the east inward flow propagating to the west outward flow. For the child node j, we have the same results by just replacing the subscript i with j.

Now, we move to the father node k at the top level $l+1$. From Fig. 4.3, it is straightforward that

$$\begin{aligned} \vec{f}_E(b_k^{l+1}) &= \vec{f}_E(b_j^l); & \vec{f}_W(b_k^{l+1}) &= \vec{f}_W(b_i^l) \\ \vec{f}_S(b_k^{l+1}) &= \begin{pmatrix} \vec{f}_S(b_i^l) \\ \vec{f}_S(b_j^l) \end{pmatrix}; & \vec{f}_N(b_k^{l+1}) &= \begin{pmatrix} \vec{f}_N(b_i^l) \\ \vec{f}_N(b_j^l) \end{pmatrix} \end{aligned} \tag{4.17}$$

$$\begin{aligned} \overleftarrow{f}_E(b_k^{l+1}) &= \overleftarrow{f}_E(b_i^l); & \overleftarrow{f}_W(b_k^{l+1}) &= \overleftarrow{f}_W(b_j^l) \\ \overleftarrow{f}_S(b_k^{l+1}) &= \begin{pmatrix} \overleftarrow{f}_S(b_i^l) \\ \overleftarrow{f}_S(b_j^l) \end{pmatrix}; & \overleftarrow{f}_N(b_k^{l+1}) &= \begin{pmatrix} \overleftarrow{f}_N(b_i^l) \\ \overleftarrow{f}_N(b_j^l) \end{pmatrix} \end{aligned} \tag{4.18}$$

$$\breve{f}_0(b_k^{l+1}) = \begin{pmatrix} \overleftarrow{f}_W(b_i^l) \\ \overleftarrow{f}_E(b_j^l) \end{pmatrix} = \begin{pmatrix} \vec{f}_W(b_j^l) \\ \vec{f}_E(b_i^l) \end{pmatrix} \tag{4.19}$$

Then, the outward flow vector and inward flow vector of the father node k can be expanded as

$$\vec{F}(b_k^{l+1}) = \begin{pmatrix} \vec{f}_E(b_k^{l+1}) \\ \vec{f}_W(b_k^{l+1}) \\ \vec{f}_S(b_k^{l+1}) \\ \vec{f}_N(b_k^{l+1}) \\ \breve{f}_0(b_k^{l+1}) \end{pmatrix} = \begin{pmatrix} \vec{f}_E(b_j^l) \\ \vec{f}_W(b_i^l) \\ \vec{f}_S(b_i^l) \\ \vec{f}_S(b_j^l) \\ \vec{f}_N(b_i^l) \\ \vec{f}_N(b_j^l) \\ \vec{f}_W(b_j^l) \\ \vec{f}_E(b_i^l) \end{pmatrix} \tag{4.20}$$

$$\overleftarrow{F}(b_k^{l+1}) = \begin{pmatrix} \overleftarrow{f}_E(b_k^{l+1}) \\ \overleftarrow{f}_W(b_k^{l+1}) \\ \overleftarrow{f}_S(b_k^{l+1}) \\ \overleftarrow{f}_N(b_k^{l+1}) \\ \overleftarrow{f}_0(b_k^{l+1}) \end{pmatrix} = \begin{pmatrix} \overleftarrow{f}_E(b_i^l) \\ \overleftarrow{f}_W(b_j^l) \\ \overleftarrow{f}_S(b_i^l) \\ \overleftarrow{f}_S(b_j^l) \\ \overleftarrow{f}_N(b_i^l) \\ \overleftarrow{f}_N(b_j^l) \\ \overleftarrow{f}_W(b_i^l) \\ \overleftarrow{f}_E(b_j^l) \end{pmatrix} \tag{4.21}$$

Therefore, the local scattering matrix of the father node k is

$$\Sigma_f(b_k^{l+1}) = \begin{pmatrix} [0] & \sigma^b_{EW}(b_j^l) & [0] & \sigma^b_{ES}(b_j^l) & [0] & \sigma^b_{EN}(b_j^l) & [0] & \sigma^b_{EE}(b_j^l) \\ \sigma^b_{WE}(b_i^l) & [0] & \sigma^b_{WS}(b_i^l) & [0] & \sigma^b_{WN}(b_i^l) & [0] & \sigma^b_{WW}(b_i^l) & [0] \\ \sigma^b_{SE}(b_i^l) & [0] & \sigma^b_{SS}(b_i^l) & [0] & \sigma^b_{SN}(b_i^l) & [0] & \sigma^b_{SW}(b_i^l) & [0] \\ [0] & \sigma^b_{SW}(b_j^l) & [0] & \sigma^b_{SS}(b_j^l) & [0] & \sigma^b_{SN}(b_j^l) & [0] & \sigma^b_{SE}(b_j^l) \\ \sigma^b_{NE}(b_i^l) & [0] & \sigma^b_{NS}(b_i^l) & [0] & \sigma^b_{NN}(b_i^l) & [0] & \sigma^b_{NW}(b_i^l) & [0] \\ [0] & \sigma^b_{NW}(b_j^l) & [0] & \sigma^b_{NS}(b_j^l) & [0] & \sigma^b_{NN}(b_j^l) & [0] & \sigma^b_{NE}(b_j^l) \\ [0] & \sigma^b_{WW}(b_j^l) & [0] & \sigma^b_{WS}(b_j^l) & [0] & \sigma^b_{WN}(b_j^l) & [0] & \sigma^b_{WE}(b_j^l) \\ \sigma^b_{EE}(b_i^l) & [0] & \sigma^b_{ES}(b_i^l) & [0] & \sigma^b_{EN}(b_i^l) & [0] & \sigma^b_{EW}(b_i^l) & [0] \end{pmatrix} \tag{4.22}$$

which is totally determined by the local scattering matrices of its child nodes i and j. Then

$$\Sigma_{ee}(b_k^{l+1}) = \begin{pmatrix} [0] & \sigma^b_{EW}(b_j^l) & [0] & \sigma^b_{ES}(b_j^l) & [0] & \sigma^b_{EN}(b_j^l) \\ \sigma^b_{WE}(b_i^l) & [0] & \sigma^b_{WS}(b_i^l) & [0] & \sigma^b_{WN}(b_i^l) & [0] \\ \sigma^b_{SE}(b_i^l) & [0] & \sigma^b_{SS}(b_i^l) & [0] & \sigma^b_{SN}(b_i^l) & [0] \\ [0] & \sigma^b_{SW}(b_j^l) & [0] & \sigma^b_{SS}(b_j^l) & [0] & \sigma^b_{SN}(b_j^l) \\ \sigma^b_{NE}(b_i^l) & [0] & \sigma^b_{NS}(b_i^l) & [0] & \sigma^b_{NN}(b_i^l) & [0] \\ [0] & \sigma^b_{NW}(b_j^l) & [0] & \sigma^b_{NS}(b_j^l) & [0] & \sigma^b_{NN}(b_j^l) \end{pmatrix} \tag{4.23}$$

$$\Sigma_{ei}(b_k^{l+1}) = \begin{pmatrix} [0] & \sigma^b_{EE}(b_j^l) \\ \sigma^b_{WW}(b_i^l) & [0] \\ \sigma^b_{SW}(b_i^l) & [0] \\ [0] & \sigma^b_{SE}(b_j^l) \\ \sigma^b_{NW}(b_i^l) & [0] \\ [0] & \sigma^b_{NE}(b_j^l) \end{pmatrix} \tag{4.24}$$

$$\Sigma_{ie}(b_k^{l+1}) = \begin{pmatrix} [0] & \sigma^b_{WW}(b_j^l) & [0] & \sigma^b_{WS}(b_j^l) & [0] & \sigma^b_{WN}(b_j^l) \\ \sigma^b_{EE}(b_i^l) & [0] & \sigma^b_{ES}(b_i^l) & [0] & \sigma^b_{EN}(b_i^l) & [0] \end{pmatrix} \tag{4.25}$$

$$\Sigma_{ii}(b_k^{l+1}) = \begin{pmatrix} [0] & \sigma^b_{WE}(b_j^l) \\ \sigma^b_{EW}(b_i^l) & [0] \end{pmatrix} \tag{4.26}$$

Since there is a relationship between the local scattering matrix of the father node and those of its two child nodes, this relationship can be used to facilitate us in solving the electric field prediction problem. Actually this is what the MR approach does. The MR approach aims at solving the problem in two steps. The first step is to compute the equivalent source of the father nodes which contain a real or an equivalent child source node in the binary tree, e.g. along the red dashed line in Fig. 4.1. This process starts from the pixel level and ends at the head node level. The equivalent source is computed by setting the inward flows to 0. The second step is to propagate the equivalent source obtained in the first step to the pixel level. This step starts from the head node level with the initial inward flows $\overleftarrow{F}_b(b_0^L)$ set to 0 according to the boundary conditions.

This is clear if we analyze the local scattering equation as follows

$$\begin{pmatrix} \vec{F}_b(b_k^{l+1}) \\ \breve{F}_0(b_k^{l+1}) \end{pmatrix} = \begin{pmatrix} \Sigma_{ee}(b_k^{l+1}) & \Sigma_{ei}(b_k^{l+1}) \\ \Sigma_{ie}(b_k^{l+1}) & \Sigma_{ii}(b_k^{l+1}) \end{pmatrix} \cdot \begin{pmatrix} \overleftarrow{F}_b(b_k^{l+1}) \\ \breve{F}_0(b_k^{l+1}) \end{pmatrix} + \begin{pmatrix} \vec{S}_b(b_k^{l+1}) \\ \breve{S}_0(b_k^{l+1}) \end{pmatrix} \tag{4.27}$$

Solving this equation with respect to the $\breve{F}_0(b_k^{l+1})$ leads to

$$\breve{F}_0(b_k^{l+1}) = (I - \Sigma_{ii}(b_k^{l+1}))^{-1} \cdot \Sigma_{ie}(b_k^{l+1}) \cdot \overleftarrow{F}_b(b_k^{l+1}) + (I - \Sigma_{ii}(b_k^{l+1}))^{-1} \cdot \breve{S}_0(b_k^{l+1}) \tag{4.28}$$

And the local scattering equation involving only the border flows is obtained

$$\vec{F}_b(b_k^{l+1}) = \Sigma_b(b_k^{l+1}) \cdot \overleftarrow{F}_b(b_k^{l+1}) + \vec{S}_{eq}(b_k^{l+1}) \tag{4.29}$$

where

$$\Sigma_b(b_k^{l+1}) = \Sigma_{ei}(b_k^{l+1}) \cdot (I - \Sigma_{ii}(b_k^{l+1}))^{-1} \cdot \Sigma_{ie}(b_k^{l+1}) + \Sigma_{ee}(b_k^{l+1}) \tag{4.30}$$

$$\vec{S}_{eq}(b_k^{l+1}) = \vec{S}_b(b_k^{l+1}) + \Sigma_{ei}(b_k^{l+1}) \cdot (I - \Sigma_{ii}(b_k^{l+1}))^{-1} \cdot \breve{S}_0(b_k^{l+1}) \tag{4.31}$$

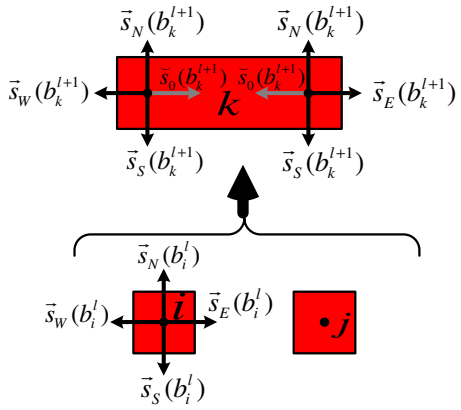

Figure 4.4: Computation of the equivalent source of the father node

To transform a father node into a source node, the outward flows of the father node $\vec{F}_b(b_k^{l+1})$ should be determined. The outward flows are only driven by the child source flows, i.e. the inward flows $\overleftarrow{F}_b(b_k^{l+1}) = 0$. Thus, according to Eq. 4.29,

$$\vec{F}_b(b_k^{l+1}) = \vec{S}_{eq}(b_k^{l+1}) \tag{4.32}$$

$$= \vec{S}_b(b_k^{l+1}) + \Sigma_{ei}(b_k^{l+1}) \cdot (I - \Sigma_{ii}(b_k^{l+1}))^{-1} \cdot \breve{S}_0(b_k^{l+1}) \tag{4.33}$$

where $\breve{S}_0(b_k^{l+1})$ and $\vec{S}_b(b_k^{l+1})$ depend on which child node is the source and the direction of gathering. For instance, for an horizontal gathering and the case that the left child i is the source as show in Fig. 4.4:

$$\breve{S}_0(b_k^{l+1}) = \begin{pmatrix} 0 \\ \vec{s}_E(b_i^l) \end{pmatrix} \tag{4.34}$$

and

$$\vec{S}_b(b_k^{l+1}) = \begin{pmatrix} \vec{s}_E(b_k^{l+1}) \\ \vec{s}_W(b_k^{l+1}) \\ \vec{s}_S(b_k^{l+1}) \\ \vec{s}_N(b_k^{l+1}) \end{pmatrix} = \begin{pmatrix} 0 \\ \vec{s}_W(b_i^l) \\ \vec{s}_S(b_i^l) \\ 0 \\ \vec{s}_N(b_i^l) \\ 0 \end{pmatrix} \tag{4.35}$$

After obtaining the equivalent source of the head node in the first step, the second step must propagate the equivalent source to the pixel level, i.e. computes the inward flows of the child nodes from the head node (see Fig. 4.5). According

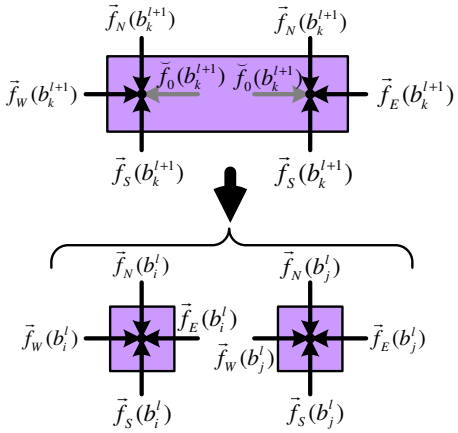

Figure 4.5: Computation of the inward flows of the child nodes

to Eq. 4.21, it is known that the inward flows of the child nodes can be obtained if we have known the inward flows and the inner flow of the father nodes. For the inward flows, they are started by setting to 0 for the head node because no energy is supposed to come from the outside according to the boundary conditions. For the inner flow, it can be computed according to Eq. 4.28.

4.1.3 The MR-FDPF model

According to the description of the MR approach above, the final implementation of the MR-FDPF model can be divided into the following four steps:

1. ***Discretize the simulated scenario and construct the binary tree***.

2. ***Preprocessing phase***: In this phase, three matrices associated with each MR nodes are computed and stored because the computation of them does not require any information of the sources. The tree matrices are the upward matrix, the downward matrix and the inner matrix:

$$U(b_k^{l+1}) = \Sigma_{ei}(b_k^{l+1}) \tag{4.36}$$

$$D(b_k^{l+1}) = \Sigma_{ie}(b_k^{l+1}) \tag{4.37}$$

$$I(b_k^{l+1}) = (I - \Sigma_{ii}(b_k^{l+1}))^{-1} \tag{4.38}$$

These matrices will be used in the upward and downward phases.

3. ***The upward phase***: The upward phase is only executed along the source MR nodes, i.e. along the red dashed line in Fig. 4.1 from the pixel level to the head node level. First, the upward phase computes and stores the steady-state inner flows (driven by the source) according to

$$\breve{F}_0^S(b_k^{l+1}) = I(b_k^{l+1}) \cdot \breve{S}_0(b_k^{l+1}) \tag{4.39}$$

which will be used in the downward phase to compute the inner flow of the father nodes. Second, the upward phase computes the equivalent source of the father MR nodes according to

$$\vec{S}_{eq}(b_k^{l+1}) = \vec{S}_b(b_k^{l+1}) + U(b_k^{l+1}) \cdot \breve{F}_0^S(b_k^{l+1}) \tag{4.40}$$

4. ***The downward phase***: Unlike the upward phase which is only executed along the source MR nodes, the downward phase should be executed along all the branches in the binary tree. The downward phase mainly computes the inner flows of the father nodes and thus the inward flows of the child nodes can be easily obtained. The inner flows of the father nodes can be computed according to Eq. 4.28. More specifically, for the MR nodes which are not the equivalent source nodes, it is

$$\breve{F}_0(b_k^{l+1}) = I(b_k^{l+1}) \cdot D(b_k^{l+1}) \cdot \overleftarrow{F}_b(b_k^{l+1}) \tag{4.41}$$

For the MR nodes which are the equivalent source nodes, it is

$$\breve{F}_0(b_k^{l+1}) = I(b_k^{l+1}) \cdot D(b_k^{l+1}) \cdot \overleftarrow{F}_b(b_k^{l+1}) + \breve{F}_0^S(b_k^{l+1}) \tag{4.42}$$

For the inward flows, it is initiated with $\overleftarrow{F}_b(b_0^L) = 0$ for the head node. Then the inward flows of the child nodes can be obtained iteratively until the pixel level is reached. At the end of the iterations, the frequency domain ParFlow linear system is solved exactly, with no approximations.

4.1.4 Calibration

A calibration process is usually considered to be imperative for any radio wave propagation model since the properties of materials in the simulated scenarios are never exactly known. According to Eq. 4.1 and Eq. 4.5, we know that in the simulated scenarios, the effect of objects to the electromagnetic waves depends on two parameters: the refraction index n_r and the normalized absorption coefficient a_r. Hence, the two parameters of the objects in the simulated scenarios need to be calibrated in the calibration process. It is noted that the absorption coefficient of the air a_{air} is also relaxed in the calibration process. It is based on the fact that for a pure $2D$ model, its free space path loss is proportional to the Tx-Rx separation distance d, i.e., $PL(d) \propto d$. However, for a realistic $3D$ propagation, its free space path loss is: $PL(d) \propto d^2$. Therefore, an attenuation coefficient a_{air} is introduced in the local scattering matrix for the air-filled pixels, modifying the path loss model to

$$PL(d) \propto d \cdot a_{air}^{-d/\Delta r} \tag{4.43}$$

where Δr is the discretization space step. This modified path loss model can fit the realistic 3D propagation model over a finite range after an appropriate choice of the a_{air} [8].

The calibration process is done in two steps. The first step is to estimate the constant offset as follows

$$\Delta\Psi = \frac{1}{m}\sum_{k=0}^{m}\left(\Psi_{mes}\left(k\right) - \Psi_{sim}\left(k\right)\right) \tag{4.44}$$

where $\Psi_{mes}\left(k\right)$ and $\Psi_{sim}\left(k\right)$ are the mean powers from measurements and simulations, respectively, and m is the total number of samples. A constant offset always exists because of the numerical sources used in the MR-FDPF model, compared to the real transmitters in reality. The second step of the calibration process is to estimate the a_{air} and (n_{mat}, a_{mat}) by minimizing the cost-function Q defined by the root mean square error (RMSE) between measurements and predictions

$$Q = RMSE = \sqrt{\frac{1}{m}\sum_{k=0}^{m}\left\|\Psi_{mes}\left(k\right) - \Psi_{pred}\left(k\right)\right\|^2} \tag{4.45}$$

where

$$\Psi_{pred}(k) = \Psi_{sim}(k) + \Delta\Psi \tag{4.46}$$

are the mean powers from predictions. The minimization process is solved by the direct search algorithm "DIRECT" by Jones et Al. in [59]. A more detailed description about the calibration process of the MR-FDPF model can be found in [60].

It is noted that it is not neccessary to perform the calibration process with too many measurement points. Usually, only a few measurement points, e.g. a subset of all the measurement points, already allow obtaining a relatively good prediction results, e.g. the RMSE less than or around 8 dB.

4.1.5 Accuracy

In this subsection, we want to show which level of accuracy the MR-FDPF model can normally achieve. Since currently, two groups of measurement data are available, we use them here to demonstrate the accuracy of the MR-FDPF model. The first group of measurements is from Stanford University which was conducted by Dr. Nicolai Czink in 2008 [61]. The second group was done in the CITI laboratory, INSA-Lyon, France.

4.1.5.1 Calibration with the measurements from Stanford University

The measurement data we use here to perform the calibration process corresponds to the "I2I stationary" scenario measurement.

The office scenario

The scenario was a typical 16m x 34 m office environment made of 30 cubicles and 7 small separated rooms. 8 transmitters and 8 receivers were distributed in the office as illustrated in Fig. 4.6. All of them were equipped with omnidirectional antennas and were fixed in their locations during the measurement. Four materials were mainly used in the office, i.e., *concrete* for the main walls, *plaster* for the internal walls, *glass* for the external glass wall and *wood* for the cubicles located in the central part of the office.

Measurement setup

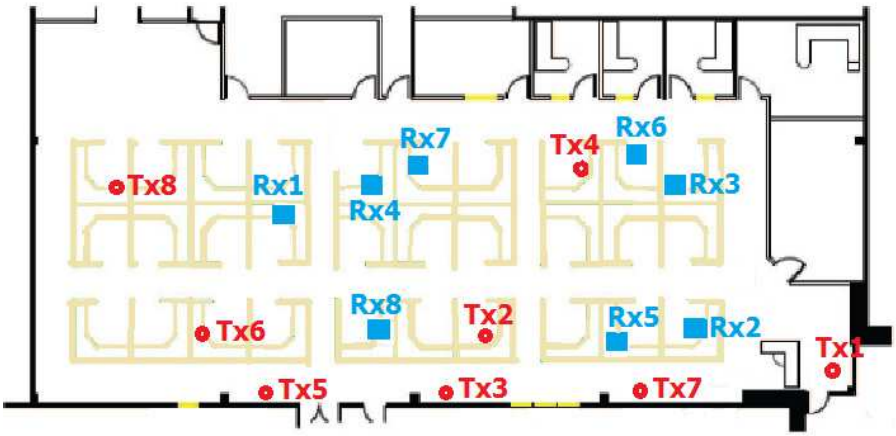

Figure 4.6: The measurement scenario.

Table 4.1: Parameter values of materials optimized from the calibration

	air	absorbant	wood	plaster	concrete	glass
n_{mat}	1.0	1.0	4.002058	1.5	5.4	2.1042523
a_{mat}	0.9999335	0.96879673	0.9999999	0.9999999	0.9999999	0.9999999

8 x 8 Multiple-Input Multiple-Output (MIMO) channels at a center frequency of 2.45 GHz were measured simultaneously with a RUSK MEDAV channel sounder [62]. In the measurement, 120 time blocks covering a total time of 32 seconds and 220 frequency bins covering a total bandwidth of 70 MHz were recorded.

Calibration with the measurements between all Txs and all Rxs

This calibration is performed with the measurement data from 64 links, i.e., the links between all the 8 Txs and all the 8 Rxs. The measurement data used to perform the calibration are taken only from the center frequency of 2.45 GHz, but are averaged along the time axis, i.e., averaged over the 120 time blocks.

The obtained parameter values of materials are listed in Table. 4.1. These parameter values are configured to run the MR-FDPF simulation at 2.45 GHz with 0 dBm transmit power. The discretization step is $\lambda/6 \approx 2$ cm. The radio

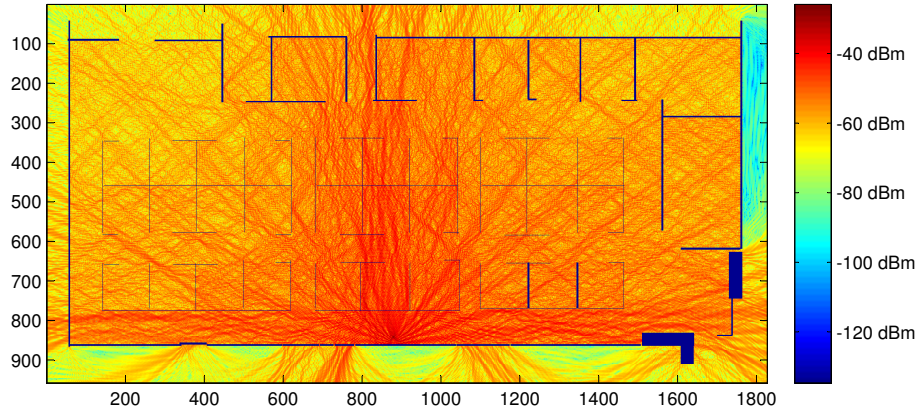

Figure 4.7: Radio coverage map of Tx3 simulated with the MR-FDPF model at 2.45 GHz plotted in dBm.

coverage map of Tx3 simulated with the MR-FDPF model is shown in Fig. 4.7 as an example.

The offset and the RMSE computed from the 64 links compared to the measurements are: *offset = -60.3912 dB; RMSE = 4.6618 dB;*

Calibration with the measurements between Tx1 and all Rxs

This calibration is performed with the measurement data from 8 links, i.e., the links between the Tx1 and all the 8 Rxs. The same as above, the measurement data used to perform the calibration are taken only from the center frequency of 2.45 GHz, but are averaged over the 120 time blocks.

The obtained parameter values of materials are listed in Table. 4.2.

Table 4.2: Parameter values of materials optimized from the calibration

	air	absorbant	wood	plaster	concrete
n_{mat}	1.0	0.75	1.5917009	2.2833333	3.0013716
a_{mat}	0.9999492	1.0	1.0	1.0	1.0

These parameters are configured to run the MR-FDPF simulatoins at totally 23 frequency bins covering the whole bandwidth of 70 MHz, i.e., a frequency spacing of 3.125 MHz and the 12-th frequency bin is centered at 2.45 GHz. This is a kind of wideband simulations which will be detailed in Chapter 6. Here, we

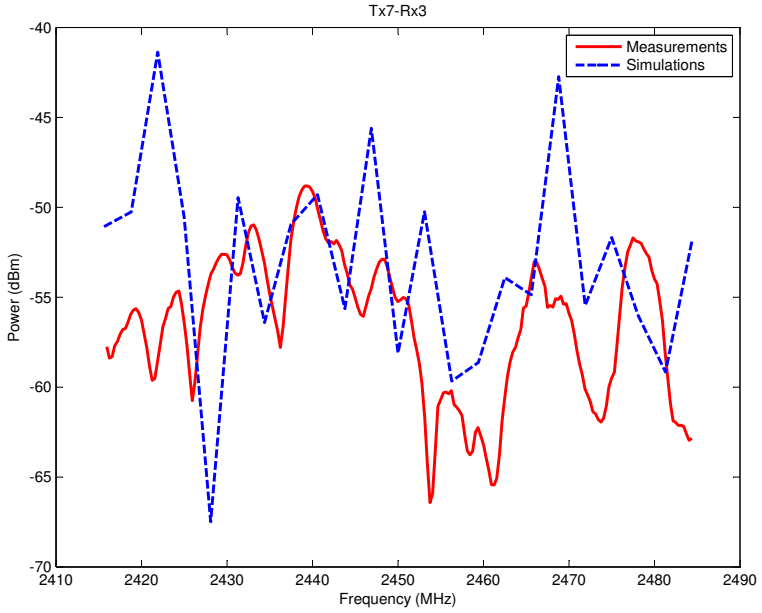

Figure 4.8: Comparison of the wideband fast fading characteristics of the link Tx7-Rx3 from the simulation and measurement

just present the wideband fast fading characteristics of the link Tx7-Rx3 in Fig. 4.8 as an example.

Thus, we can compute the offset and the RMSE between the simulations and measurements for the following three cases. The offset and the RMSE computed only from the 8 links are: *offset = -33.7677 dB; RMSE = 2.9488 dB;* The offset and the RMSE computed from all the 64 links are: *offset = -30.8306 dB; RMSE = 7.8923 dB;* The offset and the RMSE computed from all the 64 links and all the 23 frequency bins are: *offset = -30.6846 dB; RMSE = 8.7830 dB;*

From the above results, it is obvious that we get the minimum RMSE when all the simulated points are calibrated with the measurements. The less the simulated points are calibrated with the measurements, the larger the RMSE is.

4.1.5.2 Calibration with the measurements from the CITI laboratory

The measurements were done in the CITI laboratory, INSA-Lyon, France.

The scenario

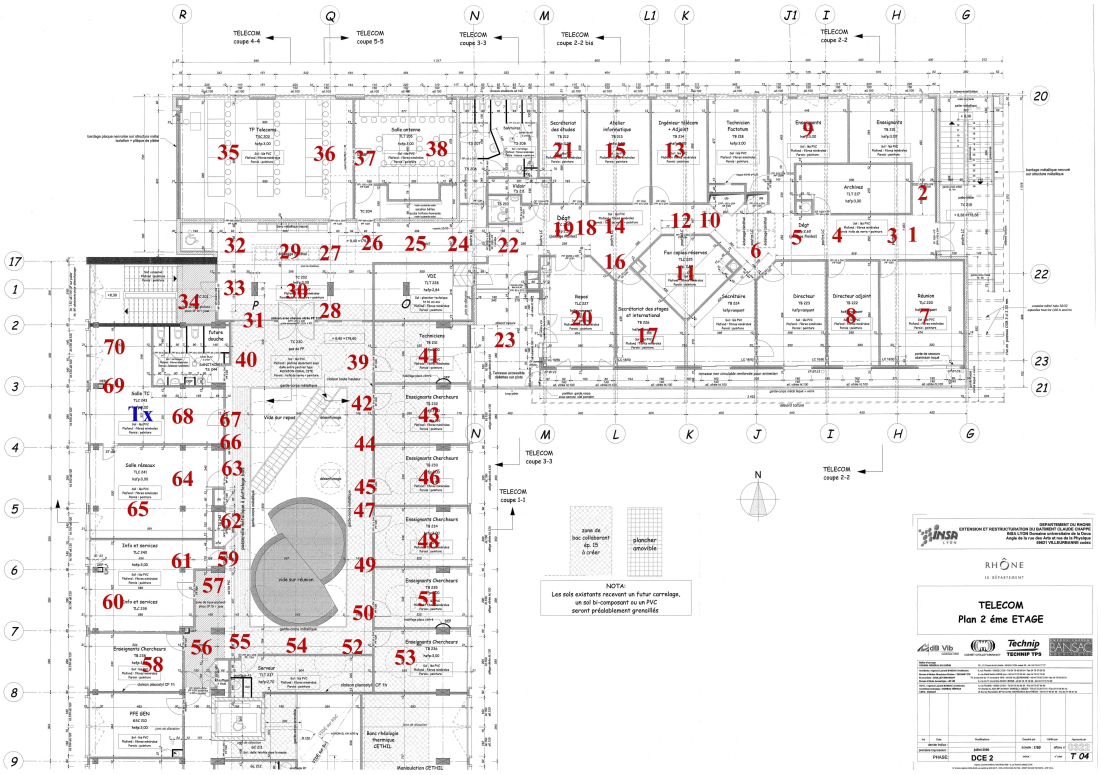

Figure 4.9: The CITI measurement scenario

The scenario is the CITI lab building at INSA-Lyon, France. The location of the transmitter is marked by "Tx" in Fig. 4.9. The numbers in Fig. 4.9 indicate the locations of the receivers. There are totally 70 numbers marked in Fig. 4.9, but the point 41 was not measured due to the closure of the office door. Hence, we finally have 69 measurement points.

Measurement setup

The measurements were done at 3.4 GHz. The transmitter included the arbitrary waveform generator (ESG4438C by Agilent Technology) and the 6 dBi omnidirectional antenna ECO6-3500. The equivalent isotropically radiated power (EIRP) was 20 dBm. The mean powers at the 69 points above were measured with the Handheld Spectrum Analyzer ROHDE & SCHWARZ FSH8 equipped with the omnidirectional antenna ECO6-3500 (see Fig. 4.10). The parameters of the FSH8 were configured as follows: F0 = 3.4 GHz; SPAN = 4.5 MHz; RBW = 300 KHz; SWT = 50 ms, where RBW and SWT denote the resolution bandwidth

Figure 4.10: The Spectrum Analyzer FSH8 and the omnidirectional antenna ECO6-3500

Table 4.3: Parameter values of materials optimized from the calibration

	air	absorbant	concrete	plaster	wood	glass	plastic
n_{mat}	1.0	1.0	5.4444447	1.9444444	1.1666666	1.4166667	1.25
a_{mat}	0.9996667	0.9688	1.0	1.0	1.0	1.0	1.0

and the sweep time, respectively.

Calibration

The calibration is performed with 12 measurement points: 1, 5, 7, 11, 15, 20, 24, 27, 28, 32, 35, 40. The parameter values of materials optimized from the calibration process are listed in Table. 4.3

The obtained parameter values are configured to run the MR-FDPF simulations at both 3.4 GHz and 3.5 GHz. And then the offset and the RMSE can be computed from all the 69 measurement points. Fig. 4.11 shows the radio coverage map predicted at 3.5 GHz with the MR-FDPF model as an example.

The offset and the RMSE computed from the 3.4 GHz MR-FDPF simulation

are: *offset = -43.0176 dB; RMSE = 8.4617 dB;* The offset and the RMSE computed from the 3.5 GHz MR-FDPF simulation are: *offset = -41.0173 dB; RMSE = 8.1095 dB.*

From the above results, we know that the calibrated parameter values optimized at a certain frequency can be used to simulate a nearby frequency. This is reasonable because although the parameters of materials are frequency-dependent in reality, they change slightly with frequency. Therefore, the parameter values of materials can be considered constant over a narrow frequency bandwidth.

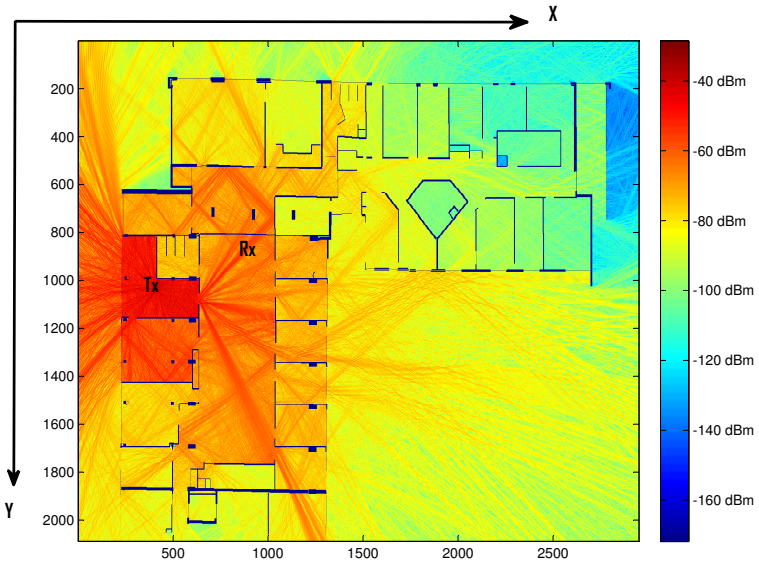

Figure 4.11: The coverage map predicted with the MR-FDPF model.

4.2 Extraction of the large scale propagation characteristics

In this section, we present the extraction of the large scale propagation characteristics, namely, the mean path loss and the shadow fading. First, the large scale propagation characteristics are described. Then whether or not the MR-FDPF model is capable of simulating the shadow fading phenomenon is checked. At last, how to extract the large scale propagation characteristics is addressed.

4.2.1 Large scale propagation characteristics

When expressed in dB, the instantaneous path loss can be considered as the sum of the mean path loss, shadow fading and small scale fading as follows [23]

$$PL(d) = L(d) + X_\sigma + F \tag{4.47}$$

where $PL(d)$, $L(d)$, X_σ and F denote the instantaneous path loss, the mean path loss, the shadow fading and the small scale fading associated with the Tx-Rx separation distance d, respectively. Unlike the small scale fading which characterizes the rapid fluctuations of the received signal strength over very short travel distances (a few wavelengths), the large scale fading, i.e., shadow fading, characterizes signal strength variation over large distances [4].

Typically, the mean path loss $L(d)$ is deterministic and is log dependent on the Tx-Rx separation distance d according to the one-slope model as follows

$$L(d) = L_0 + 10n \cdot \log_{10}(d) \tag{4.48}$$

where L_0 is a constant which accounts for system losses and n is the path loss exponent depending on the specific propagation environment. For instance, in free space propagation, $n = 2$.

The shadow fading X_σ is a zero-mean Gaussian distributed random variable (in dB) with the standard deviation σ.

The small scale fading is typically described by the Rayleigh distribution for the NLOS propagation or the Rice distribution for the LOS propagation [4].

The large scale propagation characteristics are very useful for determining the coverage area or evaluating system performance. For instance, with the large scale propagation characteristics, system designers can determine how large the coverage area of a transmitter is and how much fade margin is required to achieve a certain level of edge reliability.

4.2.2 The measurements and the MR-FDPF simulation

In order to extract the large scale propagation characteristics based on the MR-FDPF model, the MR-FDPF simulation is the first step. Moreover, in order

to verify the extraction results from the MR-FDPF model, measurements are necessary.

We use here the "I2I moving receivers" scenario measurements from Stanford University [61] to verify our simulation results. Everything in the "I2I moving receivers" scenario measurements was the same as in the "I2I stationary" scenario measurements stated in Subsection 4.1.5.1 except that the 8 receivers were randomly moved inside their cubicles when conducting the measurements. For the large scale fading study, narrowband measurements are sufficient, hence the measurement data are restricted to the center frequency of 2.45 GHz. And note that the averaging over the 120 time blocks implies the averaging over space since the receivers were moving when recording.

The MR-FDPF model is configured with the parameter values of materials given in Table. 4.1 optimized from the "I2I stationary" scenario measurements. The MR-FDPF simulation is performed at 2.45 GHz with 0 dBm transmit power. The discretization step is $\lambda/6 \approx 2$ cm. An example of the radio coverage map can be referred to Fig. 4.7.

4.2.3 Capability of simulating shadow fading phenomenon

From a theoretical point of view, the small scale fading and shadow fading can be averaged out over an area, e.g. a square area of a proper size. In other words, neither the small scale fading nor the shadow fading can be observed if the averaging area is large enough. The obtained path loss curve after averaging over a large enough area will be very smooth because it only contains the mean path loss.

If the MR-FDPF model is capable of simulating the fading characteristics, it should show the averaging effect described above. Therefore, we investigate this by performing averaging over square areas of different sizes, from $5\lambda \times 5\lambda$ to $50\lambda \times 50\lambda$, with a step of 5λ, where λ denotes the wavelength. The averaging effect from the MR-FDPF model is shown in Fig. 4.12. In this figure, a shadowing effect is evidenced over $5\lambda \times 5\lambda$ area, and $10\lambda \times 10\lambda$ area too, but there is a trend: the larger the size of the averaging area is, the less the shadowing effect can be observed. When the size of the area is about $40\lambda \times 40\lambda$, the shadowing effect

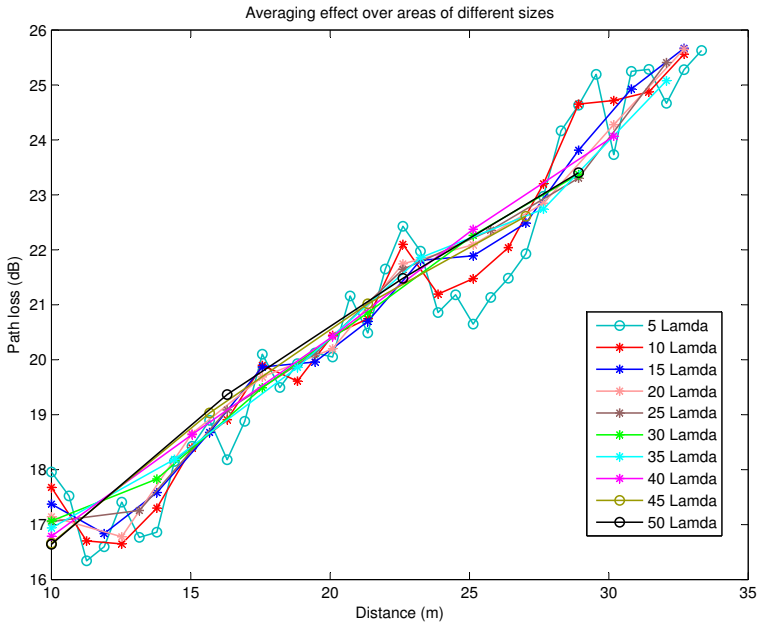

Figure 4.12: The averaging effect over areas of different sizes.

almost can not be observed, which means that the shadowing has been averaged out. Fig. 4.12 demonstrates that the MR-FDPF model is capable of simulating the shadow fading.

4.2.4 Extraction of the large scale propagation characteristics

In order to get the large scale propagation characteristics, first we should average out the small scale fading. The obtained path loss after averaging out the small scale fading is usually called the local mean path loss. The most critical point for averaging out the small scale fading is the determination of the size of the averaging area.

According to [18][37], if the samples are expressed in dB, the number of samples associated with 90% confidence interval is $N = 85$. Provided that for the MR-FDPF model, a square area can be chosen, the number of samples associated with each side of the square is thus $\sqrt{N}$. In addition, for a Rayleigh distributed signal envelope, the uncorrelated distance for two adjacent samples

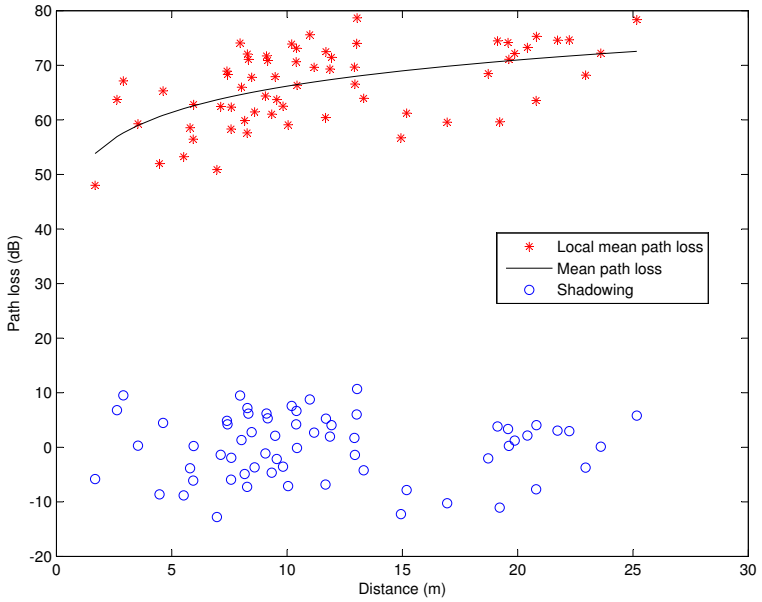

Figure 4.13: The obtained local mean path loss, mean path loss and shadowing from the MR-FDPF model.

is 0.38λ [37]. Finally, we obtain the minimum length of the side of the square is $0.38\lambda \times \sqrt{N} \approx 3.8\lambda$. On the other side, if it is a LOS propagation scenario, the received signal envelope may be Rice distributed rather than Rayleigh, then in this case a smaller sample size may be sufficient [37].

According to the description above, the local mean path loss averaged over an area of $3.8\lambda \times 3.8\lambda$ is obtained, shown in Fig. 4.13 by the red stars.

The local mean path loss includes both the mean path loss and the shadow fading. Since the mean path loss depends on the log distance shown in Eq. 4.48, we choose to get the L_0 and n by using the curve fitting tool of Matlab such that the difference between the local mean path loss and the estimated mean path loss is minimized in a mean square error sense. Substituting the estimated $L_0 = 50.26$ and $n = 1.592$ into Eq. 4.48, we obtain the mean path loss

$$L(d) = 50.26 + 10 \times 1.592 \cdot \log_{10}(d) \tag{4.49}$$

Here $n = 1.592$ indicates that there exists a waveguide effect in the propagation. The obtained mean path loss is shown by the black continuous curve in Fig. 4.13. Finally, the shadow fading can be obtained by just subtracting the mean path

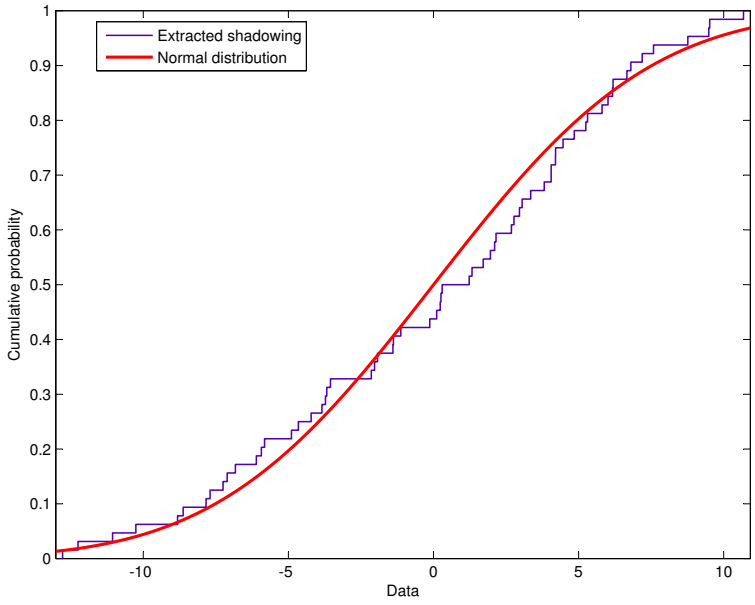

Figure 4.14: CDF comparison between the extracted shadow fading from the MR-FDPF model and normal distribution.

loss from the local mean path loss, which is denoted by the blue circles in Fig. 4.13.

In order to validate the shadow fading we have extracted, we compare its Cumulative Distribution Function (CDF) with that of a normal distribution. The comparison result is shown in Fig. 4.14. From the figure, we can see that the extracted shadow fading and the theoretical result are very similar.

Moreover, we also compute the standard deviation of the extracted shadow fading. It is 5.87 dB.

4.2.5 Experimental evaluation

Here, we extract the large scale propagation characteristics from the measurements. First of all, we obtain the local mean power by averaging over the 120 time blocks, which is shown by the red stars in Fig. 4.15. In the same way as in the simulation, the deterministic mean path loss is obtained by curve fitting

$$L(d) = 47.25 + 10 \times 1.442 \cdot \log_{10}(d) \tag{4.50}$$

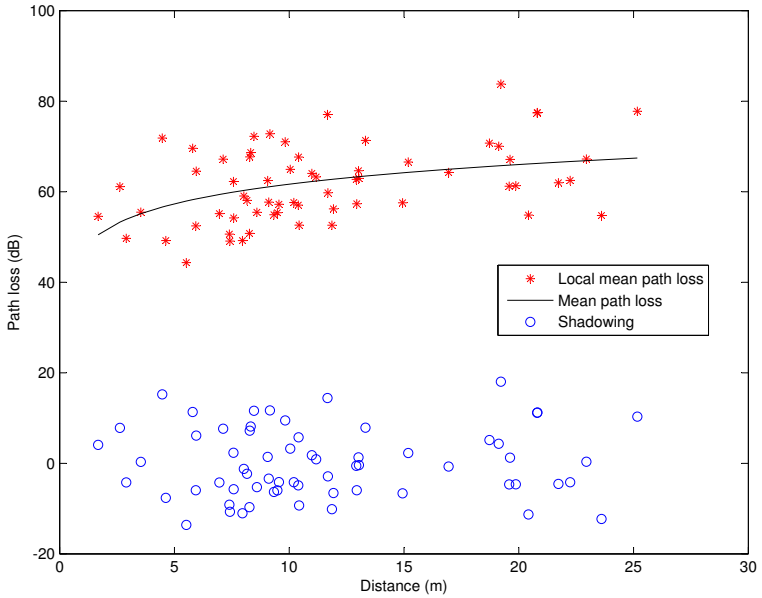

Figure 4.15: The obtained local mean path loss, mean path loss and shadowing from the measurements.

The mean path loss is shown in Fig. 4.15 by the black continuous curve. Once we get the mean path loss, the shadow fading is obtained by subtracting the mean path loss from the local mean path loss, which is denoted by the blue circles in Fig. 4.15.

The CDF comparison between the extracted shadow fading and normal distribution is shown in Fig. 4.16. This good match demonstrates that the proposed approach for extracting the shadow fading is effective. The standard deviation of the extracted shadow fading from the measurement is 7.66 dB.

Finally, by comparing the parameters extracted from the MR-FDPF model and the measurements in Table. 4.4, we can see that they fit each other very well. The path loss exponents n from both the MR-FDPF model and measurements are smaller than 2, which indicates that there exists a waveguide effect in the propagation. The standard deviation of shadowing from simulation is slightly lower than that from the measurements. We suggest that this is due to the unmodeled furniture which would contribute more to fading. The match between the simulation and measurements demonstrates that the MR-FDPF model is capable of simulating the large scale propagation characteristics.

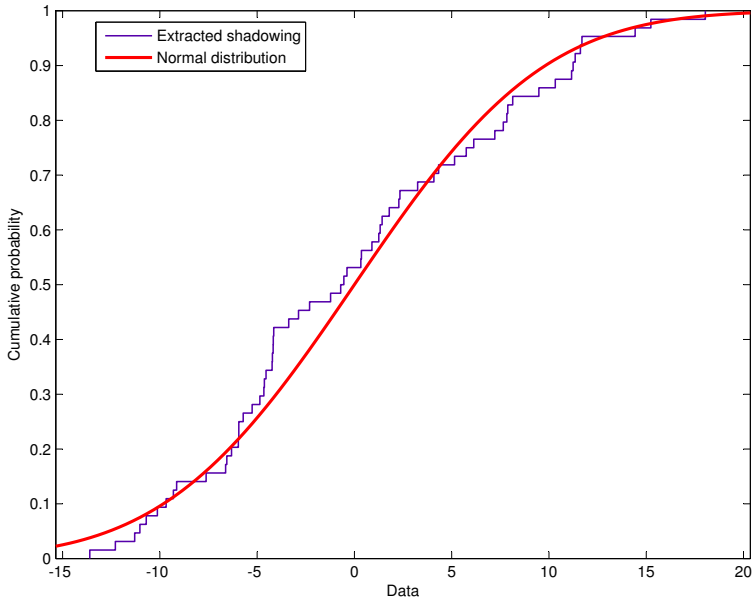

Figure 4.16: CDF comparison of the extracted shadowing and normal distribution from the measurements.

Table 4.4: Comparison between the simulation and the measurements

	n	The standard deviation σ
MR-FDPF	1.59	5.87 dB
Measurement	1.44	7.66 dB

4.3 Extraction of the small scale fading statistics

In this section, we describe how the small scale fading statistics can be extracted from the electric field strength predicted by the MR-FDPF model. The extraction performance is verified by comparisons with the measurement results.

4.3.1 Extraction of the small scale fading statistics

Since Doppler effects can normally be ignored in indoor scenarios, we assume that the indoor radio channels are time-invariant. Thus, the general time-variant

impulse response $h(t,\tau)$ becomes $h(\tau)$. For different positions in a radio coverage, the impulse responses are different, which means the impulse responses are functions of position $\vec{r}$. Here, we use the vector position $\vec{r}$ because the relative positions of neighbor pixels will be used and the wavevector $\vec{k}$ will be estimated. Transform the impulse response $h(\tau,\vec{r})$ into the frequency domain by the Fourier transform, we get the transfer function $H(f,\vec{r})$.

For the MR-FDPF model, since the transmit signal is always known, the electric field strength predicted with the MR-FDPF model at the position $\vec{r}$ can be equivalently described in terms of the transfer function $H(f,\vec{r})$ of the propagation channel between the transmitting antenna and a virtual receiving antenna located at the position $\vec{r}$.

At every position $\vec{r}$, the electric field strength and, consequently, the radio channel transfer function $H(f,\vec{r})$ satisfies the wave equation [9]. Thus, the transfer function $H(f,\vec{r})$ can be legitimately represented by the Stochastic Local Area Channel (SLAC) model [57] defined as follows

$$H(f,\vec{r}) = \sum_{l=1}^{N} \alpha_l \exp(j[\Phi_l - \vec{k}_l \cdot \vec{r} - 2\pi f \tau_l]) + w(f,\vec{r}) \tag{4.51}$$

Each plane wave in Eq. 4.51 is characterized by the constant amplitude α_l, the wavevector $\vec{k}_l$, the time delay τ_l, and the phase Φ_l which is a realization of the random variable following the uniform distribution over the interval $[0, 2\pi]$. The term $w(f,\vec{r})$ in Eq. 4.51 corresponds to the diffuse wave component [57].

Implicitly, in Eq. 4.51, we assume that the transfer function $H(f,\vec{r})$ as well as the electric field strength predicted by the MR-FDPF model is a realization of the corresponding stochastic process. This assumption can be justified by observing that multiple uncertainties are inherent in modeling any complex propagation scenario. For example, adjustments (corrections) made to the model geographical database would result in a new realization of the predicted transfer function $H(f,\vec{r})$.

We also presume that the diffuse wave component $w(f,\vec{r})$ in Eq. 4.51 is a realization of a random zero-mean complex Gaussian process uncorrelated with respect to the frequency f and the spatial position $\vec{r}$.

The parameters $\left\{\alpha_l, \tau_l, \vec{k}_l\right\}_{l=1}^{N}$ of the SLAC model in Eq. 4.51 are then determined by using the well-known Space-Alternating Generalized Expectation-maximization algorithm (SAGE) [63]. Note that under assumptions made above, the estimates $\left\{\hat{\alpha}_l, \hat{\tau}_l, \hat{\vec{k}}\right\}_{l=1}^{N}$ obtained by the SAGE algorithm asymptotically approach the Maximum-Likelihood (ML) estimates.

The estimated parameters $\left\{\hat{\alpha}_l, \hat{\tau}_l, \hat{\vec{k}}\right\}_{l=1}^{N}$ of the SLAC model in Eq. 4.51 allow determining the statistical properties of the radio channel corresponding to the link between the transmitter and receiver positions. The statistical properties, namely the Power Delay Profile (PDP) $\hat{P}_h(\tau)$, the envelope Probability Density Function (PDF) $\hat{f}_R(\rho)$, the Frequency Correlation Function (FCF) $\hat{R_H}(\Delta f)$, the Rice factor $\hat{K}$, the mean delay $\hat{\tau}_m$, and the root mean square delay $\hat{\tau}_{rms}$ are calculated as follows [64]:

$$\hat{P}_h(\tau) = \sum_{l=1}^{N} |\hat{\alpha}_l|^2 \delta\left(\tau - \hat{\tau}_l\right) \tag{4.52}$$

$$\hat{f}_R(\rho) = \rho \int_0^{\infty} J_0(\upsilon\rho)[\prod_{l=1}^{N} J_0(\hat{\alpha}_l \upsilon)]\upsilon d\upsilon \tag{4.53}$$

$$\hat{R_H}(\Delta f) = \sum_{l=1}^{N} |\hat{\alpha}_l|^2 \exp(-j2\pi\hat{\tau}_l \Delta f) \tag{4.54}$$

$$\hat{K} = \frac{\max\left((\hat{\alpha}_l)^2\right)}{\sum_{l=1}^{N} (\hat{\alpha}_l)^2 - \max\left((\hat{\alpha}_l)^2\right)} \tag{4.55}$$

$$\hat{\tau}_m = \frac{\sum_{l=1}^{N} \hat{\tau}_l \hat{\alpha}_l^2}{\sum_{l=1}^{N} \hat{\alpha}_l^2} \tag{4.56}$$

$$\hat{\tau}_{rms} = \sqrt{\frac{\sum_{l=1}^{N} \left(\hat{\tau}_l - \hat{\tau}_m\right)^2 \hat{\alpha}_l^2}{\sum_{l=1}^{N} \hat{\alpha}_l^2}} \tag{4.57}$$

Furthermore, multiple realizations of the transfer function $H(f, \vec{r})$ can be obtained by substituting the estimated parameters $\left\{\hat{\alpha}_l, \hat{\tau}_l, \hat{\vec{k}}_l\right\}_{l=1}^{N}$ into the SLAC model in Eq. 4.51.

4.3.2 Experimental evaluation

In order to verify the proposed method, we conduct both simulations and measurements.

4.3.2.1 Simulation scenario

In the simulation, CITI lab has been chosen as the indoor propagation scenario where the MR-FDPF model is used. An example of the radio coverage map of the CITI lab predicted with the MR-FDPF model is given in Fig. 4.11. In order to extract the fading statistics, the simulations have been performed at 41 frequencies, at the range from 3.477 GHz to 3.523 GHz, with the frequency step of 1.152 MHz. The discretization step of the MR-FDPF model is $\lambda/6 \approx 1.4$ cm. The locations of the transmitter and the virtual receiver are indicated by Tx and Rx, respectively, in Fig. 4.11. The Rx is a virtual rectangular antenna array consisting of $7 \times 7 = 49$ equidistant elements (see Fig. 4.17) with spacing equal to 1.4 cm, i.e., the discretization step. The transmit power is 17 dBm. The SAGE algorithm is applied to the predicted channel transfer function. The number of multiple paths is assumed to be 15.

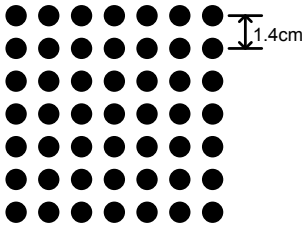

Figure 4.17: The virtual rectangular antenna array of Rx.

4.3.2.2 Measurement setup

The measurement is conducted at the same position in CITI lab as shown in Fig. 4.11. The transmitter includes the arbitrary waveform generator (ESG4438C by Agilent Technology) and the directional horn antenna (3164-08 by ETS-Lindgren). The vector signal analyser (VSA 89641 by Agilent Technology) is equipped with a 3.5 GHz, 6 dBi, omnidirectional antenna ECO6-3500. The 0.2 dB bandwidth of the VSA is 20 MHz. Fourteen measurements corresponding to different time instances have been conducted. For each measurement, 9 positions, i.e., 3×3 rectangular antenna array with spacing equal to $\lambda/2 \approx 4.2$ cm (see Fig. 4.18) are measured around the Rx in Fig. 4.11. For each referred receiving position, 4608080 samples are collected during 100 ms.

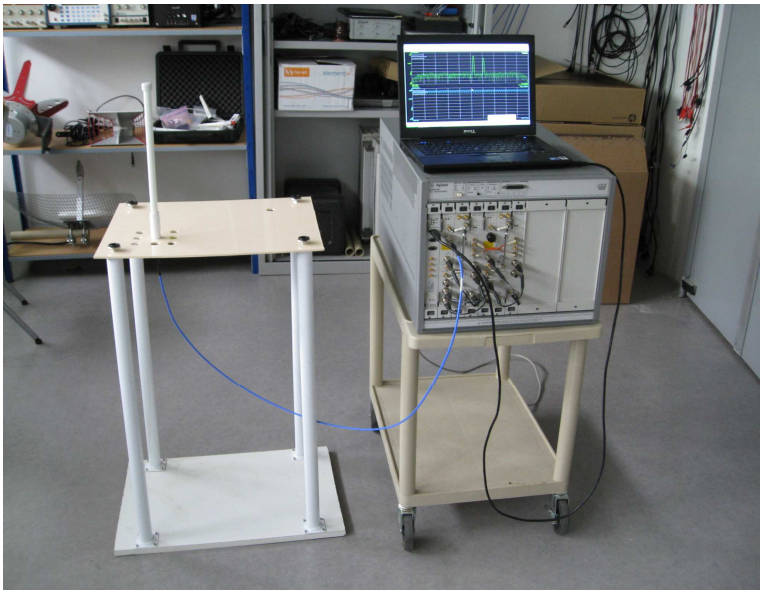

Figure 4.18: The 3×3 rectangular antenna positions.

4.3.2.3 Results

In order to evaluate the proposed approach, we compare the simulation and measurement results. Fig. 4.19 presents the comparison of channel impulse responses of the SLAC model and that obtained directly by the MR-FDPF model. The

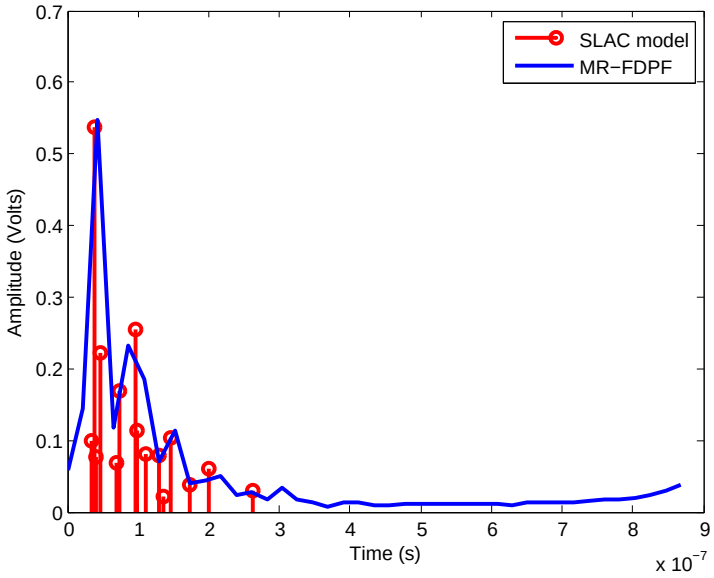

Figure 4.19: The comparison of the impulse response.

channel impulse response of the SLAC model is obtained according to

$$\hat{h}(\tau) = \sum_{l=1}^{N} \hat{\alpha}_l \delta(\tau - \hat{\tau}_l) \tag{4.58}$$

And the channel impulse response directly by the MR-FDPF model is obtained by applying the Inverse Fast Fourier Transform (IFFT) to the transfer functions. We can see that they have a good match in Fig. 4.19. The envelope PDF of the SLAC model estimated by the proposed approach according to Eq. 4.53 has also been compared to the histogram of channel transfer function in Fig. 4.20. The histogram of the envelope of the measured channel transfer function is depicted in Fig. 4.21. The Rayleigh PDF curve is also plotted for comparison reasons. From Fig. 4.20 we see that the PDF of the SLAC model fits very well the PDF of the MR-FDPF model. Furthermore, both of them match the PDF obtained from the measurements and shown in Fig. 4.21.

The angular power spectrum of the SLAC model is given in Fig. 4.22. The relative position of the transmitter and the receiver is also shown in Fig. 4.22. As can be seen from Fig. 4.22, the estimated angles are grouped near 180 and 0/360 degrees. The group around 180 degrees includes the LOS direction, which

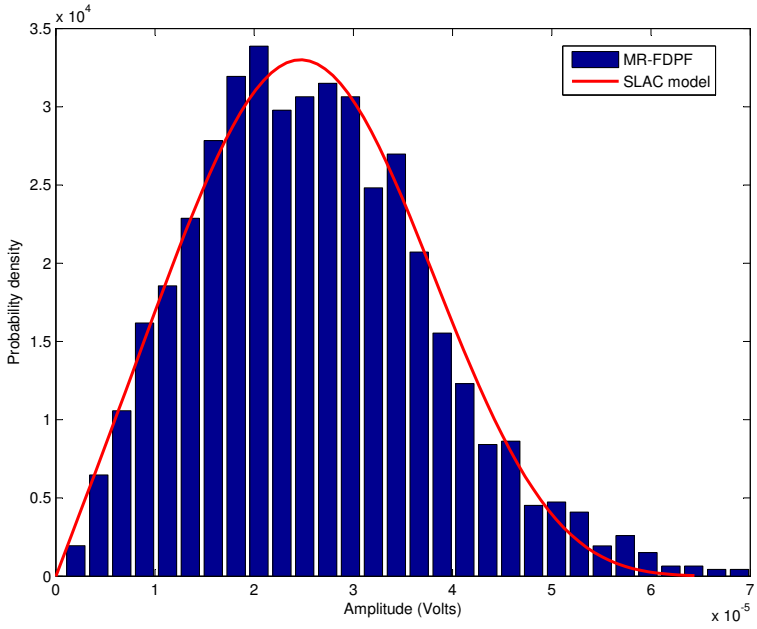

Figure 4.20: The comparison of the channel envelope PDFs.

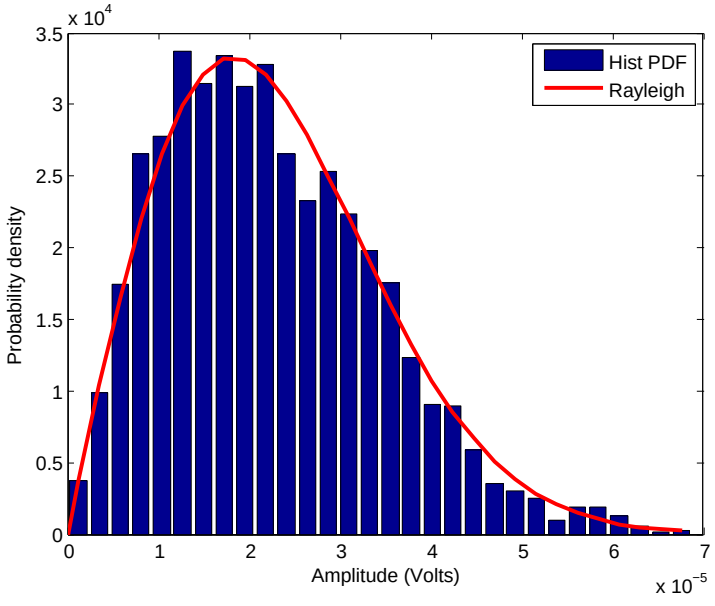

Figure 4.21: The histogram PDF of measurements.

is approximately equal to 160 degrees. The second group, i.e., the waves with the angles near 0/360 degrees are mainly due to the reflection by the walls behind the Rx.

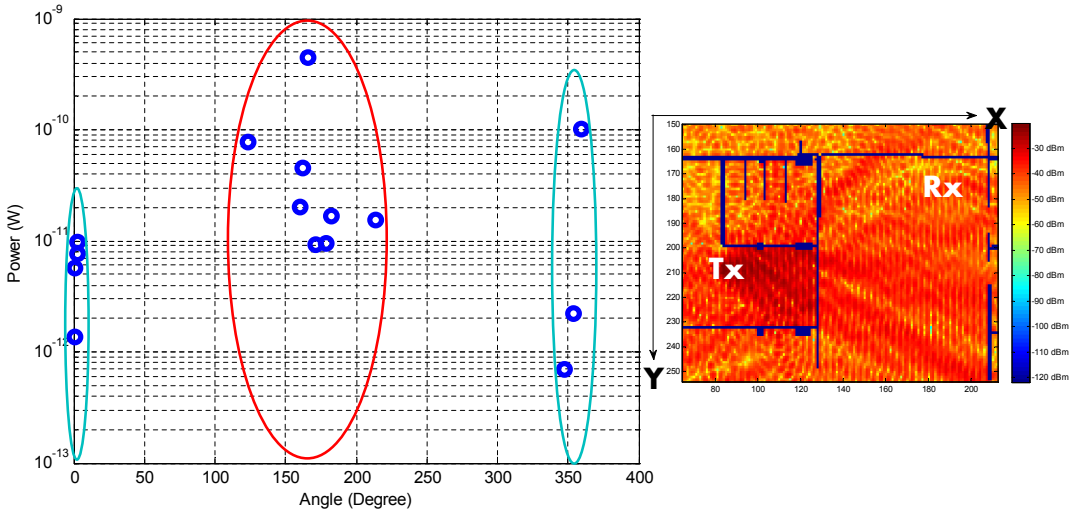

Figure 4.22: The estimated channel angular power spectrum.

By the proposed approach, we can also obtain the estimated Rice K factor, root mean square delay, mean delay and FCF from the predictions provided by the MR-FDPF model. The results are presented in the Table 4.5 and Fig. 4.23, respectively. The 95% confidence intervals calculated using the Chebyshev's inequality from the measurements are also given in Table 4.5. It can be seen that the simulated Rice K factor is well located in the 95% confidence intervals of the measurements, but the simulated root mean square delay is a bit small and is located outside the confidence interval. We suggest that this is maybe also due to the unmodeled furniture which would contribute more to multipaths.

The angular spectrum, the mean delay and the FCF estimated by the proposed approach can not be compared with the characteristics estimated from the measurements as the measurements taken at different time instances can not be synchronized on the VSA 89641.

From what we can compare and what we have compared, we can see that the MR-FDPF model appears to be capable of providing the small scale fading

Table 4.5: Comparison of the estimated values from the SLAC model and measurements

Parameters	From the SLAC model	Mean Values from Measurements	Confidence Intervals
$\hat{K}$	1.3979	1.4705	$[1.1611, 1.7798]$
$\hat{\tau}_{rms}$	$3.178 \times 10^{-8}s$	$5.2711 \times 10^{-8}s$	$[4.4794 \times 10^{-8}s, 6.0628 \times 10^{-8}s]$
$\hat{\tau}_m$	$5.7568 \times 10^{-8}s$		

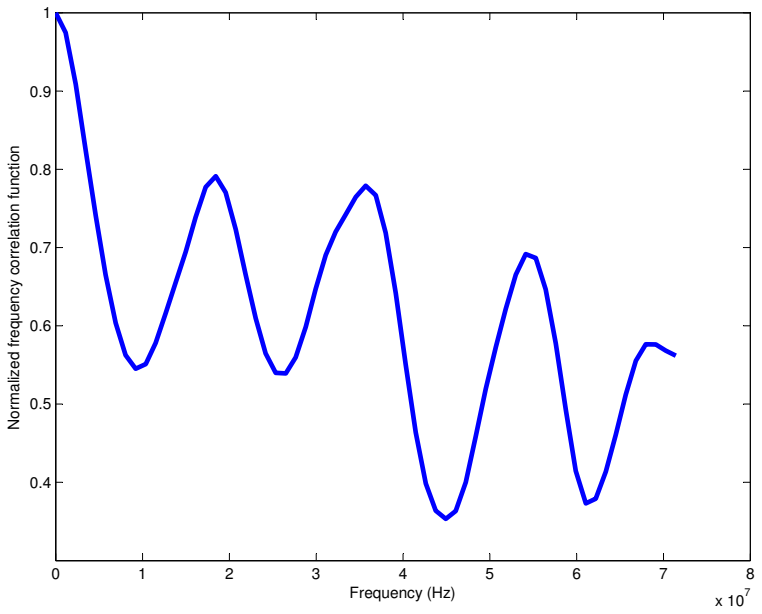

Figure 4.23: The normalized FCF obtained from the SLAC model.

and the proposed approach is efficient in extracting the small scale fading statistics. However, a further validation of the simulated results will be appreciated if a synchronized Single-Input Multiple-Output (SIMO) measurements can be performed.

4.4 A semi-deterministic model

Based on the extracted large scale propagation characteristics and the small scale fading statistics in the previous two sections, we propose here a semi-deterministic channel model which is based on the deterministic MR-FDPF model, but introduces a stochastic part to take into account the random aspect of the realistic channels.

This semi-deterministic channel model has the form of Eq. 4.47 in dB

$$PL(d) = L(d) + X_\sigma + F \tag{4.59}$$

The parameters in this model can be determined as follows:

1. The deterministic path loss $L(d)$ can be determined by the extraction approach of the large scale propagation characteristics based on the MR-FDPF simulations stated in Section 4.2.

2. The second term X_σ is a zero-mean Gaussian distributed random variable whose standard deviation can be determined by the extraction approach also in Section 4.2.

3. The third term F is the small scale fading random variable whose envelope PDF can be determined either by the estimated PDF in Eq. 4.53 or by the estimated Rice K factor in Eq. 4.55 stated in Section 4.3.

4.5 Chapter summary

This chapter first gave a detailed introduction of the MR-FDPF model. Then the large scale propagation characteristics were described and extracted based on the MR-FDPF model. After that, the small scale fading statistics were extracted by using the SAGE algorithm based on the simulated electric field provided by

the MR-FDPF model. The extracted large scale and small scale fading statistics have been verified by comparisons with the measurements. Finally, based on the extraction of the large scale propagation characteristics and the small scale fading statistics, a semi-deterministic model was proposed which introduces a stochastic part to take into account the random aspect of the realistic channels.

Chapter 5

Realistic prediction of BER for adaptive modulation

The Bit Error Rate (BER) is an important parameter for evaluating the performance of wireless networks. Many wireless applications, such as, adaptive modulation and coding (AMC) scheme, or optimal power allocation, use the BER to dynamically adapt their schemes. Hence, a realistic and accurate prediction of BER is crucial for these higher-layer protocols and applications.

Moreover, from the channel modeling perspective, many radio propagation simulators provide the mean power prediction. However, only mean power is not enough to fully describe the behavior of radio channels. Realistic radio channels are random processes and present fading due to e.g. movements of surrounding objects. A fine radio propagation simulator should also be able to provide the fading information, and thus an accurate BER prediction can be achieved. Actually, the BER statistics is indeed the input needed by network simulators, e.g. NS-3, to perform realistic simulations.

In this chapter, a realistic BER for indoor wireless transmissions is predicted. It can be divided into two parts. The first part is for Single-Input Single-Output (SISO) systems, whereas the second part is for the Maximum Ratio Combining (MRC) diversity systems. With the predicted BER, adaptive modulation is implemented for both systems at the end.

5.1 Theoretical BER analysis

Theoretically, the average BER over fading channels can be obtained by averaging the corresponding BER of Additive White Gaussian Noise (AWGN) channels over the PDF of the instantaneous SNR which depends on the fading [25]. That is

$$P_{b:fading}(E) = \int_0^\infty P_{b:AWGN}(E;\gamma)P_\gamma(\gamma)d\gamma \tag{5.1}$$

where $\gamma \triangleq \alpha^2 E_b/N_0$ denotes the instantaneous SNR per bit, α is the fading amplitude, E_b is the signal energy per bit, N_0 is the noise power spectral density, $P_\gamma(\gamma)$ is the PDF of the instantaneous SNR depending on the fading, $P_{b:fading}(E)$ is the BER over fading channels and $P_{b:AWGN}(E;\gamma)$ is the BER over AWGN channels conditioned on the fading. The $P_{b:AWGN}(E;\gamma)$ can be obtained by substituting γ for E_b/N_0 in the BER over AWGN channels $P_{b:AWGN}(E)$.

Normally, the $P_{b:AWGN}(E)$ is a Gaussian Q-function for the ideal coherent detection and the desired form of the Gaussian Q-function is

$$Q(x) = \frac{1}{\pi}\int_0^{\pi/2} \exp(-\frac{x^2}{2\sin^2\theta})d\theta \tag{5.2}$$

Making use of the definition of the MGF in Eq. 3.29, we come to a unified and simplest way for computing the $P_{b:fading}(E)$ since the MGFs of a number of fading models are already available. Then typically, the $P_{b:fading}(E)$ is just a single integral with finite limits and integrand containing the MGF of the fading.

One point we should emphasize is that the $P_{b:AWGN}(E)$ here which is used to compute the $P_{b:fading}(E)$ should not be the commonly used approximate AWGN BER obtained from the approximate relationship between the BER $P_b(E)$ and Symbol Error Rate (SER) $P_s(E)$ as follows

$$P_b(E) \cong \frac{P_s(E)}{\log_2 M} \tag{5.3}$$

because this approximation is only valid for large symbol SNR, but the limits of the integral in Eq. 5.1 are from zero to infinity (i.e. γ can vary from zero to infinity over fading channels). The $P_{b:AWGN}(E)$ used here should be either the exact AWGN BER or the approximate AWGN BER which is accurate at both low and high SNR.

Here, we adopt the approximate AWGN BER of Lu et al. [65] as the $P_{b:AWGN}(E)$ to compute the $P_{b:fading}(E)$ since it is very accurate at both low and high SNR and it is much simpler than the exact AWGN BER [66][67][68][69].

Thus, for M-PSK modulations, we have

$$P_{b:AWGN}(E) \cong \frac{2}{\max(\log_2 M, 2)} \cdot \sum_{i=1}^{\max(\frac{M}{4},1)} Q\left(\sqrt{\frac{2E_b \log_2 M}{N_0}} \sin\frac{(2i-1)\pi}{M}\right) \quad (5.4)$$

where M is the modulation order, e.g. $M = 2$ for BPSK, $M = 4$ for QPSK.

For M-QAM modulations, we have

$$P_{b:AWGN}(E) \cong \frac{4}{\log_2 M}(1 - \frac{1}{\sqrt{M}}) \cdot \sum_{i=1}^{\sqrt{M}/2} Q\left((2i-1)\sqrt{\frac{3E_b \log_2 M}{N_0(M-1)}}\right) \quad (5.5)$$

Therefore, for the BER for the M-PSK modulations over fading channels, we have

$$P_{b:fading}(E) \cong \frac{2}{\max(\log_2 M, 2)} \cdot \sum_{i=1}^{\max(\frac{M}{4},1)} \frac{1}{\pi}\int_0^{\pi/2} M_\gamma\left(-\frac{\log_2 M}{\sin^2\theta}\sin^2\frac{(2i-1)\pi}{M}\right)d\theta \quad (5.6)$$

For the BER for the M-QAM modulations over fading channels, we have

$$P_{b:fading}(E) \cong \frac{4}{\log_2 M}(1 - \frac{1}{\sqrt{M}}) \cdot \sum_{i=1}^{\sqrt{M}/2} \frac{1}{\pi}\int_0^{\pi/2} M_\gamma\left(-\frac{(2i-1)^2 \cdot 3 \cdot \log_2 M}{2\sin^2\theta \cdot (M-1)}\right)d\theta \quad (5.7)$$

From above, it is noticed that the BER over fading channels depends exactly on the MGF of fading channels. Recall the MGF of fading channels provided in Chapter 3, we know that the MGF of fading channels is usually related to the fading parameters and the average SNR. Therefore, in the following section, we introduce the methods for estimating the fading parameters, namely, the Rice K factor and the m parameter of the Nakagami-m fading.

5.2 Estimation of the fading parameters

The widely used multipath fading channels are Rayleigh, Rice or Nakagami-m fading channels. Rayleigh fading has no fading parameters, so there are totally

two fading parameters to be estimated: the Rice K factor for the Rice fading and the m parameter for the Nakagami-m fading.

5.2.1 Estimation of the Rice K factor

The Rice K factor is defined as the ratio of the power of the LOS component to the NLOS components (usually called diffuse components):

$$K = \frac{A^2}{2\sigma^2} \tag{5.8}$$

where A is the amplitude of the LOS component and $2\sigma^2$ is the variance of the diffuse components. Over the past few decades, the estimation of the Rice K factor has attracted great interest [70][71][72] since the Rice K factor is an indicator of the radio link quality.

The most commonly used method for estimating the Rice K factor is the moment-based method [70] because of its simplicity compared to other methods, such as the ML method [71][72]. However, the moment-based method has its limitation: when the Rice K factor values are small, the moment-based method can provide sometimes physically meaningless results [71][72][73]. In other words, the moment-based method only works well for large Rice K factor values. However, for the indoor scenarios, the Rice K factor is usually small at most of positions due to the rich presence of the walls and furniture. Furthermore, we would like to provide a Rice K factor map of the whole building, so we hope the applicable range of the estimation method can be as large as possible. Thus, we decide not to use the traditional moment-based method, but the RICEFIT method developed by Ridgway in Matlab [74]. We choose the RICEFIT method also because it estimates the A and σ separately. This is important for the goodness of fit tests in the following subsection where a fully specified CDF is needed, since only a Rice K factor can not completely determine the CDF of a Rice distribution.

5.2.2 Estimation of the m parameter

There exist a number of methods for estimating the m parameter of the Nakagami-m fading [75][76][77][78][79]. From the Eq. 2.15, we know that the

m parameter can be estimated by estimating the Rice K factor first, and then map it to the m parameter. On the other hand, we can also estimate the m parameter by the Greenwood's method [78] since it outperforms other estimators [76]. The Greenwood's method is stated briefly as follows [76]

$$\hat{m} = \begin{cases} \frac{0.5000876+0.1648852y-0.0544274y^2}{y}, & 0 < y \leq 0.5772 \\ \frac{8.898919+9.059950y+0.9775373y^2}{y(17.79728+11.968477y+y^2)}, & 0.5772 < y < 17 \end{cases} \tag{5.9}$$

where $y = ln(\hat{\mu}_2/G)$, $ln(\cdot)$ denotes the natural logarithm operator, $\hat{\mu}_2$ is the arithmetic mean of sample power, i.e. $\hat{\mu}_2 = \frac{1}{N}\sum_{n=1}^{N} x_n^2$, and G is the geometric mean of sample power $G = \left(\prod_{n=1}^{N} x_n^2\right)^{1/N}$.

5.2.3 Remarks of goodness of fit tests

The Kolmogorov-Smirnov test [80] is one of the most well-known goodness of fit tests which is based on the maximum absolute vertical difference between the empirical distribution function (EDF) $F_n(x)$ and the hypothetical distribution function $F(x)$. The Kolmogorov-Smirnov test has the advantage of no assumptions made about the distribution of the data. However, the classic Kolmogorov-Smirnov test with the standard table of critical values is only valid when the $F(x)$ is fully specified. If the distribution is not fully specified and one or more parameters need to be estimated from the data, the results will be conservative [81]. The requirement of a fully specified distribution is a serious limitation because in reality, most of the time we don't know exactly the distribution. We usually need to estimate parameters from the data. Therefore, some authors have developed the modified versions of the Kolmogorov-Smirnov test so that they can be suitable for the cases where a fully-specified distribution can not be provided. For example, Lilliefors has adapted the Kolmogorov-Smirnov test for normal distribution with unknown mean and variance in [82], and exponential distribution with unknown mean in [83], respectively. As a modification of the Kolmogorov-Smirnov test, the Anderson-Darling test [84] has been improved by Stephens to test the following distributions with unknown parameters, such as, normal, exponential, Weibull, extreme value, gamma, logistic, etc [80].

What we plan to test here is the Rice distribution with unknown parameters, which is unfortunately, to the best of our knowledge, available neither from the Anderson-Darling test and Lillierfors test nor from any other available goodness of fit tests. This is because the Rice distribution is not even a member of distributions in the location-scale family in which case the distribution of the test statistics will not depend on the true values of the unknown parameters [80]. Since the goodness of fit test is not the main purpose of this work, we decide to still use the Kolmogorov-Smirnov statistic to perform the goodness of fit test but just keep in mind that the results are conservative. For example, when the sample size is 144, the critical value 0.112 in the standard table corresponds to the 5% significance level, but if we estimate any parameters of the Rice distribution from the data, this 0.112 actually corresponds to a significance level less than 5%.

5.3 Realistic prediction of BER in SISO systems for adaptive modulation

As we have already known, a realistic prediction of BER can be achieved if the fading parameters and the average SNR are provided. The fading parameters and the average SNR can be estimated based on the MR-FDPF model. Actually, the MR-FDPF model provides us a coverage map at the pixel level as shown in Fig. 4.11. This coverage map can be partitioned into lots of rectangular local areas which contain a certain number of pixels. Then the fading parameters and the SNR can be estimated over these local areas. Each local area leads to a fading parameter and a SNR and thus a BER. Hence at the end, each of them forms a new map at the local-area level.

Here, the CITI building of INSA-Lyon is still chosen as the indoor propagation scenario simulated with the MR-FDPF model. The simulation is performed at the frequency of 3.5 GHz with the discretization step of 2 cm. The location of the Tx is inside a small office which is indicated by Tx in Fig. 5.1. The Equivalent Isotropically Radiated Power (EIRP) of the Tx is 23 dBm.

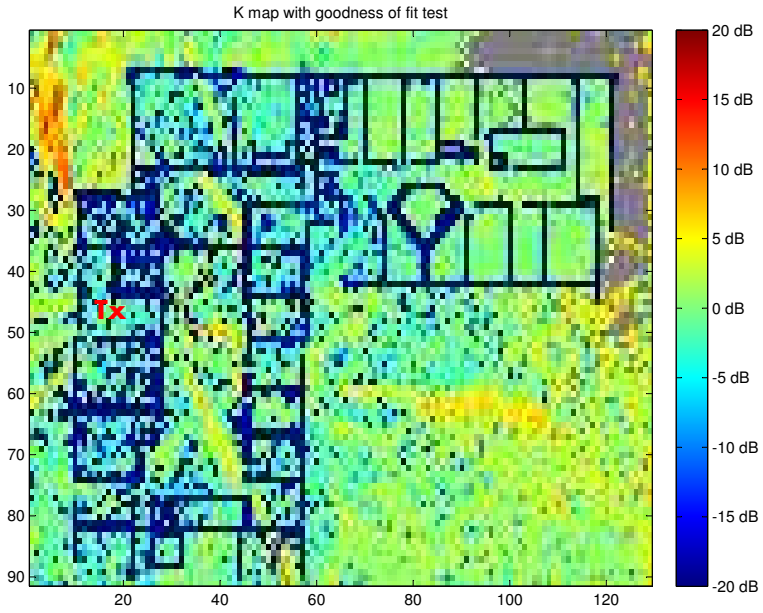

Figure 5.1: K map with goodness of fit test.

5.3.1 Rice K factor map

As discussed above, here we use the RICEFIT method to estimate the Rice K factor. In Fig. 5.1, the Rice K factor map extracted from the MR-FDPF model is shown in dB. Each K factor in Fig. 5.1 is estimated over a local area with 23×23 pixels, but only $12 \times 12 = 144$ of them taken according to an alternating pattern are used to perform the estimation since only uncorrelated samples are expected. According to [37], the uncorrelated distance of two samples is about $0.38\lambda = 3.26$ cm, and on the other hand, the distance between two pixels in the simulation is 2 cm, so each pixel will be uncorrelated with its second neighbor.

5.3.2 Performance evaluation of the estimation of the Rice K factor

In order to evaluate the performance of the estimated Rice K factor, we perform the goodness of fit test. As discussed previously, the Kolmogorov-Smirnov test is chosen and is performed at the 5% significance level although the actual significance level will be less than 5%. The grey points in Fig. 5.1 are the locations

where the estimated Rice K factor has failed the Kolmogorov-Smirnov test. It is observed that most of the failed Rice K factors are located at the top right corner and outside the building. It is suggested that this is because the envelop distribution there does not retain very strong Rice characteristics [85]. For the failed locations, we don't consider them in the following BER and modulation maps since the estimated Rice K factors there are not reliable. They will be left in grey as well.

5.3.3 Prediction of BER and AMC

It has been shown that the Rice K factor has an important impact on the capacity and performance of wireless communication systems [86]. For instance, the BER characteristics of wireless communication systems depend not only on the SNR, but also on the Rice K factor. Therefore, the prediction of BER with considering the Rice K factor will be more accurate.

In Fig. 5.2, we show the BER map for the QPSK modulation with considering the Rice K factor. The BER is calculated from the value of the Rice K factor and the SNR, considering the thermal noise over a bandwidth of 3.5 MHz. We can also show the BER maps for AWGN channels. However, because the impact of the Rice K factor on the BER is equivalent to that on modulation maps of adaptive modulation schemes, we decide to only show here the modulation maps for AWGN channels.

In order to simplify the study, we consider only the uncoded BER of 10^{-3} as the threshold to adapt the modulation schemes. The possible modulations are: BPSK, QPSK, 16QAM and 64QAM. In Fig. 5.3 and Fig. 5.4, the modulation maps are obtained under the Rice and AWGN channels, respectively. In these two figures, the numbers in the colorbar denote the modulation schemes: 1, 2, 3 and 4 denote the BPSK, QPSK, 16QAM and 64QAM, respectively, and 0 denotes none of these four modulation schemes can satisfy the target BER. From Fig. 5.3 and Fig. 5.4, we can see that modulation maps under Rice channels and AWGN channels are very different which illustrates that the widely used mean power approach can lead to a completely false prediction.

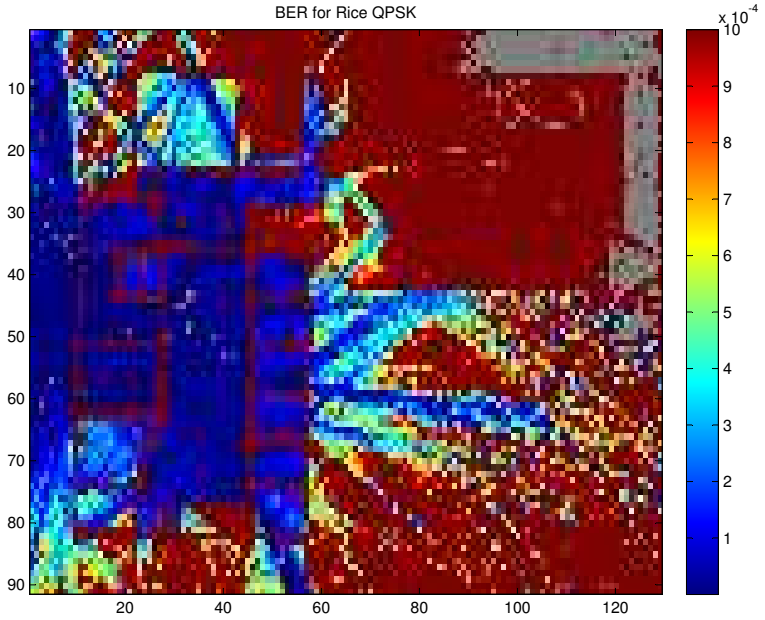

Figure 5.2: BER map for QPSK modulation under Rice channels.

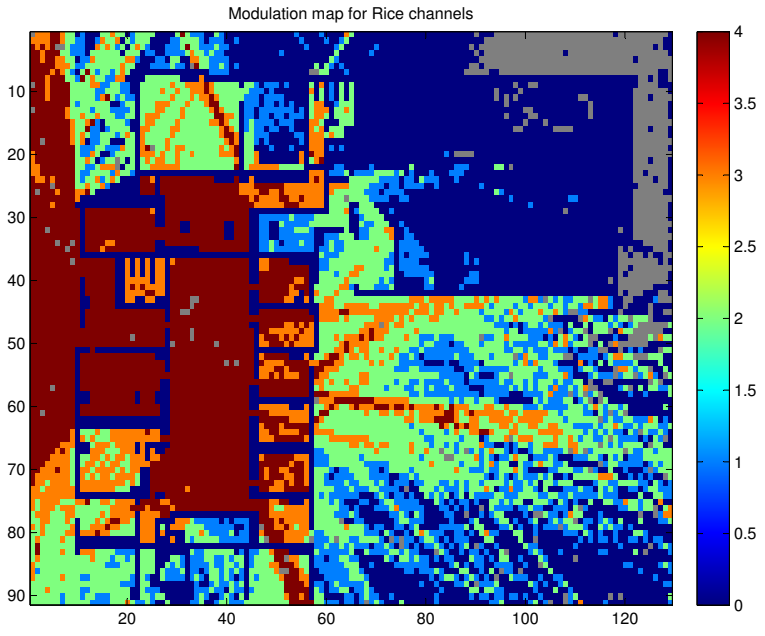

Figure 5.3: Modulation map under Rice channels.

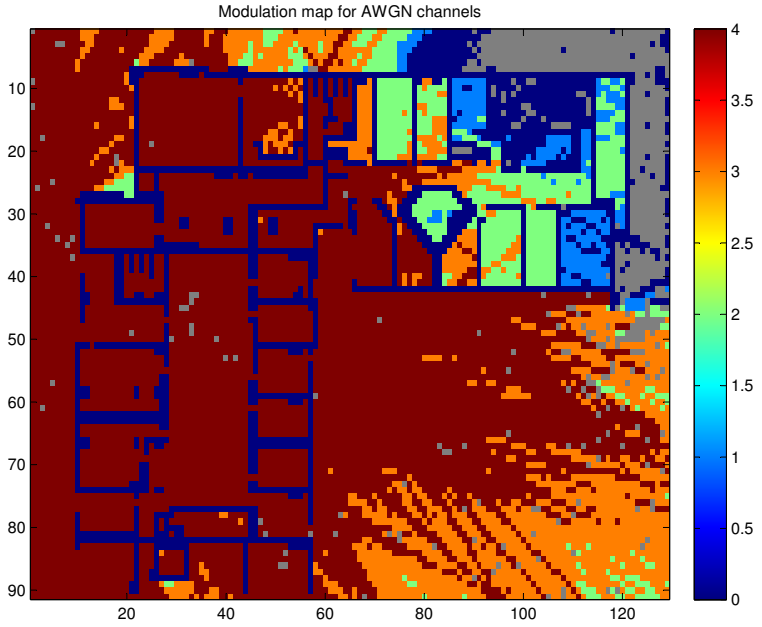

Figure 5.4: Modulation map under AWGN channels.

5.4 Realistic prediction of BER in MRC diversity systems for adaptive modulation

For the cases where the MRC diversity is used, the computation of the $P_{b:fading}(E)$ depends on the MGF of the combined SNR PDF. Since we want the BER to have a high level of accuracy, we try to make as less assumptions as possible. Thus, here we consider the diversity reception with D nonidentically distributed branches with arbitrary correlation. More specifically, we assume that the diversity branches share the same Nakagami-m fading parameter m, but they can each have their own average SNR $\bar{\gamma}_d$ $(d = 1, 2, \cdots, D)$. The envelope correlation coefficient between any channel pairs (d, d') $(d, d' = 1, 2, \cdots, D)$ is denoted by $\rho_{dd'}$. Then, the MGF of the combined SNR PDF over the Nakagami-m fading

channels is given by [87],

$$M_{\gamma}(s) = \prod_{d=1}^{D} \left(1 - \frac{s\bar{\gamma}_d}{m}\right)^{-m} \cdot \left| \begin{bmatrix} 1 & \sqrt{\rho_{12}}\left(1 - \frac{m}{s\bar{\gamma}_2}\right)^{-1} & \cdots & \sqrt{\rho_{1D}}\left(1 - \frac{m}{s\bar{\gamma}_D}\right)^{-1} \\ \sqrt{\rho_{12}}\left(1 - \frac{m}{s\bar{\gamma}_1}\right)^{-1} & 1 & \cdots & \sqrt{\rho_{2D}}\left(1 - \frac{m}{s\bar{\gamma}_D}\right)^{-1} \\ \cdot & \cdot & \cdot & \cdot \\ \cdot & \cdot & \cdot & \cdot \\ \cdot & \cdot & \cdot & \cdot \\ \sqrt{\rho_{1D}}\left(1 - \frac{m}{s\bar{\gamma}_1}\right)^{-1} & \sqrt{\rho_{2D}}\left(1 - \frac{m}{s\bar{\gamma}_2}\right)^{-1} & \cdots & 1 \end{bmatrix} \right|^{-m} \quad (5.10)$$

where $|[M]|_{D\times D}$ stands for the determinant of the $D \times D$ matrix M. Substituting the Eq. 5.10 into the Eq. 5.6 and Eq. 5.7, we can easily obtain the $P_{b:fading}(E)$ for the M-PSK and M-QAM modulations.

For the MRC diversity systems, we consider the Nakagami-m fading. Therefore, in order to compute the BER, the m parameter of the Nakagami-m fading, the average SNR for each diversity branch $\bar{\gamma}_d$ and the envelope correlation coefficient $\rho_{dd'}$ should be provided.

5.4.1 The m parameter map of the Nakagami-m fading channels

As stated in Section 5.2, there exist a number of estimation methods for the m parameter of the Nakagami-m fading, but here we adopt two methods: One is the Rice K factor mapping method since we have already estimated the Rice K factor in the previous section. The other one is the Greenwood's method since it outperforms others. The m parameter maps extracted from the MR-FDPF model by the two methods are given in dB in Fig. 5.5 and Fig. 5.6, respectively. In the two figures, each m parameter is obtained over a local area with dimensions 23×23 pixels, but only half of them taken based on an alternating pattern are chosen to implement the estimations since only uncorrelated samples are needed. The space discretization step of the MR-FDPF simulation is 2 cm.

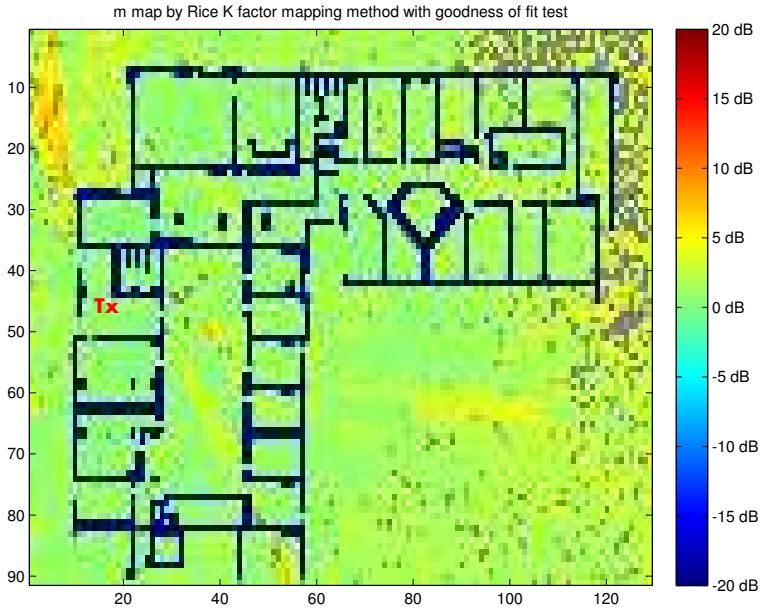

Figure 5.5: The m parameter map by the Rice K factor mapping method with goodness of fit test.

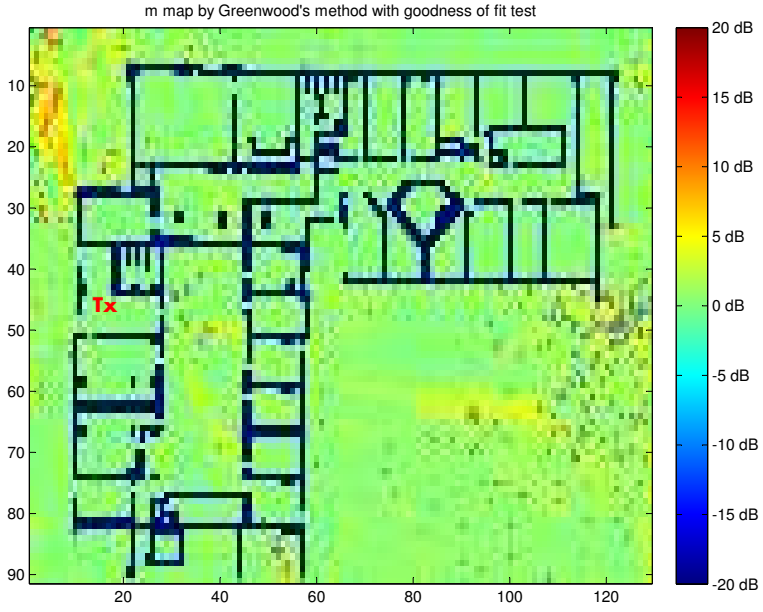

Figure 5.6: The m parameter map by the Greenwood's method with goodness of fit test.

5.4.2 Performance evaluation of the estimation of the m parameter of the Nakagami-m fading

We conduct the goodness of fit test to evaluate the estimation performance of the m parameter of the Nakagami-m fading by the two above-mentioned methods. The Kolmogorov-Smirnov test is adopted and performed at the 5% significance level. The grey points in Fig. 5.5 and Fig. 5.6 denote the locations where the estimated m parameter has failed the Kolmogorov-Smirnov test. From the Fig. 5.5, we see that most of the estimated m values by the Rice K factor mapping method have passed the Kolmogorov-Smirnov test, which validates that the RICEFIT method developed by Ridgway [74] works well in estimating the Rice K factor. Especially, the locations of the failed m values are basically in accordance with those of the failed Rice K values where the envelope distributions there are supposed to not retain very strong Rice characteristics [14]. At the end, it is observed in Fig. 5.6 that the locations of the failed m values are very few, which further proves that the Greenwood's method is among the best available methods for estimating the m parameter of the Nakagami-m fading. Therefore, here we use the Greenwood's method to estimate the m parameter for the following BER prediction.

Moreover, the mean and the variance of the estimated m parameter by the Greenwood's method is 1.2854 and 0.4778, respectively. The mean value of 1.2854 indicates that the propagation environment under investigation is a Rayleigh-like environment.

5.4.3 Prediction of BER and AMC with MRC diversity

The BER performance of the real-life diversity systems depends not only on the SNR, but also on the fading parameters and the correlations among diversity branches. Since it is possible to estimate the fading parameters and compute the correlations among diversity branches based on the MR-FDPF model, the predicted BER from the MR-FDPF model should be realistic and accurate. The correlations among branches are computed based on the signal envelope of the space samples around the corresponding antennas from the MR-FDPF model. We compute the BER for the BPSK, QPSK, 16QAM and 64QAM modulation

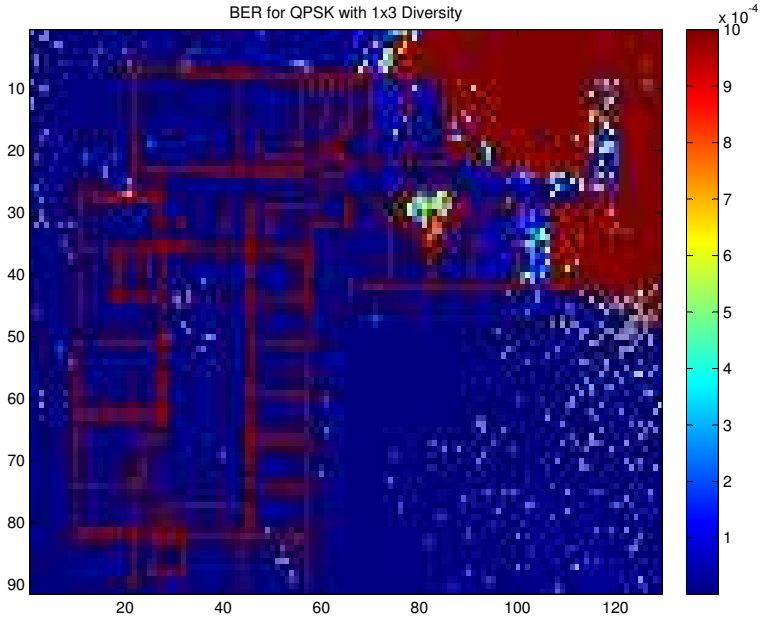

Figure 5.7: The BER map for the QPSK with 1x3 Diversity.

schemes according to Eq. 5.6 and Eq. 5.7. Here taking the QPSK modulation for example, we show the BER maps for the QPSK modulation with the 1x3 diversity, 1x2 diversity and SISO system in Fig. 5.7, Fig. 5.8 and Fig. 5.9, respectively. In these three figures, the BER is computed based on the thermal noise of 3.5 MHz bandwidth. It is observed that the BER difference between the 1x2 diversity and SISO system is larger than that between the 1x3 diversity and 1x2 diversity. This is reasonable because for diversity systems, the BER decreases negative exponentially with the number of diversity branches.

For the AMC, we consider only the target uncoded BER of 10^{-3} to adapt the modulation schemes. Fig. 5.10, Fig. 5.11 and Fig. 5.12 show the modulation maps with the 1x3 diversity, 1x2 diversity and SISO system, respectively. The numbers in the three figures: 1, 2, 3 and 4 denote the BPSK, QPSK, 16QAM and 64QAM, respectively. The number 0 denotes none of these modulation schemes above can achieve the target BER. From the Fig. 5.7 - Fig. 5.12, we can see how much the diversity can improve the system performance.

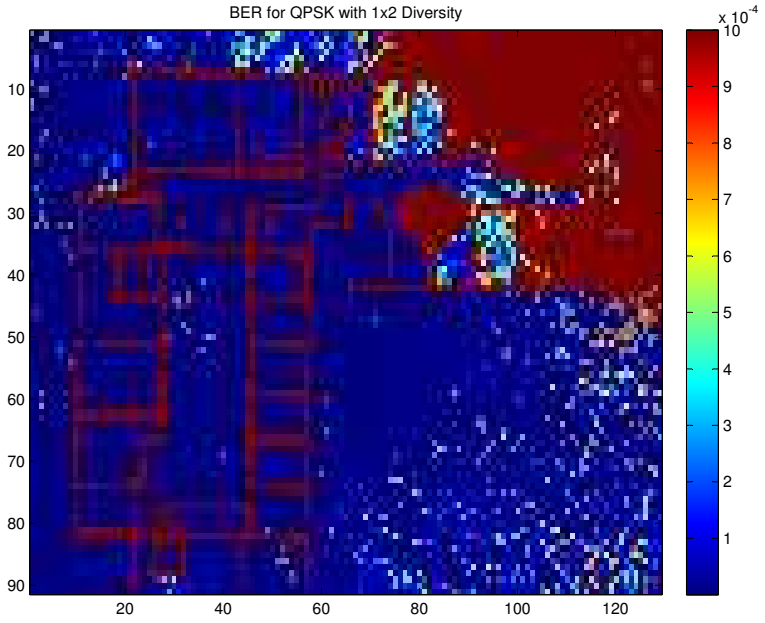

Figure 5.8: The BER map for the QPSK with 1x2 Diversity.

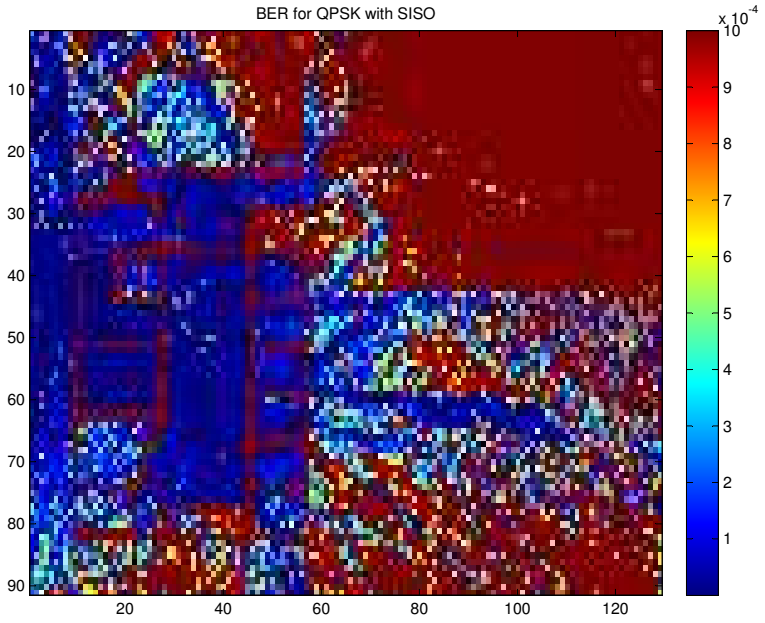

Figure 5.9: The BER map for the QPSK with SISO systems.

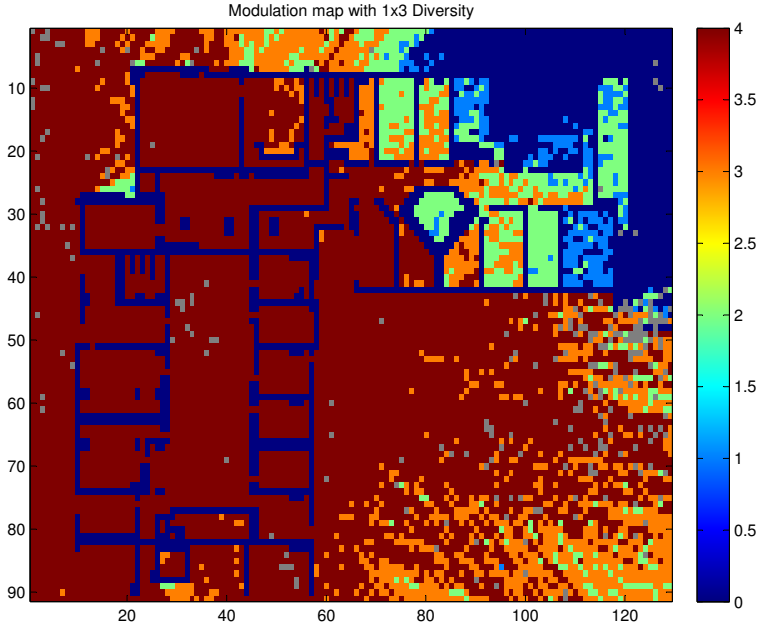

Figure 5.10: The modulation map with 1x3 diversity with the BER threshold of 10^{-3}.

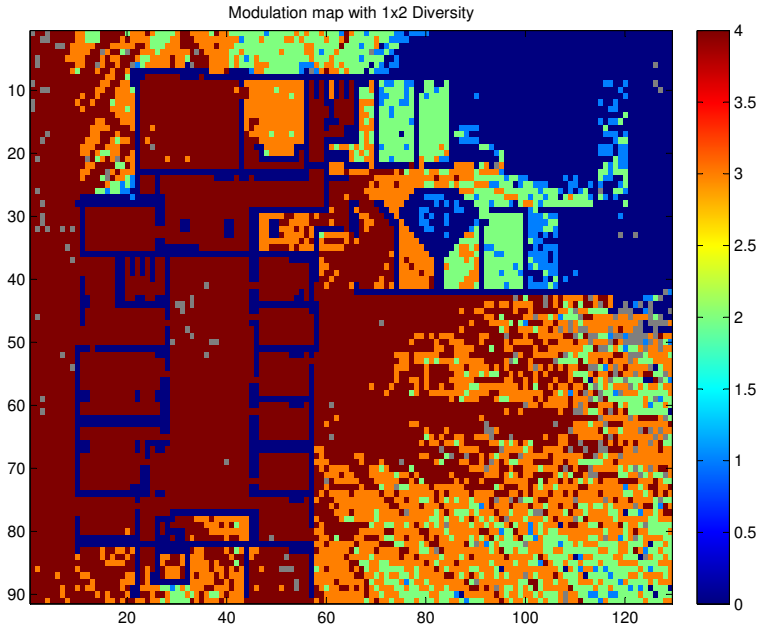

Figure 5.11: The modulation map with 1x2 diversity with the BER threshold of 10^{-3}.

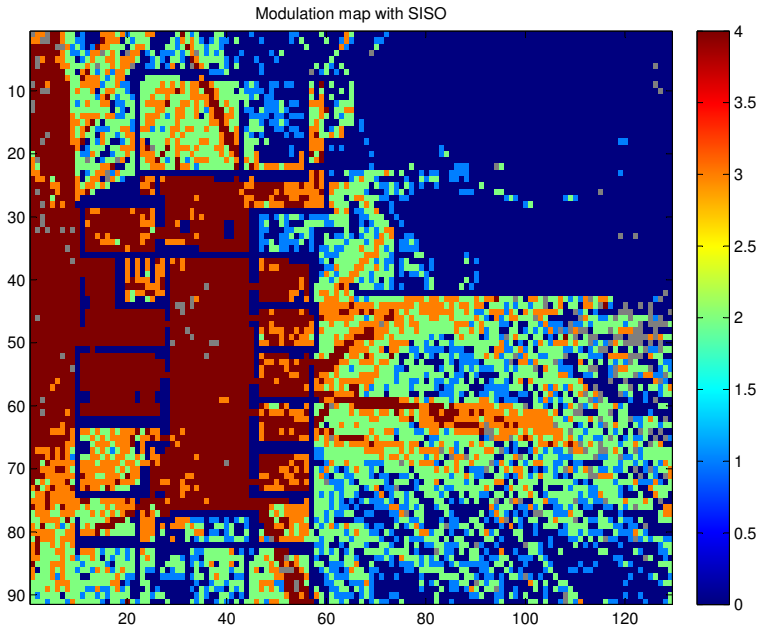

Figure 5.12: The modulation map with SISO with the BER threshold of 10^{-3}.

5.5 Chapter summary

In this chapter, we presented how a realistic BER can be predicted based on the MR-FDPF model. Actually, the BER maps for the simulated scenarios were provided. Two systems were tackled in this chapter. The first one is the SISO systems and the second one is the MRC diversity systems. For the BER of the MRC diversity systems, the correlations among diversity branches were also taken into account. The realistic prediction of the BER can be useful for many higher layer applications. And finally, the adaptive modulation was implemented based on the predicted BER for the both systems in this chapter.

Chapter 6

Wideband simulations

A great need of high data rate services has stimulated the development of the wideband wireless communications. One of the facts that the wideband wireless communications should face is that the wideband wireless channels usually suffer from the frequency selective fading. Therefore, the radio channel models which characterize large bandwidths are useful for the wideband wireless communication systems to study their performance.

This chapter starts with two wideband simulation approaches based on the MR-FDPF model. Then the wideband simulations are performed and the performance of simulating the wideband multipath fast fading is verified by comparisons with the measurements. At the end, the wideband block adaptive modulation for Orthogonal Frequency-Division Multiplexing (OFDM) systems is implemented based on the realistic prediction of the BER of each block of subcarriers.

6.1 Wideband simulation approaches

The wideband simulation can be achieved in two approaches based on the MR-FDPF model. The first approach is the straightforward repetition of the MR-FDPF model at multiple frequencies. The simulated frequency response has a high level of accuracy since it is the exact solution of Maxwell's equations at each simulated frequency sample within the bandwidth. However, this accuracy is achieved at the cost of high computational load. For instance, if the simulated

bandwidth is 50 MHz and you want to simulate N frequencies within this bandwidth, then the computational load is exactly N times of that of the narrowband simulation. The finer the frequency response, the larger the computational load.

The second approach is proposed to significantly reduce the computational load at the cost of acceptable degradation of the accuracy [88][89]. It is based on the Neumann series expansion. According to the MR-FDPF model, the field strength prediction at the frequency $v_0 \in B$ (B denotes the bandwidth) is the solution of

$$\underline{\overleftarrow{F}}(v_0) = \left(I - \underline{\tilde{\Sigma}}(v_0)\right)^{-1} \underline{\overleftarrow{S}} \tag{6.1}$$

where $\underline{\tilde{\Sigma}}(v_0) = \underline{\tilde{\Sigma}} \cdot e^{-j2\pi v_0 \Delta t}$. Similarly, the field strength prediction at the frequency $v_0 + \Delta v \in B$ is the solution of

$$\underline{\overleftarrow{F}}(v_0 + \Delta v) = \left(I - \underline{\tilde{\Sigma}}(v_0 + \Delta v)\right)^{-1} \underline{\overleftarrow{S}} \tag{6.2}$$

Note that $\underline{\tilde{\Sigma}}(v_0 + \Delta v) = e^{-j2\pi \Delta v \Delta t} \cdot \underline{\tilde{\Sigma}}(v_0)$. Thus

$$\begin{aligned}
\underline{\overleftarrow{F}}(v_0 + \Delta v) &= \left[I - \underline{\tilde{\Sigma}}(v_0) + \underline{\tilde{\Sigma}}(v_0) - e^{-j2\pi \Delta v \Delta t} \cdot \underline{\tilde{\Sigma}}(v_0)\right]^{-1} \underline{\overleftarrow{S}} \\
&= \left[\left(I - \underline{\tilde{\Sigma}}(v_0)\right)\left(I - \left(I - \underline{\tilde{\Sigma}}(v_0)\right)^{-1} \cdot \underline{\tilde{\Sigma}}(v_0) \cdot \left(e^{-j2\pi \Delta v \Delta t} - 1\right)\right)\right]^{-1} \underline{\overleftarrow{S}} \\
&= \left(I - \underline{\tilde{\Sigma}}(v_0)\right)^{-1} \cdot \left[I - \left(I - \underline{\tilde{\Sigma}}(v_0)\right)^{-1} \cdot \underline{\tilde{\Sigma}}_{\Delta v}\right]^{-1} \underline{\overleftarrow{S}} \\
&= \left[I - \left(I - \underline{\tilde{\Sigma}}(v_0)\right)^{-1} \cdot \underline{\tilde{\Sigma}}_{\Delta v}\right]^{-1} \cdot \underline{\overleftarrow{F}}(v_0)
\end{aligned} \tag{6.3}$$

where $\underline{\tilde{\Sigma}}_{\Delta v} = \underline{\tilde{\Sigma}}(v_0) \cdot \left(e^{-j2\pi \Delta v \Delta t} - 1\right)$. Using the Neumann series expansion [90], $\underline{\overleftarrow{F}}(v_0 + \Delta v)$ can be written into the form of

$$\underline{\overleftarrow{F}}(v_0 + \Delta v) = \left(\sum_{n=0}^{\infty} \left[\left(I - \underline{\tilde{\Sigma}}(v_0)\right)^{-1} \cdot \underline{\tilde{\Sigma}}_{\Delta v}\right]^n\right) \cdot \underline{\overleftarrow{F}}(v_0) \tag{6.4}$$

Thus, the N-order approximation of $\underline{\overleftarrow{F}}(v_0 + \Delta v)$ is given by

$$\underline{\overleftarrow{F}}(v_0 + \Delta v) \approx \underline{\overleftarrow{F}}(v_0) + \underline{\overleftarrow{F}}^{(1)}(\Delta v) + \cdots + \underline{\overleftarrow{F}}^{(N)}(\Delta v) \tag{6.5}$$

where

$$\underline{\overleftarrow{F}}^{(1)}(\Delta v) = \left(I - \underline{\tilde{\Sigma}}(v_0)\right)^{-1} \cdot \underline{\tilde{\Sigma}}_{\Delta v} \cdot \underline{\overleftarrow{F}}(v_0) \tag{6.6}$$

and

$$\underline{\overleftarrow{F}}^{(n+1)}(\Delta v) = \left(I - \underline{\tilde{\Sigma}}(v_0)\right)^{-1} \cdot \underline{\tilde{\Sigma}}_{\Delta v} \cdot \underline{\overleftarrow{F}}^{(n)}(v_0) \tag{6.7}$$

It is of importance to note that the similarity of Eq. 6.7 to Eq. 6.1 implies that the $(n+1)$-th order of $\underline{\overleftarrow{F}}^{(n+1)}(\Delta v)$ can be solved by the MR-FDPF model when setting the $\underline{\tilde{\Sigma}}_{\Delta v} \cdot \underline{\overleftarrow{F}}^{(n)}(v_0)$ as the source. This is very promising because it means that the upward matrix, downward matrix and inner matrix obtained in the preprocessing phase can be directly used to predict the electric field of its neighbor frequencies, otherwise, the preprocessing should be redone. Actually, the computational load of the preprocessing phase is the main computational load of the MR-FDPF model.

6.2 Wideband multipath fast fading characteristics

Radio waves can experience fast fading in the time domain, frequency domain and space domain. Here, we focus mainly on the fast fading in the frequency domain. Fig. 6.1 shows an example of the measured time frequency response of stationary channels where only the fast fading in the frequency domain is obvious. The fast fading in the time domain is minor here due to the stationary scenario, e.g. the static transmitters and receivers. The fast fading in the frequency domain can be explained by the constructive or destructive addition of multipath signals with different phases. The multipath fast fading varies with frequencies since different frequencies can lead to different arriving phases even the radio waves undergo the same paths, thus the results of the multipath addition can be different. Moreover, materials in the propagation scenarios behave differently at different frequencies. Generally speaking, multipath fast fading is very sensitive and depends highly on the scenarios.

Since the multipath fast fading is so sensitive, we believe that the MR-FDPF model is advantageous in simulating it over the well-known Ray optical models

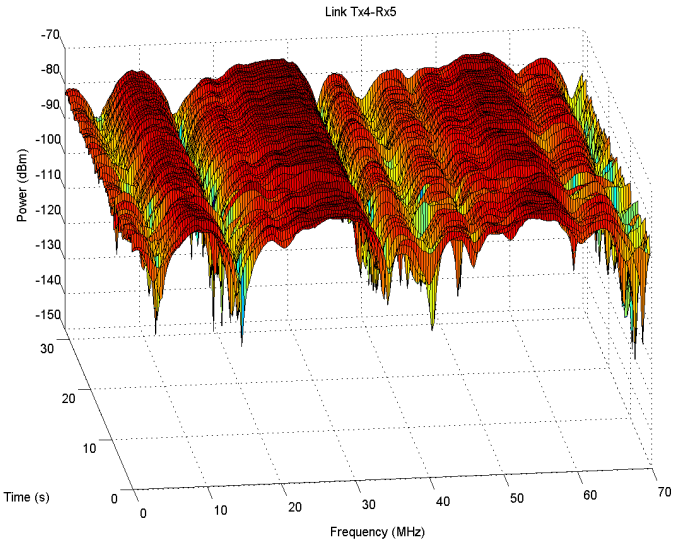

Figure 6.1: Example of measured time frequency response of stationary channels.

due to its very fine accuracy. Moreover, its requirement of using a small discretization step compared to the wavelength allows identifying very accurately all the different paths.

In order to show the ability of the MR-FDPF model in simulating the wideband multipath fast fading, the MR-FDPF simulations are performed at a whole bandwidth of 70 MHz centered at 2.45 GHz. Totally, 23 frequency bins are simulated which are evenly distributed in the bandwidth of 70 MHz. The wideband simulations here are done by the first wideband simulation approach of the MR-FDPF model described in Section 6.1 since we are more interested in the accuracy than the computational load. The scenario is the office scenario in Stanford University where 8 transmitters and 8 receivers are distributed in the office (See Fig. 4.6). The measurements which will be used to verify the simulated wideband fast fading characteristics are the "I2I stationary" scenario measurements. More details about the scenario and measurements can be found in Chapter 4.

By the wideband simulations of the MR-FDPF model, we obtain the wideband multipath fast fading characteristics. The simulated wideband fast fading results are calibrated with the measurements between the Tx1 and all the 8 Rxs at only the center frequency of 2.45 GHz, i.e. calibrated with 8 measurements. The

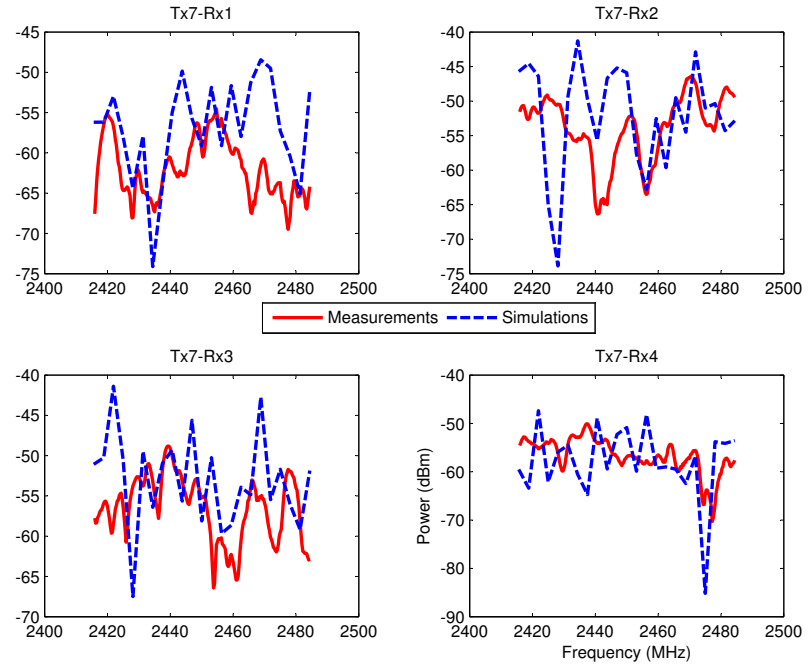

Figure 6.2: The comparisons of the wideband fast fading characteristics of the links between the Tx7 and the Rx1-4.

calibrated parameter values of materials are configured to run the MR-FDPF simulations at all the 23 frequencies. The obtained offset and RMSE compared to the measurements computed from all the $8 \times 8 = 64$ links and all the 23 frequency bins are: offset $= -30.6846$ dB; RMSE $= 8.7830$ dB;

Here, we present for example the wideband fast fading characteristics of the links between 2 transmitters (Tx7 and Tx8) and 8 receivers from the simulations and measurements in Fig. 6.2-6.5. In these figures, the receiving powers are plotted in dBm and the horizontal ordinate is the frequency covering 70 MHz centered at 2.45 GHz. The blue dash lines are the fading characteristics of the simulations and the red solid lines are those of the measurements. From these figures, we see that the wideband multipath fast fading from the simulations does not fit exactly that from the measurements. As stated above, this is due to the high sensitivity of the multipath fast fading.

In order to have a feeling of how sensitive the wideband multipath fast fading is, we investigate the fading variations by the MR-FDPF simulations when moving

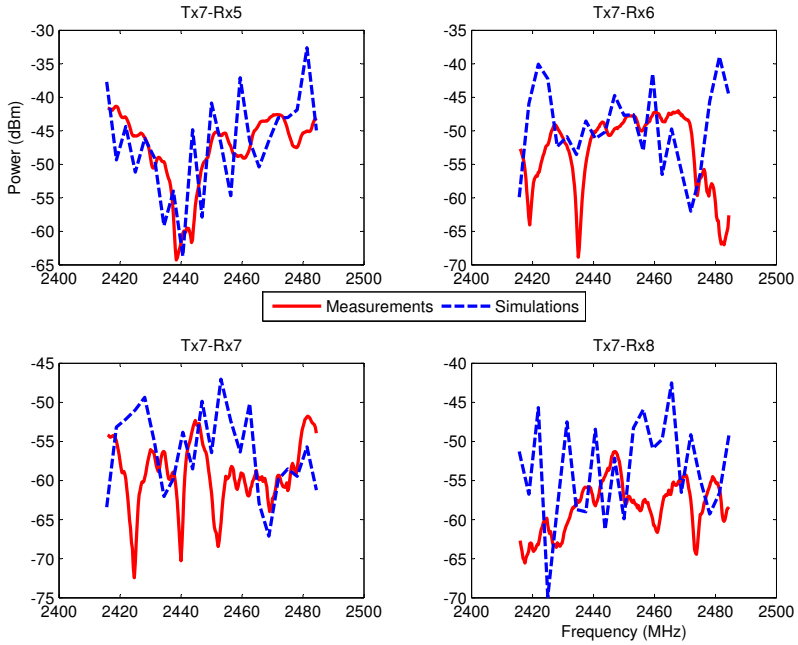

Figure 6.3: The comparisons of the wideband fast fading characteristics of the links between the Tx7 and the Rx5-8.

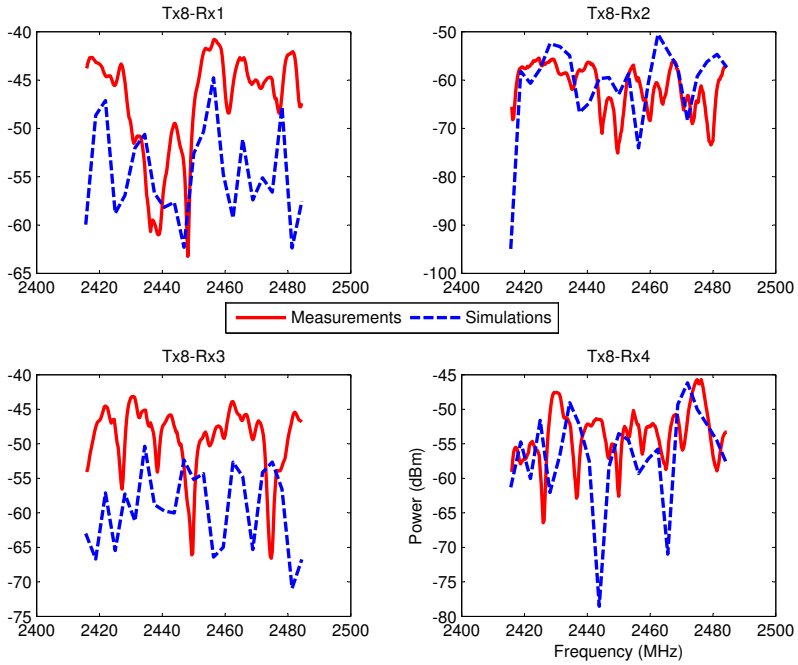

Figure 6.4: The comparisons of the wideband fast fading characteristics of the links between the Tx8 and the Rx1-4.

the Rxs with one pixel distance, i.e., 2 cm in Fig. 6.6-6.7. These two figures show that the fast fading characteristics can be very different even when moving 2 cm. Therefore, we know that the fast fading characteristics are very sensitive and it is not possible to get exactly the same fast fading characteristics at a given point with the measurements. For instance, the positions of Txs and Rxs are not known at such an accuracy level in both the simulations and measurements. And in our simulations we did not include furniture which also modifies slightly the directions and amplitudes of the different paths. Moreover, another important reason is that for the wideband multipath fast fading characteristics, the simulation results are only calibrated with 8 links at only one frequency bin, i.e. the center frequency of 2.45 GHz. That is why the wideband multipath fast fading curves from the simulations and the measurements in Fig. 6.2-6.5 fit best only at the center frequency.

Since the fast fading characteristics are so sensitive and have a high level of variations, it is very difficult to verify the fast fading characteristics obtained from the simulations by the measurements. However, in reality we are much more interested in how severe the channel fading is than how the channel fades. Therefore, the simulations and measurements are not expected to have the same fading curves, but have a comparable Fading Depth (FD).

6.2.1 Fading depth analysis

FD is an important parameter since it affects a lot the system performance. An accurate knowledge of FD is very useful for the design of reliable communication systems. It represents how severe the channel fading is. Here we define the FD as:

$$FD = \bar{P}_i - \min\left(P_i\right) \tag{6.8}$$

where P_i are the received powers in dB, $\bar{\cdot}$ and $\min\left(\cdot\right)$ denote the mean and minimum value of its variable, respectively. Here, we are mainly focusing on the FD in the frequency domain since generally the indoor radio channels do not suffer from large temporal variations.

In the table 6.1, we compare the mean FD of the total $8 \times 8 = 64$ links from the measurements and the simulations. This table shows that the mean

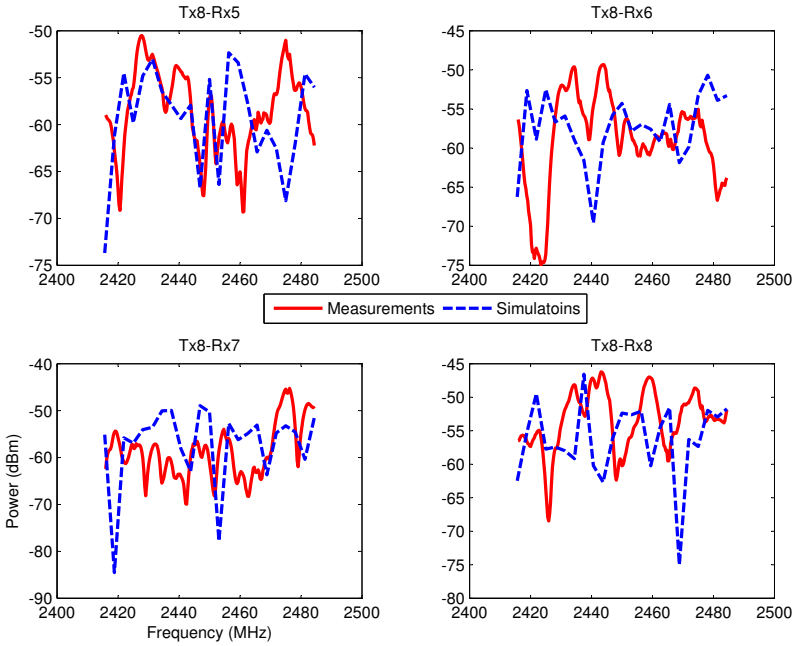

Figure 6.5: The comparisons of the wideband fast fading characteristics of the links between the Tx8 and the Rx5-8.

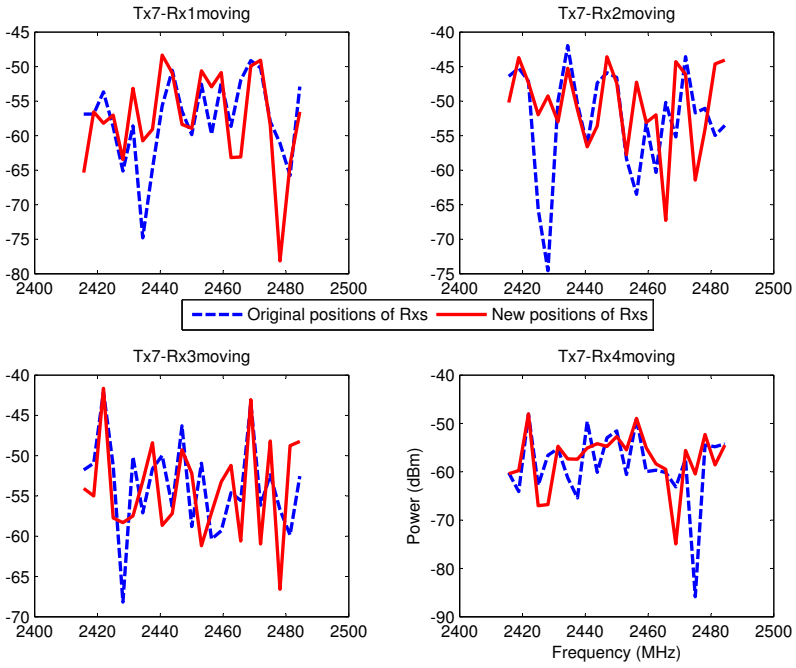

Figure 6.6: The comparisons of the wideband fast fading characteristics of the links between the Tx7 and the Rx1-4 when moving the Rxs with 2cm.

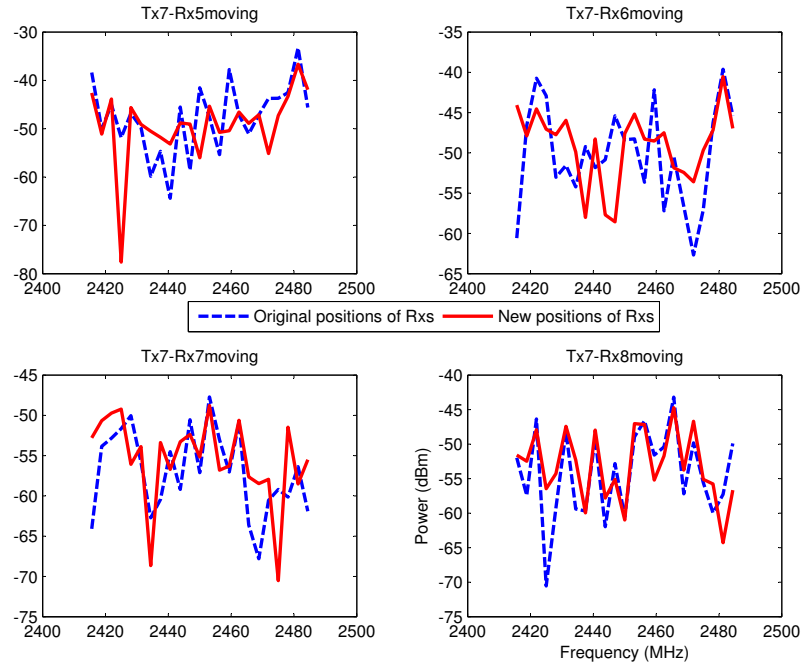

Figure 6.7: The comparisons of the wideband fast fading characteristics of the links between the Tx7 and the Rx5-8 when moving the Rxs with 2cm.

FD from the simulations are very closed to that from the measurements, which means that the MR-FDPF model is capable of simulating the wideband fast fading characteristics.

Table 6.1: Comparison of the FD from the measurements and simulations

	Measurements	**Simulations**
Mean values of the FD	12.6762	14.4655

6.3 Wideband block adaptive modulation

For the wideband wireless communications, subcarriers in the whole bandwidth under investigation can have very different SNRs and fading severities due to the wideband multipath fast fading. Therefore, in order to achieve a higher data rate, the subcarrier adaptive modulation or the block adaptive modulation techniques can be implemented for OFDM systems [91][92]. In the block adaptive

modulation technique, all the subcarriers of the OFDM systems are first divided into a number of blocks and then all the subcarriers within a block employ the same modulation scheme. In this way, the signaling overhead is reduced compared to the subcarrier adaptive modulation. The modulation scheme for each block of subcarriers is determined by the target BER. The highest order of modulation scheme which can satisfy the target BER is chosen as the modulation scheme for the block.

As we have already known, the MR-FDPF model provides a coverage map for the whole simulated area, which means that the received signal power for any position in the simulated area is known. If we consider only the thermal noise, then we can easily obtain the SNR according to

$$SNR = \frac{S}{N_0 \cdot B} \tag{6.9}$$

where S is the received signal power, N_0 is the thermal noise spectral density and B is the bandwidth. For the block adaptive modulation, the signal powers of the blocks S can be obtained from the MR-FDPF model by the wideband simulations, and the B is the bandwidth of the blocks.

As is known, not only the SNR, but also the fading parameters have a big influence on the BER [14][25] since fading parameters indicate the fading severity of wireless channels. Wireless channels with a severer fading condition have a worse BER even with the same average SNR. Thus, the prediction of BER will be accurate and realistic if we take into account the fading parameters.

Here, we model the fading as the Nakagami-m fading and thus the m parameter needs to be estimated. The estimation of the m parameter and the computation of the BER can be done as in Chapter 5.

6.3.1 The scenario and measurements

In order to verify our block adaptive modulation results from the MR-FDPF simulations, both the "I2I stationary" and the "I2I moving receivers" scenario measurements of the Stanford measurements are chosen. More details about the measurements can be found in Chapter 4 or in [61].

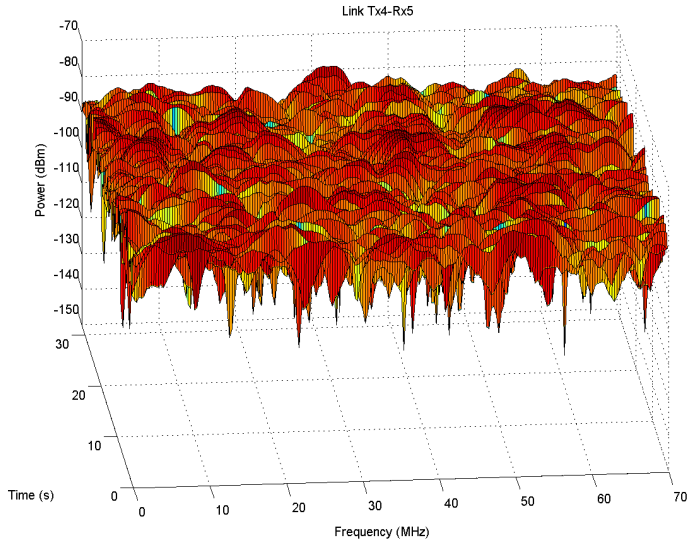

Figure 6.8: Example of measured time frequency response of moving receiver channels.

In the "I2I stationary" measurements, only minor variations over the time domain can be observed due to the stationary transmitters and receivers, and the observed large variations (up to 20 dB) over the frequency domain are due to the wideband multipath fast fading (see Fig. 6.1). However, in the "I2I moving receivers" measurements, large variations can be observed both over the time domain and frequency domain since the receivers are moving during the recording (see Fig. 6.8).

The above measurements corresponding to the two scenarios are chosen for the following purposes. The "I2I stationary" measurements are chosen for obtaining a stable frequency response characteristic (averaged over time) so that the block adaptive modulation can be implemented. The "I2I moving receivers" measurements are chosen for estimating the m parameter of the Nakagami-m fading.

Here, we only use the middle 50 MHz measurement data and consider the OFDM system with 128 subcarriers. The transmit power for each subcarrier is -30 dBm, which implies that we don't consider the adaptive power allocation.

6.3.2 Wideband multipath fast fading characteristics

The simulations of the MR-FDPF model are performed at 32 frequency bins distributed evenly within the 50 MHz bandwidth centered at 2.45 GHz. The discretization step is 2 cm. Since the OFDM system is with 128 subcarriers, each simulated frequency bin represents 4 subcarriers which are grouped as a block for the block adaptive modulation.

In Fig. 6.9, we present the wideband multipath fast fading comparison of the link Tx4-Rx5 between the MR-FDPF model and measurements as an illustration. For more results about the wideband multipath fast fading characteristics, please refer to Section 6.2. From Fig. 6.9, we observe that although the wideband multipath fast fading characteristics from the MR-FDPF model and the measurements do not fit each other exactly, they show a comparable fading depth.

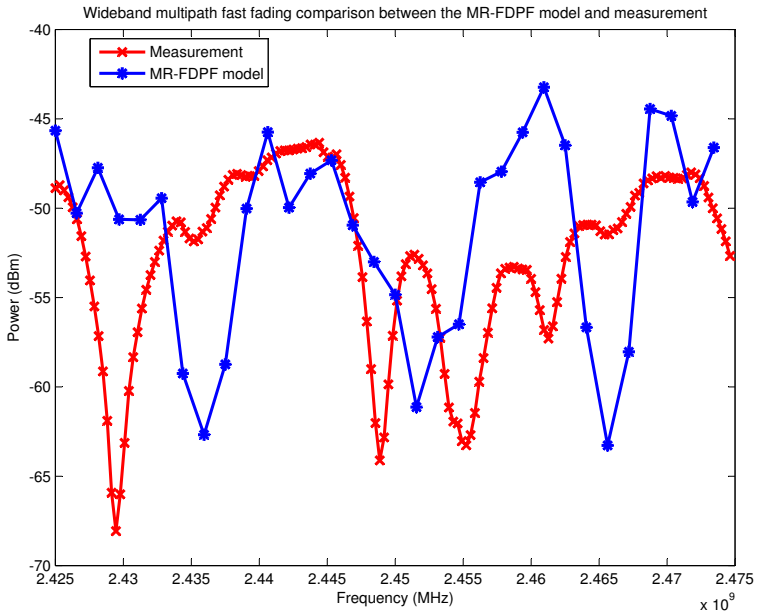

Figure 6.9: Wideband multipath fast fading comparison of the link Tx4-Rx5 between the MR-FDPF model and measurement.

6.3.3 Realistic prediction of BER and block adaptive modulation for OFDM systems

For the MR-FDPF model, the average SNR for each of the 32 subcarrier blocks is computed according to Eq. 6.9. The m parameter of the Nakagami-m fading is estimated over a 23 x 23 pixel square area according to Eq. 5.9. For the measurements, the average SNR for each of the 32 subcarrier blocks is computed from the averaged frequency response of the "I2I stationary" measurements. The m parameter is estimated from the 120 time slots data of the "I2I moving receivers" measurements at each of these 32 frequency bins.

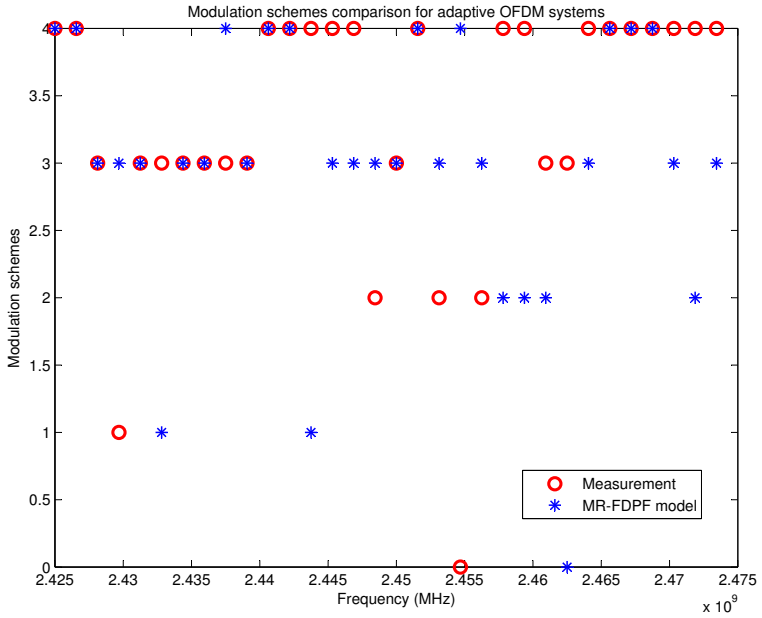

Figure 6.10: Modulation schemes for adaptive OFDM systems.

The predicted BER is used to determine the modulation scheme of each block of subcarriers at the threshold of 10^{-3}. Totally, four modulation schemes: BPSK, QPSK, 16QAM and 64QAM are chosen to perform the block adaptive modulation technique. Fig. 6.10 shows the modulation schemes of the block adaptive modulation from both the MR-FDPF model and measurements. In Fig. 6.10, the numbers: 1, 2, 3, 4 denote the BPSK, QPSK, 16QAM, 64QAM modulation schemes, respectively, and 0 denotes none of the four modulations can satisfy the target BER.

Table 6.2: Comparison of the average aggregate data rate and data rate gain

	MR-FDPF model	**Measurements**
Average aggregate data rate 1	173.66 Mbps	146.00 Mbps
Average aggregate data rate 2	127.34 Mbps	108.69 Mbps
Average data rate gain	1.42	1.40

6.3.4 Average aggregate date rate and data rate gain of block adaptive modulation

Another way to check whether the MR-FDPF model and the measurements fit each other statistically is to compute the average aggregate data rate per link from the block adaptive modulation and the average data rate gain of the block adaptive modulation over the non-adaptive modulation. There are 8 transmitters and 8 receivers, i.e. $8 \times 8 = 64$ links, so the average aggregate data rate per link is computed by the total aggregate data rate of the 64 links divided by 64.

The aggregate data rate is computed according to [92]

$$R = \frac{Number\ of\ bits\ per\ OFDM\ symbol}{Time\ duration\ of\ OFDM\ symbol} \tag{6.10}$$

The data rate gain is defined as [92]

$$Gain = \frac{Data\ rate\ from\ adaptive\ modulation}{Data\ rate\ from\ nonadaptive\ modulation} \tag{6.11}$$

Here, we use the maximum data rate from the BPSK, QPSK, 16QAM 64QAM non-adaptive modulations as the data rate from non-adaptive modulation to compute the data rate gain in Eq. 6.11. Therefore, the obtained data rate gain is conservative compared to practical systems since we use the maximum data rate as the data rate from non-adaptive modulation.

Table. 6.2 gives the obtained average aggregate data rate per link from the block adaptive modulation, i.e., average aggregate data rate 1 and that from the non-adaptive modulation, i.e., average aggregate data rate 2 and the average data rate gain from the MR-FDPF model and that from the measurements. From Table. 6.2, we can see that the MR-FDPF model and the measurements fit each other statistically very well.

6.4 Chapter summary

This chapter first presented two approaches of the wideband simulations based on the MR-FDPF model. The first approach was the straightforward repetition of the MR-FDPF simulations at multiple frequencies. The second approach was an approximation one based on the Neumann series expansion. For this chapter, the first approach was finally chosen as the wideband simulation approach since we were more interested in the accuracy than the computational load here. The simulated wideband multipath fast fading characteristics by the MR-FDPF model were compared to those from the measurements and they fitted each other statistically. Finally, the simulated wideband multipath fast fading characteristics were used to implement the block adaptive modulation scheme for OFDM systems. The obtained average aggregate data rate and the data rate gain from the block adaptive modulation were verified by the measurements.

Chapter 7

Conclusion and perspectives

7.1 Conclusion

In radio propagation models, deterministic ones usually possess a high level of accuracy since they take the specific propagation environments into account. However, in reality, radio channels are a kind of random processes due to e.g. the moving people or moving objects around. Thus, realistic radio channels can not be completely determined by purely deterministic models. Based on the deterministic MR-FDPF model, this thesis proposed a semi-deterministic model which introduced a stochastic part to take into account the random aspect of the realistic radio channels. Besides, many radio propagation simulators provide only the mean power prediction, but it has been shown that fading has also an important impact on the system performance. Hence, the fading information was extracted based on the MR-FDPF model and then an accurate prediction of the BER was achieved. The prediction of the BER has been tackled for three systems: the SISO systems, the MRC diversity systems and the wideband OFDM systems. Finally, the predicted BER has been used to implement the adaptive modulation scheme.

This thesis started with the background and the state-of-the-art survey of indoor radio propagation models in Chapter 2. And then in Chapter 3, the characterization of deterministic channels and randomly time-variant linear channels were provided. Randomly time-variant linear channels are introduced to take the randomness of the realistic channels into account. In order to simplify the

analysis, the assumption of the WSSUS is made and then the autocorrelation functions of the system functions are simplified to the P-functions which depend only on two variables. Moreover, a number of parameters for radio link quality were also described which were used in the latter chapters.

The main purpose of Chapter 4 was to extract the large scale propagation characteristics and the small scale fading statistics based on the MR-FDPF model. Hence, the principle of the MR-FDPF model was provided first, followed by the model calibration and the accuracy analysis. The reason why we wanted to separate the large scale propagation characteristics and the small scale fading was that we believe although the final effects of the realistic radio channels are random, there is still something deterministic inside. We consider the mean path loss to be deterministic, but the shadow fading and the small scale fading to be random. Thus, the mean path loss can be described deterministically, but the shadow fading and the small scale fading should be described statistically. In this way, a semi-deterministic model was finally proposed based on the deterministic MR-FDPF model which took the randomness of the realistic radio channels into account.

Chapter 5 was about the realistic prediction of the BER and the adaptive modulation scheme. As is known, the BER depends not only on the mean power, but also on the fading severity, even also on the correlations among diversity branches for diversity systems. Thus, this chapter first introduced the theoretical results of the BER which was based on well-known MGF. Then the estimation of the fading parameters were discussed for the Rice and the Nakagami-m fading channels. The Kolmogorov-Smirnov goodness of fit test was performed to verify the performance of the estimations. The BER was predicted for two systems: the SISO systems and the MRC diversity systems. With the realistic prediction of the BER, the adaptive modulation scheme was finally implemented.

The wideband simulations were presented in Chapter 6. Two wideband simulation approaches based on the MR-FDPF model were given in the first part of this chapter. Then the wideband multipath fast fading characteristics were obtained by the wideband simulations of the MR-FDPF model and they were verified by comparisons to the measurements. In the last part of this chapter, the

realistic BER was predicted for the wideband OFDM systems based on the simulated wideband multipath fast fading characteristics and thus the block adaptive modulation was implemented. The obtained average aggregate data rate and the data rate gain were verified by the measurements

7.2 Perspectives

Although the work in this thesis improves the MR-FDPF model from several aspects above, there are still some interesting research directions which are worth exploring:

1. Since we have already predicted a realistic BER and implemented the adaptive modulation scheme for the SISO systems, the MRC diversity systems and the wideband OFDM systems, it can be really interesting to do so for the Multiple-Input Single-Output (MISO) and MIMO systems. For the simulations of the mulitple-input systems, it is easy and convenient for the MR-FDPF model because the antenna array has already been implemented in the MR-FDPF model to synthesize the particular radiation patterns [93].

2. The results in Chapter 5 have not been verified by the measurements although the estimation performance of the fading parameters has been verified by the goodness of fit test. Thus, it is worth performing some measurements and processing the measurement data to verify the predicted BER and adaptive modulation scheme for both the SISO and the MRC diversity systems.

3. In chapter 4, we analyzed the accuracy of the MR-FDPF model. For instance, for a calibrated MR-FDPF simulation result, we can obtain the RMSE when compare the simulation to the measurement. This RMSE can be considered as the error introduced by the MR-FDPF model due to e.g. the inaccurate modeling of the simulated scenarios. This error can be modeled to follow a certain kind of distributions, e.g. the Gaussian distribution, and then the confidence interval can be computed. This idea can be applied to the prediction of both the path loss and the BER.

4. Since a modulation map can already be provided for the simulated scenarios by our previous work, a throughput can be predicted for the wireless systems.

For instance, mobile users can be first allocated randomly in the simulated scenario, and then choose a certain kind of the Media Access Control (MAC) layer protocols. Finally, the throughput for the systems can be computed.

References

[1] S.-P. Yeh, S. Talwar, G. Wu, N. Himayat, and K. Johnsson. Capacity and coverage enhancement in heterogeneous networks. *IEEE Wireless Communications*, 18(3):32–38, 2011. 1

[2] R. Jain, S. Katiyar, and N. Agrawal. Hierarchical cellular structures in high-capacity cellular communication systems. *(IJACSA) International Journal of Advanced Computer Science and Applications*, 2(9):52 –57, 2011. 1

[3] J. Zhang and G. de la Roche. *Femtocells: technologies and deployment*. Wiley Online Library, 2010. 2

[4] T.S. Rappaport. *Wireless communications: principles and practice*. Prentice Hall PTR New Jersey, 1996. 2, 4, 13, 17, 63

[5] H. Hashemi. The indoor radio propagation channel. *Proceedings of the IEEE*, 81(7):943 –968, July 1993. 4

[6] J.-M. Gorce, K. Jaffres-Runser, and G. de la Roche. Deterministic approach for fast simulations of indoor radio wave propagation. *IEEE Transactions on Antennas and Propagation*, 55(3):938 –948, 2007. 6, 26, 46

[7] K. Runser and J.-M. Gorce. Assessment of a new indoor propagation prediction method based on a multi-resolution algorithm. In *61st IEEE Vehicular Technology Conference*, Stockholm, Sweden, May 2005. 6, 26

[8] G. de la Roche, K. Jaffres-Runser, and J-M. Gorce. On predicting in-building wifi coverage with a fast discrete approach. *International Journal of Mobile Network Design and Innovation*, 2(1):3–12, 2007. 6, 55

[9] P.O. Luthi. *Lattice Wave Automata: from radio wave to fracture propagation.* PhD thesis, Computer Science Department, University of Geneva, 24 rue General-Dufour, 1211 Geneva 4, Switzerland, 1998. 6, 25, 27, 70

[10] B. Chopard, P. Luthi, and J.-F. Wagen. Multi-cell coverage predictions: a massively parallel approach based on the parflow method. In *The Ninth IEEE International Symposium on Personal, Indoor and Mobile Radio Communications*, volume 1, pages 60 –64, 1998. 6

[11] C. Balanis. *Advanced Engineering Electromagnetics.* John Wiley & Sons, New York, NY, USA, 1999. 6, 13

[12] M. Luo, N. Lebedev, G. Villemaud, G. De La Roche, J. Zhang, and J.M. Gorce. On predicting large scale fading characteristics with the MR-FDPF method. In *6th European Conference on Antennas and Propagation (EUCAP)*, Prague, Czech Republic, March 2012. 8

[13] M. Luo, D. Umansky, G. Villemaud, M. Lafort, and J.-M. Gorce. Estimating channel fading statistics based on radio wave propagation predicted with deterministic MR-FDPF method. In *5th European Conference on Antennas and Propagation (EuCAP 2011)*, Rome, Italy, April 2011. 8

[14] M. Luo, G. Villemaud, J. Gorce, and J. Zhang. Realistic prediction of BER and AMC for indoor wireless transmissions. *IEEE Antennas and Wireless Propagation Letters*, 11:1084 – 1087, 2012. 8, 93, 108

[15] M. Luo, G. Villemaud, J.Weng, J.-M. Gorce, and J. Zhang. Realistic prediction of ber and amc woth mrc diversity for indoor wireless transmissions,. In *IEEE Wireless Communications and Networking Conference (WCNC 2013), Shanghai, China, April*, 2013. 8

[16] M. Luo, G. De La Roche, G. Villemaud, J.M. Gorce, D. Umansky, and J. Zhang. Simulation of wide band multipath fast fading based on finite difference method. In *IEEE Vehicular Technology Conference*, San Francisco, United States, September 2011. 8

[17] M. Luo, G. Villemaud, J.-M. Gorce, and J. Zhang. Realistic prediction of ber for adaptive ofdm systems. In *7th European Conference on Antennas and Propagation (EuCAP 2013)*, Gothenburg, Sweden, April 2013. 8

[18] S.R. Saunders and A. Aragón-Zavala. *Antennas and propagation for wireless communication systems*. Wiley, 2007. 11, 13, 15, 16, 65

[19] C. Huygens and M. Blay. *Traité de la lumiere*. Gauthier-Villars, 1920. 13

[20] J. Keller. *A geometrical theory of diffraction*. Courant Institute of Mathematical Sciences, New York University, 1958. 13

[21] R. Kouyoumjian and P. Pathak. A uniform geometrical theory of diffraction for an edge in a perfectly conducting surface. *Proceedings of the IEEE*, 62(11):1448–1461, 1974. 13

[22] P. Pajusco. Propagation channel models for mobile communication. *Comptes Rendus Physique*, 7(7):703–714, 2006. 13, 28

[23] A.F. Molisch. *Wireless communications*. John Wiley & Sons, New York, NY, USA, 2011. 13, 14, 31, 33, 37, 63

[24] COST Action. *Digital Mobile Radio Towards Future Generation Systems: Final Report*. Directorate General Telecommunications, Information Society, Information Market, and Exploitation Research, 1999. 13, 15, 16, 17

[25] M.K. Simon and M.S. Alouini. *Digital communication over fading channels*, volume 86. Wiley-IEEE Press, 2004. 13, 17, 19, 39, 40, 41, 82, 108

[26] Z. Ren, G. Wang, Q. Chen, and H. Li. Modelling and simulation of rayleigh fading, path loss, and shadowing fading for wireless mobile networks. *Simulation Modelling Practice and Theory*, 19(2):626–637, 2011. 15

[27] S. Seidel and T. Rappaport. 914 MHz path loss prediction models for indoor wireless communications in multifloored buildings. *IEEE Transactions on Antennas and Propagation*, 40(2):207–217, 1992. 15

[28] M. Panjwani, A. Abbott, and T. Rappaport. Interactive computation of coverage regions for wireless communication in multifloored indoor environments. *IEEE Journal on Selected Areas in Communications*, 14(3):420–430, 1996. 15

[29] K. Cheung, J. Sau, and R. Murch. A new empirical model for indoor propagation prediction. *IEEE Transactions on Vehicular Technology*, 47(3):996–1001, 1998. 15

[30] M. Lott and I. Forkel. A multi-wall-and-floor model for indoor radio propagation. In *IEEE 53rd Vehicular Technology Conference*, Rhodes, Greece, May 2001. 15, 16

[31] J. Keenan and A. Motley. Radio coverage in buildings. *British Telecom Technology Journal*, 8(1):19–24, 1990. 15, 16

[32] G. Wolfle, P. Wertz, and F. Landstorfer. Performance, accuracy and generalization capability of indoor propagation models in different types of buildings. In *10th IEEE International Symposium on Personal, Indoor and Mobile Radio Communications*, 1999. 16, 27

[33] P. Karlsson. *Indoor radio propagation for personal communications services.* PhD thesis, Lund Institute of Technology, 1995. 17

[34] M. Nakagami. The m-distribution-A general formula of intensity distribution of rapid fading. *Statistical Method of Radio Propagation*, 1960. 18

[35] A. Sheikh, M. Abdi, and M. Handforth. Indoor mobile radio channel at 946 MHz: Measurements and modeling. In *43rd IEEE Vehicular Technology Conference*, Secaucus, NJ, USA, 1993. 19

[36] A. Goldsmith. *Wireless communications.* Cambridge university press, 2005. 19

[37] J.D. Parsons. *The mobile radio propagation channel*, volume 81. Wiley Online Library, 2000. 19, 20, 21, 33, 65, 66, 87

[38] M. Lawton and J. McGeehan. The application of a deterministic ray launching algorithm for the prediction of radio channel characteristics in small-cell environments. *IEEE Transactions on Vehicular Technology*, 43(4):955–969, 1994. 20

[39] K. Yee. Numerical solution of initial boundary value problems involving maxwell's equations in isotropic media. *IEEE Transactions on Antennas and Propagation*, 14(3):302–307, 1966. 22

[40] A. Taflove. Application of the finite-difference time-domain method to sinusoidal steady-state electromagnetic-penetration problems. *IEEE Transactions on Electromagnetic Compatibility*, (3):191–202, 1980. 22, 23

[41] P. Pagani, F. Talom, P. Pajusco, and B. Uguen. *Ultra Wide Band Radio Propagation Channel*. Wiley-ISTE, 2010. 22, 33

[42] A. Rial. *Applying the finite-difference time-domain to the modelling of large-scale radio channels*. PhD thesis, University of Bedfordshire, 2010. 22

[43] J. Maxwell. Xxv. on physical lines of force. *The London, Edinburgh, and Dublin Philosophical Magazine and Journal of Science*, 21(139):161–175, 1861. 22

[44] A. Taflove and M. Brodwin. Numerical solution of steady-state electromagnetic scattering problems using the time-dependent maxwell's equations. *IEEE Transactions on Microwave Theory and Techniques*, 23(8):623–630, 1975. 23

[45] A. Taflove and S. Hagness. *Computational electrodynamics*, volume 160. Artech house BostonLondon, 2000. 23

[46] B. Chopard, P.O. Luthi, and J.-F. Wagen. Lattice boltzmann method for wave propagation in urban microcells. *IEE Proceedings - Microwaves, Antennas and Propagation*, 144(4):251 –255, August 1997. 24, 27

[47] B. Chopard and M. Droz. *Cellular automata modeling of physical systems*. Cambridge University Press, 1998. 24

[48] G Wölfle and F. Landstorfer. Dominant paths for the field strength prediction. In *48th IEEE Vehicular Technology Conference*, Ottawa, Canada, May 1998. 27, 28

[49] G. Wölfle, R. Wahl, P. Wertz, P. Wildbolz, and F. Landstorfer. Dominant path prediction model for indoor scenarios. In *German Microwave Conference (GeMIC)*, 2005. 27

[50] G. Wolfle, P. Wertz, and F. Landstorfer. Performance, accuracy and generalization capability of indoor propagation models in different types of buildings. In *10th IEEE International Symposium on Personal, Indoor and Mobile Radio Communications*, 1999. 27

[51] P. Pechac and M. Klepal. Effective indoor propagation predictions. In *54th IEEE Vehicular Technology Conference*, Atlantic, USA, 2001. 28

[52] L. Subrt and P. Pechac. Semi-deterministic propagation model for subterranean galleries and tunnels. *IEEE Transactions on Antennas and Propagation*, 58(11):3701–3706, 2010. 28

[53] M. Klepal. *Novel approach to indoor electromagnetic wave propagation modelling*. PhD thesis, 2003. 28

[54] S. Primak and V. Kontorovich. *Wireless multi-antenna channels: modeling and simulation*, volume 28. Wiley, 2011. 28

[55] A.F. Molisch, H. Asplund, R. Heddergott, M. Steinbauer, and T. Zwick. The COST259 directional channel model-part I: Overview and methodology. *IEEE Transactions on Wireless Communications*, 5(12):3421–3433, 2006. 28

[56] M. Döttling, W. Mohr, and A. Osseiran. *Radio Technologies and Concepts for IMT-Advanced*. Wiley, 2009. 28

[57] G.D. Durgin. *Theory of stochastic local area channel modeling for wireless communications*. PhD thesis, Citeseer, 2000. 39, 70

[58] J.M. Gorce, K. Jaffrès-Runser, and G. De La Roche. The adaptive multi-resolution frequency-domain parflow MR-FDPF method for indoor radio wave propagation simulation. Part I: Theory and algorithms. 2005. 46

[59] D.R. Jones, C.D. Perttunen, and B.E. Stuckman. Lipschitzian optimization without the lipschitz constant. *Journal of Optimization Theory and Applications*, 79(1):157–181, 1993. 56

[60] K. Jaffrès-Runser, G. De La Roche, Villemaun G., and J.M. and Gorce. The adaptive multi-resolution frequency-domain parflow MR-FDPF method for indoor radio wave propagation simulation. Part II: Calibration and experimental assessment. Technical report, 2005. 56

[61] N. Czink, B. Bandemer, G. Vazquez-Vilar, A. Paulraj, and L. Jalloul. July 2008 radio measurement campaign: Measurement documentation. Technical report, Stanford University, Smart Antennas Research Group, July 2008. 56, 64, 108

[62] Rusk medav channel sounders. [Online]. Available: http://www.channelsounder.de, 2008. 57

[63] B.H. Fleury, M. Tschudin, R. Heddergott, D. Dahlhaus, and K. Ingeman Pedersen. Channel parameter estimation in mobile radio environments using the sage algorithm. *Selected Areas in Communications, IEEE Journal on*, 17(3):434 –450, March 1999. 71

[64] G.D. Durgin. *Space-time wireless channels*. Prentice Hall, 2003. 71

[65] J. Lu, K. Letaief, J. Chuang, and M. Liou. M-PSK and M-QAM BER computation using signal-space concepts. *IEEE Transactions on Communications*, 47(2):181–184, 1999. 83

[66] P. Lee. Computation of the bit error rate of coherent m-ary psk with gray code bit mapping. *IEEE Transactions on Communications*, 34(5):488–491, 1986. 83

[67] J. Lassing, E.G. Strom, E. Agrell, and T. Ottosson. Computation of the exact bit-error rate of coherent m-ary psk with gray code bit mapping. *IEEE Transactions on Communications*, 51(11):1758–1760, 2003. 83

[68] D. Yoon, K. Cho, and J. Lee. Bit error probability of m-ary quadrature amplitude modulation. In *52nd IEEE Vehicular Technology Conference*, USA, 2000. 83

[69] K. Cho and D. Yoon. On the general BER expression of one-and two-dimensional amplitude modulations. *IEEE Transactions on Communications*, 50(7):1074–1080, 2002. 83

[70] A. Abdi, C. Tepedelenlioglu, M. Kaveh, and G. Giannakis. On the estimation of the K parameter for the rice fading distribution. *IEEE Communications Letters*, 5(3):92 –94, March 2001. 84

[71] J. Sijbers, A.J. Den Dekker, P. Scheunders, and D. Van Dyck. Maximum-likelihood estimation of rician distribution parameters. *IEEE Transactions on Medical Imaging*, 17(3):357–361, 1998. 84

[72] C.F.M. Carobbi and M. Cati. The absolute maximum of the likelihood function of the rice distribution: Existence and uniqueness. *IEEE Transactions on Instrumentation and Measurement*, 57(4):682–689, 2008. 84

[73] L.J. Greenstein, S.S. Ghassemzadeh, V. Erceg, and D.G. Michelson. Ricean k-factors in narrow-band fixed wireless channels: Theory, experiments, and statistical models. *IEEE Transactions on Vehicular Technology*, 58(8):4000–4012, 2009. 84

[74] G. Ridgway. RICEFIT. [Online] http://www.mathworks.com/matlabcentral/fileexchange/14237-ricerician-distribution/content/rician/ricefit.m, 2008. 84, 93

[75] A. Abdi and M. Kaveh. Performance comparison of three different estimators for the nakagami m parameter using monte carlo simulation. *IEEE Communications Letters*, 4(4):119–121, 2000. 84

[76] Q. Zhang. A note on the estimation of nakagami-m fading parameter. *IEEE Communications Letters*, 6(6):237–238, 2002. 84, 85

[77] H.C.S. Thom. A note on the gamma distribution. *Monthly Weather Review*, 86(4):117–122, 1958. 84

[78] J.A. Greenwood and D. Durand. Aids for fitting the gamma distribution by maximum likelihood. *Technometrics*, 2(1):55–65, 1960. 84, 85

[79] K. Bownan and L. Shenton. Properties of estimators for the gamma distribution. *History and Philosophy of Logic*, 11(4):377–519, 1982. 84

[80] R.B. D'Agostino and M.A. Stephens. *Goodness-of-fit techniques*, volume 68. Marcel Dekker, New York, 1986. 85, 86

[81] F.J. Massey Jr. The kolmogorov-smirnov test for goodness of fit. *Journal of the American Statistical Association*, 46(253):68–78, 1951. 85

[82] H.W. Lilliefors. On the kolmogorov-smirnov test for normality with mean and variance unknown. *Journal of the American Statistical Association*, 62(318):399–402, 1967. 85

[83] H.W. Lilliefors. On the kolmogorov-smirnov test for the exponential distribution with mean unknown. *Journal of the American Statistical Association*, 64(325):387–389, 1969. 85

[84] T. Anderson and D.A. Darling. A test of goodness of fit. *Journal of the American Statistical Association*, 49(268):765–769, 1954. 85

[85] S. Wyne, T. Santos, F. Tufvesson, and AF Molisch. Channel measurements of an indoor office scenario for wireless sensor applications. In *IEEE Global Telecommunications Conference*, Washington, USA, November 2007. 88

[86] V. Tarokh, N. Seshadri, and A.R. Calderbank. Space-time codes for high data rate wireless communication: Performance criterion and code construction. *IEEE Transactions on Information Theory,*, 44(2):744–765, 1998. 88

[87] M.S. Alouini and M.K. Simon. Multichannel reception of digital signals over correlated nakagami fading channels. In *Proceedings of the Annual Allerton Conference on Communication Control and Computing*, volume 36, pages 146–155. Citeseer, 1998. 91

[88] J.-M. Gorce, G. Villemaud, and P. Flipo. On simulating propagation for OFDM/MIMO systems with the MR-FDPF model. In *the Fourth European Conference on Antennas and Propagation (EuCAP)*, pages 1 –5, 2010. 100

[89] D. Umansky, J.M. Gorce, M. Luo, G. De La Roche, and G. Villemaud. Computationally efficient MR-FDPF and MR-FDTLM methods for multi-frequency simulations. *IEEE Transactions on Antennas and Propagation*, 61(3):1309 – 1320, 2012. 100

[90] C. Meyer. *Matrix analysis and applied linear algebra book and solutions manual*, volume 2. Society for Industrial and Applied Mathematics, 2000. 100

[91] A.P. Kannu, T. Sivanadyan, and S. Subramaniam. Performance of block adaptive modulation schemes for ofdm based wlan systems. In *2002 IEEE International Conference on Personal Wireless Communications*, New Delhi, India, December 2002. 107

[92] F. Edalat. *Real-time Sub-carrier Adaptive Modulation and Coding in Wide-band OFDM Wireless Systems*. PhD thesis, Massachusetts Institute of Technology, 2008. 107, 112

[93] G. Villemaud, G. De la Roche, and J.M. Gorce. Accuracy enhancement of a multi-resolution indoor propagation simulation tool by radiation pattern synthesis. In *IEEE Antennas and Propagation Society International Symposium*, pages 2153 –2156, 2006. 117